

University of Nevada, Reno

An Investigation of Tungsten-Based Z-Pinch Planar Wire Array and Benchmarking Experiments

*A dissertation submitted in partial fulfillment of the requirements for the degree of Doctor
of Philosophy in Physics*

Glenn Osborne

Dr. Victor L. Kantsyrev, Dissertation Advisor

December, 2012

Copyright by Glenn C. Osborne 2012

All Rights Reserved



University of Nevada, Reno
Statewide • Worldwide

THE GRADUATE SCHOOL

We recommend that the dissertation
prepared under our supervision by

GLENN OSBORNE

entitled

**An Investigation Of Tungsten-Based Z-Pinch Planar Wire Array And
Benchmarking Experiments**

be accepted in partial fulfillment of the
requirements for the degree of

DOCTOR OF PHILOSOPHY

Dr. Victor Kantsyrev, Advisor

Dr. Alla Safronova, Committee Member

Dr. Andrey Esaulov, Committee Member

Dr. Peter Winkler, Committee Member

Dr. Peter Beiersdorfer, Committee Member

Dr. Frederick Harris, Graduate School Representative

Marsha H. Read, Ph. D., Dean, Graduate School

Abstract

Wire array z-pinches provide an accessible means to research plasmas of high density and temperature and have valuable applications in the fields of inertial confinement fusion (ICF), astrophysics, and radiation studies. The purpose of this work is tungsten/aluminum z-pinch study and to aid in the development of diagnostics for tungsten x-ray radiation from a high-energy-density (HED) plasma, while exploring possible applications to hohlraum-based ICF research. The z-pinch experiments were primarily carried out on Zebra, the 1.0-1.7 MA pulse power generator located at the University of Nevada, Reno (UNR) Physics Department's Nevada Terawatt Facility (NTF), which creates plasmas with typical radiation emission quantum energies up to 2 MeV. This radiation is studied using an extensive suite of diagnostics, including optical imaging systems, x-ray detectors, spectrometers, and more, which yield both temporal and spatial information in the spectral region between 0.01 keV and 2 MeV.

This work also includes the results of research into a new and interesting phenomenon in z-pinch plasmas called bubbling. Specifically, planar wire arrays with relatively large inter-wire gaps where tungsten is placed in the center of a load configuration composed primarily of a single row of aluminum showed unusual characteristics. These loads are shown to generate an effect in which plasma from the ablation of outer aluminum wires is temporarily hindered from converging at the center of the array where the tungsten wire is located. A full investigation of this effect and possible applications to radiation pulse shaping, particularly with multi-planar arrays, are also discussed. A large number of other z-pinch x-ray radiation pulse shaping experiments with combined tungsten/aluminum planar wire arrays are also surveyed in addition to those included in the bubbling effect study. The generation of pre-pulses, or small radiation bursts prior to the primary x-ray radiation peak, is important

for driving hohlraum-based ICF loads. Additional experiments also explored methods for generating absorption spectra from z-pinch loads without the use of an external source by placing a single Al wire at the end of a W single planar wire array, which allowed the W M-shell emission to act as a semi-backlighter for K-shell Al absorption lines.

Data from other types of sources were also included in this study for the purpose of benchmarking and comparison, including experiments carried out on an electron beam ion trap at Lawrence Livermore National Laboratory (named EBIT-I). The EBIT data in particular was useful for the benchmarking of a model that was developed for M-shell W spectra, which utilizes the Theoretical Hebrew University Lawrence Livermore Atomic Code (HULLAC).

Dedicated to my father, Gregory J. Osborne,

for always inspiring me to achieve.

Acknowledgements

First, I am grateful to my advisors, Drs. Victor Kantsyrev and Alla Safronova, for without whom none of this work would have been possible. They have both guided and challenged me in both my research and in life, and have never hesitated to share their expertise and experience in my education as a student, a researcher, and a person. They have always gone above and beyond what was expected of them as mere graduate advisors to ensure that there would always be a path forward for me, and ensured that I stayed on it.

Second, I would like to thank each member of my doctoral committee for their guidance and wisdom over the years. In particular, Andrey Esaulov has always provided me with invaluable insights and conversation regarding all aspects of my research, Peter Beiersdorfer has never hesitated to be honest with me, question my conclusions, and challenge me to learn to and grow, and during my first years at the university, Frederick Harris gave his time freely in mentoring me both with my academics and with my life in general.

I would also like to extend my gratitude to my collaborators and fellow graduates students, Michael Weller, Ishor Shrestha, Kenneth Williamson, Veronica Schlyaptseva, Nicholas Quart, Steve Keim, and Austin Stafford, whom I've worked in the laboratory with for many years. The conversations and brainstorming sessions I've had with them were always interesting, and their camaraderie will be missed as I move on to the next stages of my life.

An acknowledgement is also extended to the members of the Nevada Terawatt Facility (NTF) and others within the Physics Department at the University of Nevada, Reno, where most of the experimental portions of this research took place, as well as the team at Cornell University where I also spent significant time participating in experiments. These collaborations helped to expand my knowledge and broadened my understanding of the research presented here. In particular, I would like to name Bruno LeGalloudec, Vidya Nalajala,

Alexey Astanovitskiy, and Steve Batie for their tireless efforts and the outstanding quality of their work at the Zebra facility at the NTF.

For their love and support outside the laboratory, I would also like to extend my gratitude to my friends and family, particularly my parents, Gregory and Jane Osborne. It was from them that I learned the values of knowledge, generosity, and perseverance, among many of the other positive qualities they have within themselves to share. My brother and sister, Steven Osborne and Katherine Lyle, respectively, have also set personal examples of achievement and excellence in their lives that have inspired me in mine. And lastly, a heartfelt thanks to my partner, Rebecca Evans, and my good and close friends, too numerous to name individually, for always being there when I needed them and providing me an endless source of encouragement.

The projects presented in this dissertation were funded by the DOE under Grant No. DE-FG02-08ER54951, the NNSA under Cooperative Agreements DE-FC52-06NA27586 and DE-FC52-06NA27588, and in part by DE-FC52-06NA27616.

Table of Contents

Abstract	i
Acknowledgements	iv
Table of Contents	vi
List of Tables	viii
List of Figures	x
I Introduction	1
1 Overview of Research	2
1.1 Z-Pinch-Generated Plasma	3
1.2 Laser-Produced Plasma	5
1.3 Electron Beam Ion Traps	5
1.4 Plasma Spectroscopy	6
2 Facilities and Diagnostics	7
2.1 Z-Pinch Machines	7
2.1.1 University of Nevada, Reno - “Zebra” Generator	7
2.1.2 Cornell University - “COBRA” Facility	14
2.2 University of Nevada - “Leopard” Laser	16
2.3 University of Nevada, Reno - “Sparky” Facility	17
2.4 Lawrence Livermore National Laboratory - “EBIT-I” Facility	18
II Tungsten/Aluminum Plasma Spectroscopy	20

3	EBIT Spectra	21
3.1	Identification of M-Shell W Lines	22
3.2	Modeling of M-Shell W	28
3.3	Charge State Balancing of W Ions	30
4	Z-Pinch Combined Tungsten/Aluminum Spectra	35
4.1	Aluminum Tracer Wires and Modeling of K-Shell Aluminum Plasma	35
4.2	Charge State Balancing of 3d-5l Transitions in Z-Pinch Spectra	37
4.3	Wire Array Plasma Absorption Spectroscopy with Semi-Backlighter Source	37
III	The Z-Pinch Ablation “Bubbling” Phenomenon	50
4.4	Spectroscopic Analysis of “Bubbling” Shots	55
4.5	Wire Array Dynamics Modeling	58
IV	Z-Pinch Radiation Pulse Shaping with Combined Tungsten and Aluminum Planar Wire Array Loads	62
5	Single Planar Bubbling Arrays	65
6	Double Planar Wire Arrays	67
7	Skewed Double Planar Wire Arrays	71
8	Triple Planar Wire Arrays	74
9	Load Type Comparisons	79
V	Conclusions	83
	References	87
VI	Appendix	96
A	List of Acronyms and Abbreviations	96
B	Constants	97
C	X-Ray Film Calibration	97
D	Zebra Scope Signal Processing	98
D.1	Power Calculations	100
E	B-Dot Calibrations on a 50 KV Pulser	101
F	List of Publications	104

List of Tables

List of Tables

3.1	Ionization potentials for W ($Z = 74$) most prominent in EBIT-I spectra. . . .	21
3.2	$3d \rightarrow 5l$ and $3d \rightarrow 6l$ line identifications for EBIT spectra at various electron beam energies with comparisons to existing tables by Kramida and Shirai (Kramida 2009). If no intensity is given, the line is blended with the one above it. Uncertainties for experimental EBIT data are discussed in the text in section III. Estimated uncertainties for all wavelengths listed from (Kramida 2009) were between ± 0.002 and ± 0.005 Å (see text). (Osborne 2010)	24
3.3	$3l \rightarrow 4l'$ line identifications for EBIT spectra at various electron beam energies with comparisons to existing tables by Kramida and Shirai (Kramida 2009). (*) denotes a line identified by J. Clementson (Clementson 2010) that was not included in (Kramida 2009). If no intensity is given, the line is blended with the one above it. Uncertainties for experimental EBIT data are discussed in the text in section III. Estimated uncertainties for all wavelengths listed from (Kramida 2009) were between ± 0.002 and ± 0.005 Å (see text). (Osborne 2010)	26
3.4	Table 3.3 contd. (Osborne 2010)	27
3.5	Theoretical fractional populations of prominent ion species in EBIT-I spectra of various electron beam energies shown in Fig. 3.4.	34
4.1	Transitions of K-shell Al and Mg spectral features prominent in z-pinch experiments, where λ is wavelength and A_r is rate of radiative decay.	36
4.2	Listing of prominent spectral emission features found in Fig. 4.7 along with estimations for the electron temperatures each line is commonly found at in Zebra-generated plasmas.	42
4.3	Listing of prominent spectral absorption features found in Fig. 4.7 along with estimations for the electron temperatures each line is commonly found at in Zebra-generated plasmas.	42
4.4	List of Zebra shots performed with the intension of creating K-shell Al absorption features. Shot configurations are given along with bolometer energy readings, the peak current through the load, the percentage of Al to W mass in the initial wire array, and whether or not the experiment produced absorption lines. Entries with '-' marks indicate data that was unobtainable for that particular experiment.	44

4.5	Comparison of parameters of W and W/Al shots. Single planar configurations are denoted using dots that represent single wires and multi planar arrays are shown using bars that indicate wire rows. Black indicates Al wires, gray indicates W, and light gray indicates Au. Implosion time measured from current start to PCD x-ray peak. The section of time between the start of the of x-ray output on the XRD signal and the implosion peak is given as Zone 1, and the section between the pre-pulse peak and the implosion peak is given as Zone 2. Pre-pulse percentage is calculated as the integral of the XRD signal from time $t = 0$ to the minimum point between the pre-pulse peak and the implosion peak divided by the integral of the entire signal. . . .	51
9.1	List of all shots in the pulse shaping survey where pre-pulse formations were observed. Graphical representations of each of the load configurations can be found in Figs. 8.1, 8.2, and 8.3. Pre-pulse percentages correspond to the ratios of integrated XRD signals that accounts for the pre-pulse formations with respect to the total XRD yield for the entire z-pinch lifecycle.	80
9.2	List of all shots in the pulse shaping survey where pre-pulse formations were not observed.	81

List of Figures

List of Figures

1.1	Picture of a single planar wire array for use on Zebra (see section 2.1.1) before it's placed in the load chamber.	4
1.2	Picture of a double planar wire array for use on Zebra (see section 2.1.1) before it's placed in the load chamber.	4
2.1	Simplified cartoon of the Zebra generator at the Nevada Terawatt Facility with major components labeled.	8
2.2	Simplified geometry of the LCM on Zebra (Chuvatin 2009).	8
2.3	Cartoon of time-integrated spatially resolved KAP spectrometer on Zebra. . .	10
2.4	Cartoon of a typical diagnostic setup on Zebra with viewports labeled, courtesy of M.E. Weller.	11
2.5	Diagram of convex crystal spectrometer, with λ_{\min} and λ_{\max} shown along with the angle of incidence, ϑ	13
2.6	Illustration of the COBRA generator at Cornell University (Greenly 2008). . .	15
2.7	Cartoon of a typical diagnostic setup on COBRA. Devices labeled #2, 5, 6, and 9 are the same that were used on Zebra, shown in Fig. 2.4.	16
2.8	Representation of the Leopard laser (left and top) with the Phoenix chamber (center) and Zebra (right) shown.	17
2.9	An artist rendition of EBIT-I (Levine 1998).	18
2.10	EBIT XRS microcalorimeter, with magnified image showing a single pixel (Porter 2000).	19
2.11	Cartoon of EBIT-I assembly with labels for all sections.	20
3.1	Overview of tungsten spectra for varying electron beam energies produced on EBIT-I.	22
3.2	Spectra of W on EBIT-I at varying electron beam energies with lines labeled in accordance with Table 3.2. Continuation of these spectra for wavelengths $> 5 \text{ \AA}$ is given in Fig. 3.3. (Osborne 2010)	23
3.3	Spectra of W on EBIT-I at varying electron beam energies with lines labeled in accordance with Table 3.1 and 3.2. (Osborne 2010)	25
3.4	$3d \rightarrow 5l$ model fitting and charge state balancing for EBIT-I spectra of various electron beam energies. Vertical axis is scaled linearly. (Osborne 2010)	31
3.5	Fractional populations of prominent ion species in EBIT-I spectra, derived using synthesized spectra calculated by HULLAC. Vertical axis is scaled linearly. (Osborne 2010)	31

3.6	Trends of independently normalized observed intensities of Ni-like W lines in EBIT-I spectra of various electron beam energies. Vertical axis is scaled linearly. (Osborne 2010)	32
3.7	Trends of independently normalized observed intensities of Cu-like W lines in EBIT-I spectra of various electron beam energies. Vertical axis is scaled linearly. (Osborne 2010)	32
3.8	Trends of independently normalized observed intensities of Zn-like W lines in EBIT-I spectra of various electron beam energies. Vertical axis is scaled linearly. (Osborne 2010)	33
3.9	Normalized intensities of unknown lines compared to averaged balancing trends of prominent ions in EBIT-I spectra at various electron beam energy. Vertical axis is scaled linearly. (Osborne 2010)	33
4.1	Identification and modeling of diagnostically important Al and Mg lines in a combined Al/W Zebra experiment, recorded with the TIXRS.	35
4.2	Spectrogram tracing from leopard shot #556, a low contrast (10^5) laser shot with pulse length 0.8 ns with a thin pure Al target. Lines are identified in accordance with Table 4.1 with modeling shown.	36
4.5	Configuration and orientations of spectroscopic diagnostics of Zebra shots #1297 and #2453. Light circles indicate tungsten wires where the dark circle indicates the aluminum tracer. (Osborne 2011)	38
4.3	Spectrum from z-pinch combined W/Al experiment. Prominent Al lines are indicated and model for charge state balancing of $3d-5l$ transitions is shown. (Osborne 2010)	39
4.4	Film scans of experimental results from shots (a) #1297 and (b) #2453, with time-integrated spectrometer data on the left. Positions where tracings were taken (shown in Fig. 4.7) are indicated by a corresponding line number, and regions where spectral features are most prominent are indicated above. Pinhole images are shown to the right of their appropriate spectrometer film, with (a) being a time-gated pinhole image and (b) a time-integrated pinhole image. The letters A and C indicate the orientation of the film images, denoting anode and cathode positions, respectively. (Osborne 2011)	39
4.6	Wire Ablation Dynamics Modeling for shot #1297. Experimental signals (XRD, PCD, and Current, as labeled) in (a) use arbitrary units, the estimated absolute value of the maximum distance where wire mass of each material is relative to the center of the array is given on the left axis, and the current scale is shown to the right. The horizontal axis scales the time evolution of the shot from the beginning of the current rise. A graphical representation showing the motion of plasma from each individual wire is given in (b).	40
4.7	Spectrogram tracings of shot #1297 with axial locations as indicated in Fig. 4.4. Prominent lines are labeled accordingly along with groupings of features shown in greater detail in Figs. 4.8 and 4.9. Vertical axis is in arbitrary units. (Osborne 2011)	41
4.8	Spectrogram tracings of lines 1 and 2 shown in Fig. 4.7 with emphasis given to the K-shell absorption features in line 1 (with line 2 shown for comparison). Clusters of lines are labeled according to their respective ion species. Vertical axis is in arbitrary units. (Osborne 2011)	43

4.9	Spectrogram tracing of $3d \rightarrow 5l$ M-shell W lines labeled in accordance with (Osborne 2010) from the first line indicated in Fig. 4.4. Vertical axis is in arbitrary units. (Osborne 2011)	44
4.10	Configuration (a) and film scans (b) of experimental results from shot #2609, with time-integrated spectrometer data on the left. A pinhole image (with cutoff wavelength $< 2.7 \text{ \AA}$) is shown to the right of the spectrometer film and is labeled (c). Wire Ablation Dynamics Modeling is shown in (d). Experimental signals (XRD, PCD, and Current, as labeled) in (d) use arbitrary units, the estimated absolute value of the maximum distance where wire mass of each material is relative to the center of the array is given on the left axis, and the current scale is shown to the right. The horizontal axis scales the time evolution of the shot from the beginning of the current rise.	46
4.11	A graphical representation showing the motion of plasma from each individual wire from shot #2609, calculated using Wire Ablation Dynamics Modeling.	47
4.12	Configuration (a) and film scans (b) of experimental results from shot #2610, with time-integrated spectrometer data on the left. A pinhole image (with cutoff wavelength $< 2.7 \text{ \AA}$) is shown to the right of the spectrometer film and is labeled (c). Wire Ablation Dynamics Modeling is shown in (d). Experimental signals (XRD, PCD, and Current, as labeled) in (d) use arbitrary units, the estimated absolute value of the maximum distance where wire mass of each material is relative to the center of the array is given on the left axis, and the current scale is shown to the right. The horizontal axis scales the time evolution of the shot from the beginning of the current rise.	48
4.13	A graphical representation showing the motion of plasma from each individual wire from shot #2610, calculated using Wire Ablation Dynamics Modeling.	49
4.14	Shadowgraphy (shown at the left four positions of each row of images, viewed parallel to the laser probe with the exception of the first row, which is at a 12.5° angle) and pinhole imaging (resolution of 220 \mu m and lower cutoff wavelength $\lambda_{1/10} < 3.1 \text{ \AA}$, viewed at a 45° angle, shown to the right of the shadowgraphy image) for shots (top row) 1765 – SPWA with wires spaced 2 mm apart, taken 24 ns before stagnation, (second row) 1955 – SPWA with wires spaced 2 mm apart, taken 39 ns before stagnation, (third row) 2162 – SPWA with wires spaced 2 mm apart, taken 28 ns before stagnation, and (fourth row) 2161 – SPWA with Al wires spaced 1.4 mm apart and 2.8 mm from the central W wire, taken 66 ns before stagnation.	52
4.15	Shadowgraphy images of bubbling shot showing time evolution of instabilities over an approximately 6 ns time frame, cropped for emphasis on the center of the array.	53
4.16	Signals for shots a) 1955 – Al/W/Al SPWA, 2 mm inter-wire gap, b) 1765 – W/Al/W SPWA, 2 mm inter-wire gap, c) 2456 – Al/W/Al SPWA, 1.4/2.8/1.4 mm inter-wire gap, and d) 2162 – Al/Au/Al SPWA, 2 mm inter-wire gap. Arrows indicate timing of shadowgraphy images shown in Fig. 4.14.	54
4.17	Time-integrated spectra of shot 1765 (W/Al/W non-bubbling load with 2 mm inter-wire gap), with prominent K-shell Al/Mg and M-shell W lines marked. W lines follow the identification labels used in section 3. Modeling of W $3d \rightarrow 5l$ transitions is shown, with model indicated in color and experiment in black.	56

4.18	Time-integrated spectra of shot 1955 (Al/W/Al bubbling load with 2 mm inter-wire gap), with prominent K-shell Al/Mg and M-shell W lines marked. W lines follow the identification labels used in section 3. Modeling of W $3d-5l$ transitions is shown, with model indicated in color and experiment in black.	57
4.19	Time-integrated spectra of shot 2456 (Al/W/Al bubbling load with 1.4/2.8/1.4 mm inter-wire gaps), with prominent K-shell Al/Mg and M-shell W lines marked. W lines follow the identification labels used in section 3. Modeling of W $3d-5l$ transitions is shown, with model indicated in color and experiment in black.	57
4.20	Quasi-continuous two dimensional (overhead view) distribution of the (a) plasma mass density $\rho(x,y)$ and (b) current density through the plasma $j_z(x,y)$ calculated by the WADM for Zebra shot #1955 (Al/W/Al bubbling load with 2 mm inter-wire gap) at time $t = 65$ ns, where the shadowgraphy image shown in Fig. 4.14 (second row) is taken. Dotted lines show approximate boundaries of the bubble region.	59
4.21	Volume densities of the radiation power losses Prad and Ohmic heating P_Ω in (a) tungsten and (b) aluminum plasmas at constant pressure 8×10^8 Pa, as a function of electron temperature T_e or the ratio of total wire mass M to the mass of the ablated plasma M_b	60
4.22	Sample shot with z-pinch lifecycle phases indicated. Signals shown are current (red), XRDs (blue), EUV (green), and PCDs (purple).	63
4.23	Radiation yields (PCD with 10 μm Be filter and EUV Si-Diode with 0.2 μm Al filter) of a cylindrical wire array experiment on COBRA, with current and a cartoon representation of the load configuration shown. All wires in the array were 10 μm Al (5005), an alloy consisting of 99.2% Al and 0.8% Mg.	64
6.3	Time-gated pinhole image of shot #1965, taken ~ 30 ns before the implosion peak, filtered to show radiation energies > 1 keV.	67
6.1	Sample shots from two of the DPWA configurations tested. Arrows on signals indicate the approximate times when the corresponding shadowgraphy images were taken. Initial positions of the arrays are indicated with white lines overlaid on shadowgraphy images, with slanted markers representing arrays that are viewed at an angle rather than parallel to the field of view.	68
6.2	Sample shots from two of the DPWA configurations tested. Arrows on signals indicate the approximate times when the corresponding shadowgraphy images were taken. Initial positions of the arrays are indicated with white lines overlaid on shadowgraphy images, with slanted markers representing arrays that are viewed at an angle rather than parallel to the field of view.	69
7.1	Sample shots from two of the skewed DPWA configurations tested. Arrows on signals indicate the approximate times when the corresponding shadowgraphy images were taken. Initial positions of the arrays are indicated with white lines overlaid on shadowgraphy images, with slanted markers representing arrays that are viewed at an angle rather than parallel to the field of view.	72
7.2	ICCD image of shot #1783, a skewed planar wire load, taken early in the implosion phase perpendicular to the planes of the array.	73
7.3	Shadowgraphy image of shot #1778, a skewed planar wire load, taken 54 ns before the implosion peak at an angle parallel to the planes of the wires.	73

8.1	Sample shots from two of the TPWA configurations tested. Arrows on signals indicate the approximate times when the corresponding shadowgraphy images were taken. Initial positions of the arrays are indicated with white lines overlaid on shadowgraphy images, with slanted markers representing arrays that are viewed at an angle rather than parallel to the field of view.	75
8.2	Sample shots from two of the TPWA configurations tested. Arrows on signals indicate the approximate times when the corresponding shadowgraphy images were taken. Initial positions of the arrays are indicated with white lines overlaid on shadowgraphy images, with slanted markers representing arrays that are viewed at an angle rather than parallel to the field of view.	76
8.3	Sample shots from two of the TPWA configurations tested. Arrows on signals indicate the approximate times when the corresponding shadowgraphy images were taken. Initial positions of the arrays are indicated with white lines overlaid on shadowgraphy images, with slanted markers representing arrays that are viewed at an angle rather than parallel to the field of view.	77
E.1	Sample of calibration shot on the 50 KV pulser at NTF. Lines that indicate they are combined refer to B-dot signals that have had the absolute values of their positive and negative portions averaged together.	102
E.2	Cartoon of the plate used on the 50 KV pulser at NTF for calibration of B-dots. Gray circles indicate rods that connect to a bottom plate (which is connected to ground), white circles indicate open holes where B-dots can be installed (the control B-dot position is marked with a C), and the central circle represents the location of the CVR where the current is passed to the plate from the pulser itself.	103

Part I

Introduction

University-scale generators offer a useful opportunity to investigate plasma properties in a cost-effective manner, while simultaneously educating students. These smaller experiments can also often be scaled or directly applied to research at much larger facilities, particularly national laboratories where repetitions of a single experiment can cost upwards of tens or even hundreds of thousands of dollars. The wealth of information that can be generated at the university scale is by no means small, however, and full suites of diagnostics provide the capability to rigorously investigate the generated plasmas. The devices used for these diagnostics are often developed at the universities where these laboratories exist and are then often also adopted or utilized in larger facilities. By providing these diagnostics and the plethora of information that's available through them, these smaller facilities play a crucial role in solving the vast puzzles involved in fusion research. Connecting the results of many different experiments and diagnostics can result in a far deeper understanding of a particular problem than by focusing on one set of data alone. For example, spectroscopic analysis provides a plethora of information about the interactions of free electrons in a plasma and can be used to infer temperatures, densities, and opacity properties of an experiment, but gives vague representations of the structure of the plasma column itself, which is better investigated by pinhole imaging or shadowgraphy. A humble attempt at piecing together the many pieces of a puzzle is presented here, specifically to investigate the properties of highly ionized tungsten (W).

1 Overview of Research

Tungsten has been an extensively studied topic of interest at Sandia National Laboratory (hereafter SNL) since 1998 when they showed the ability to produce X-ray power yields up to 200 TW and energies to 2 MJ (Spielman 1998, Deeney 1998), although the first x-ray spectra of M-shell W were produced in exploded-wire experiments more than 30 years ago (Burkhalter 1977). A large amount of research (Cuneo 2002, Cuneo 2005) has been devoted to exploring W plasmas, particularly in the high energy density (HED) regime characteristic of z-pinches, due in part to its high strength-to-weight ratio and opacity. Not only is it practical and easy to work with, it has proven to be an efficient radiator at the plasma temperatures and densities commonly found in large pulse pinch devices (Spielman 1998). Tungsten is also a topic of interest in magnetic fusion applications due large to its low erosion yield from plasma particle bombardment. This makes it an ideal candidate material for plasma-facing walls in tokamaks. The risk of contaminating the fusion plasma is still rather high, however, but there are both benefits and dangers associated with these impurities. One of the largest drawbacks comes from having high-Z ions that haven't been fully stripped radiating emission lines in low-Z plasma, which poses the threat of cooling the fusion medium enough to keep it from achieving burn conditions. There is a considerable benefit to having high-Z element impurities that emit line radiation, though, because it they can then be used as tracers to diagnose plasma parameters. But for W to be useful in this way as a probe, its spectroscopic properties must be well understood.

The driving motivation behind the research presented in this paper is to not only further develop diagnostics for W plasmas, but also to employ it and experiments with other materials to better understand the processes involved in z-pinch plasma lifecycles with an emphasis on ICF applications. These studies include investigations into z-pinch radiation pulse shaping, spectroscopic analysis and modeling of M-shell W transitions, using W plasma as a semi-backlighter for Al z-pinch absorption spectra, and behaviors that result from mixing materials of varying properties in z-pinch loads.

1.1 Z-Pinch-Generated Plasma

An interest in using z-pinches to drive ICF experiments has existed since even before the construction of the first z-pinch devices in the 1950s, and z-pinch was one of the first approaches considered for fusion power. Experimental and theoretical work through the 1950s and 1960s demonstrated that they had limited potential in direct fusion applications, however, due to their inherent susceptibility to magnetohydrodynamic instabilities (Anderson 1958). Advances in technology since then have given rise to much faster pulse power generation capable of producing intense sources of x-rays (Spielman 1998). During this period, a number of z-pinch machines have been built around the world at numerous institutions including (but not limited to) Sandia National Laboratories, University of Nevada, Reno, Imperial College, University of Michigan, and Cornell University. The basic operating principle of a z-pinch device is the Lorentz force, where a conductive wire is pulsed with current and experiences a force within its generated magnetic field. This force, when great enough, turns the wire material to plasma and highly ionizes it. In the case of many wires, such as in the wire arrays discussed here, another effect of the Lorentz force is that it will draw nearby wires with parallel current flow in the same direction towards each other, creating a plasma “pinch” at the center of the load where all of the ablated wire material converges and implodes. This is where z-pinch gets its name, where the “Z” refers to the direction of the current flow with respect to the anode and cathode. The intense current pulses that are required for these experiments are generally provided by capacitor banks, which deliver power to the electrodes within the load chamber.

The z-pinch experiments that are discussed in this paper are primarily W and Al and span a wide variety of applications and load configurations. Focus is also paid to the utilization of the planar wire array (PWA) z-pinch load configuration. This load type features an array of wires lined up in a row, rather than in the more conventional cylindrical shape. PWAs were proven to be efficient radiators on Zebra at the University of Nevada, Reno (UNR) (Kantsyrev 2006) and have since been considered for driving hohlraum-based ICF experiments at SNL (Jones 2010). The formations of x-ray radiation pre-pulses are impor-

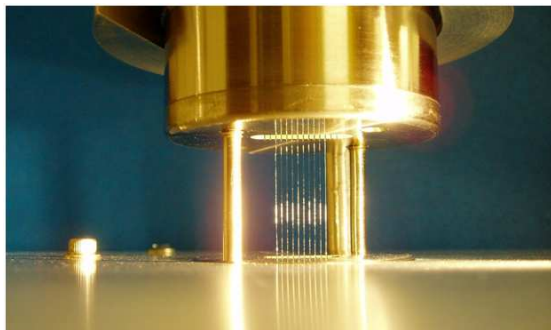


Figure 1.1: Picture of a single planar wire array for use on Zebra (see section 2.1.1) before it's placed in the load chamber.

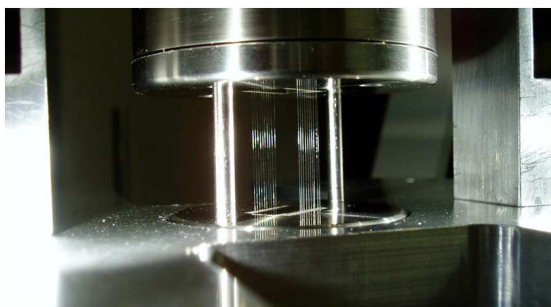


Figure 1.2: Picture of a double planar wire array for use on Zebra (see section 2.1.1) before it's placed in the load chamber.

tant for driving these hohlraum loads (Vesey 2007), so a campaign was launched at UNR to create a statistical understanding of the variations of pre-pulse shapes and their dependency on load configuration. Some of the results of those experiments are presented and discussed.

In the process of studying the pulse shapes of various PWA loads, unexpected instabilities were discovered by accident on the shadowgraphy images of a single PWA (SPWA) experiment that mixed tungsten and aluminum wires in a widely spaced configuration. This phenomenon was dubbed “bubbling” due to the bubble-like shapes first witnessed on laser probing images. A full investigation of this effect was launched in an attempt to not only understand its cause, but also to employ it in the shaping of plasma radiation yields in both single and multi PWA configurations. The results of this study are presented in part III.

1.2 Laser-Produced Plasma

While the field of laser-driven fusion ignition has often been in direct competition with z-pinch ICF initiatives, it can also be useful for providing a different perspective for studying the same ionization processes that are present in z-pinch plasmas. In these experiments, solid metal materials commonly used in our z-pinch loads were blasted with high-energy laser pulses, which ionized the material and turned it to plasma. Although these laser experiments generated much less intense total radiation than we typically witness in z-pinches, they do have the advantage of producing a narrower band of energies. This makes them ideal for studying high-Z elements such as W, which have complex atomic interactions, however the data that has been included in this research is primarily used for benchmarking an AI model.

Another advantage to laser-driven experiments is their extremely short pulse duration. A typical z-pinch experiment spans tens to hundreds of nanoseconds, but the laser experiments (Safronova 2012) that were conducted had plasma lifecycles on the order of femtoseconds, generated by relativistic 350 fs and 0.8 ns pulses. This allowed the observation of non-stationary ionization in hot multicharged plasma.

1.3 Electron Beam Ion Traps

An electron beam ion trap (EBIT) is a complex device used to trap and study radiating ions. Once ions have been injected into the vacuum chamber of the EBIT, a strong electron beam is activated and focused through the center of the device using a series of powerful electromagnets. Ions are pulled into the beam via the attractive force between the negatively charged electrons and the positively charged ion nuclei, where they are bombarded by electrons and further ionized into highly charged states. Electrodes are used to keep the ions confined axially, and the ions caught in the trapping region can often be held there for several minutes at a time.

One of the primary advantages to using EBITs to collect spectroscopic data lies within the ability for the electron beam to be configured and operate within a very narrow energy

band. This allows the user to select specific ranges of ionization energies to observe, which produce “clean” spectra ideal for studies in atomic physics. This is particularly useful in comparison to z-pinch plasmas from high-Z elements, such as tungsten, because spectra from the latter tend to include both resolved lines and unresolved continua from a wide range of energies, which can obscure specific features of interest. While there is a drastic difference in temperatures and densities between EBIT and z-pinch plasmas, resonance lines still appear at the same energies and can be directly compared for identification purposes. EBIT is also useful for benchmarking spectroscopic models that can later be applied to other regimes of plasma, particularly for complex high-Z materials, and one such procedure is presented and discussed in section 3.2.

1.4 Plasma Spectroscopy

Spectroscopy provides a nonintrusive means to extract a wealth of information from plasma radiation that may otherwise be unavailable or nebulous on other diagnostics. The interactions of free electrons with positively charged ions can provide information on numerous plasma parameters, including electron temperature and density, optical thickness, and charge state balance within the plasma. Much of this is made possible by the development of atomic codes where plasma properties are precisely specified and then compared against experimental data. While complex, these models have proven to be both accurate and informative.

Despite the surge in interest related to tungsten plasma in the late ‘90’s, the development of proper spectroscopic diagnostics for highly charged (M-shell) W radiation has been slow, however, due largely to the complexity involved in studying the electron interactions of such a high atomic number ($Z = 74$) element. A few approaches to diagnosing spectroscopic results from W are suggested here, with results shown from not only z-pinch experiments, but an electron beam ion trap as well.

2 Facilities and Diagnostics

The facilities used for these experiments are as diverse as the devices that were employed. The majority of the z-pinch experiments were done at UNR on Zebra with supplemental data from collaboration work with Cornell University using Cobra. While the similar operational parameters of these two machines offered valuable comparisons, the differences in facilities provided unique challenges and ample opportunities for student learning. For example, Zebra's daily functionality and its core diagnostics are maintained by a team of technicians that work in conjunction with scientists conducting experiments. This generally allows more data to be obtained per shot from Zebra, but experiments are restricted to a somewhat rigid schedule. The Cobra facility offers a much more relaxed atmosphere in which the device is operated almost entirely by students, which allows a great deal of freedom not always available on Zebra, but does so at the expense of shot-to-shot efficiency.

Many of the diagnostics were fielded at multiple locations and, in some cases, slightly modified to better observe the generated plasmas. For example, Sparky, the small pulse laser device found in the Physics Department at UNR was not only used to collect extreme ultraviolet (EUV) spectra, but also test a number of diagnostics for use on both Zebra and Leopard. Many of the diagnostics that were used on Zebra were also used on Leopard, though some required slight modification.

2.1 Z-Pinch Machines

The two z-pinch machines used for the experiments discussed here are "Zebra" at the Nevada Terawatt Facility and "COBRA" at Cornell University. These two machines have similar operational parameters and, as such, are able to share many of the same diagnostics.

2.1.1 University of Nevada, Reno - "Zebra" Generator

The Nevada Terawatt Facility is a division of the Physics Department at the University of Nevada, Reno. Located approximately 20 miles north of the main campus, the facility houses the largest university-scale pulse power device in the United States, named Zebra

(Bauer 1997).

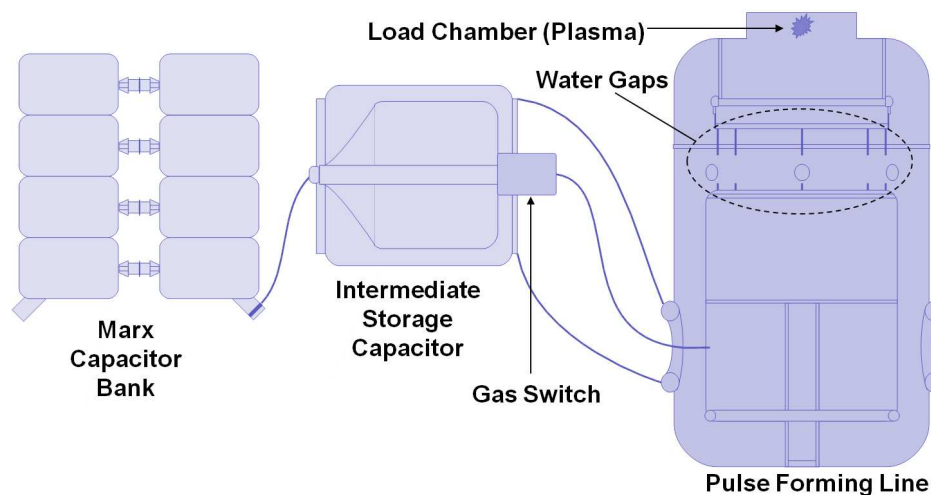


Figure 2.1: Simplified cartoon of the Zebra generator at the Nevada Terawatt Facility with major components labeled.

The Zebra generator is capable of delivering up to 1.5 TW of power in the span of 100 ns. This short, high-voltage pulse is achieved by charging a bank of 32 1.3 μF capacitors in parallel up to 85 kV and then discharging them in series. The pulse that results from the Marx capacitor bank discharge is microsecond-scale, but is compressed twice before reaching the targeting chamber, first by an intermediate 28 nF, 3.5 MV storage capacitor that uses water as a dielectric. A gas switch is configured to self-trigger once the intermediate capacitor

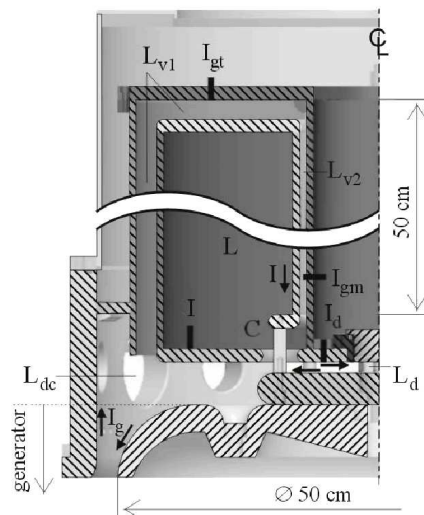


Figure 2.2: Simplified geometry of the LCM on Zebra (Chuvatin 2009).

reaches approximately 80% charge, and then the pulse is sent down a 1.9Ω coaxial vertical transmission line and up into the target chamber, the walls of which act as the return current

path. Zebra has a generator inductance of 26 nH and a chamber inductance of 30 nH. The Marx capacitor bank has a maximum energy storage potential of 150 kJ.

Normally, Zebra's maximum delivered current is about 1 MA, as governed by the circuit equation (neglecting resistive losses)

$$V_{oc}(t) + \rho I_0(t) + (L_0 + L_{dc} + L_d) \frac{dI_0(t)}{dt} = 0, \quad (2.1)$$

where $V_{oc}(t)$ is the generator open-circuit voltage, $\rho = 1.9 \Omega$ is the machine impedance, $L_0 \approx 26$ nH the generator inductance, L_{dc} is the chamber inductance, L_d the load inductance, and $I_0(t)$ is the generator current. However, this has recently been increased (Chuvatin 2009) to 1.7 MA with the development of a chamber modification called the load current multiplier (LCM) (Chuvatin 2006). The efficiency of energy transfer to the load is generally limited by the inductance mismatch between the load itself and the pulse generator, and the LCM effectively acts as an impedance converter to increase delivered current. The device consists of two concentric cylinders that act as electrodes and replace the anode portion of the load chamber. We can expand Eq. 2.1 to include this new hardware (shown in Fig. 2.2) by distinguishing $I_g(t)$ as the generator current (different now from $I_0(t)$ above), $L_v = L_{v1} + L_{v2} \approx 24$ nH as the new LCM magnetically insulated transmission line (MITL) inductances, and $L \approx 90$ nH as the large LCM cavity inductance to be

$$V_{oc} + \rho I_g + \left(L_0 + L_{dc} + L_v + \frac{4LL_d}{L + L_d} \right) \frac{dI_g}{dt} = 0. \quad (2.2)$$

When the current pulse reaches the inner surface of the outer cylinder, an equal and opposite current is induced the inner cylinder. The two currents are combined at the convolute, effectively multiplying the amplitude of the pulse delivered to the load by

$$\kappa \equiv \frac{I_d}{I_g} = \frac{2L}{L + L_d}, \quad (2.3)$$

where I_d denotes the current delivered to the load. Experiments in which a static (constant inductance) rod was used as a load in Zebra and the current was returned through 8 posts at

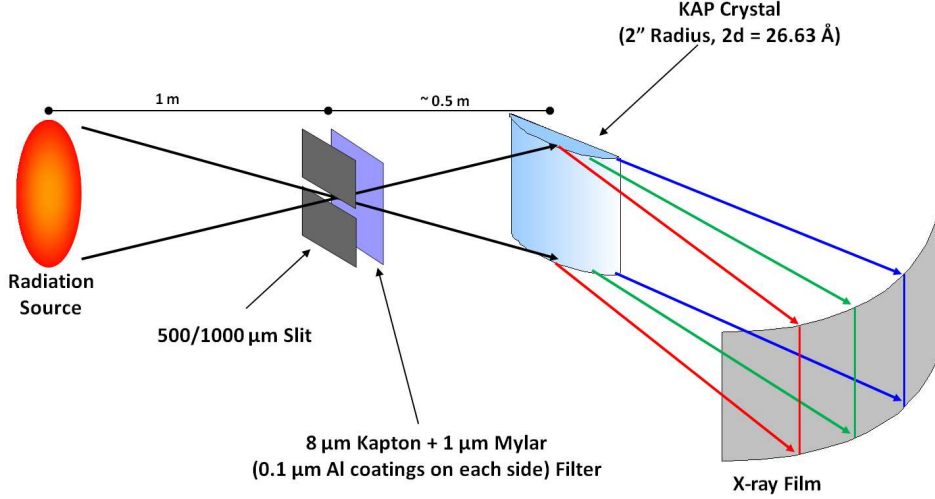


Figure 2.3: Cartoon of time-integrated spatially resolved KAP spectrometer on Zebra.

the LCM convolute showed consistently that $L_d \approx 7$ nH, resulting in a current multiplication factor of $\kappa \approx 1.86$.

Diagnostics on Zebra change and evolve between experimental campaigns, but a cartoon of the most recent configuration can be seen in Fig. 2.4. The majority of the diagnostics are connected radially to one of a set of 16 viewports located 30 cm from the center of the load chamber. These devices include two bare Ni bolometers, photoconducting detectors (PCD) (Sherlock 2004), x-ray diodes (XRD), silicon diodes with 25 or 50 μm pinholes that measure x-ray and extreme ultraviolet (EUV) radiation, an intensified charge-coupled device (ICCD) camera, a visible light streak camera, a time-integrated pinhole (TIPH) imager, a time-integrated potassium hydrogen phthalate (KAP) crystal (2 inch radius, $2d = 26.63$ Å; see Eq. 2.9 and following discussion for more details) spectrometer (TIXRS) fielded with a 0.5 mm slit to produce data of spatial resolution of 1.5 mm and spectral resolution of 500 (cartoon shown in Fig. 2.3), and an optical probing system that uses a 150 ps pulse laser with wavelength 532 nm that is split into four channels spaced 3, 6, and 3 ns apart. The critical density, or maximum electron density that allows propagation of a laser probe with frequency ω_L through a non-relativistic plasma is

$$n_{cd} = \frac{m_e \omega_L^2}{4\pi e^2}, \quad (2.4)$$

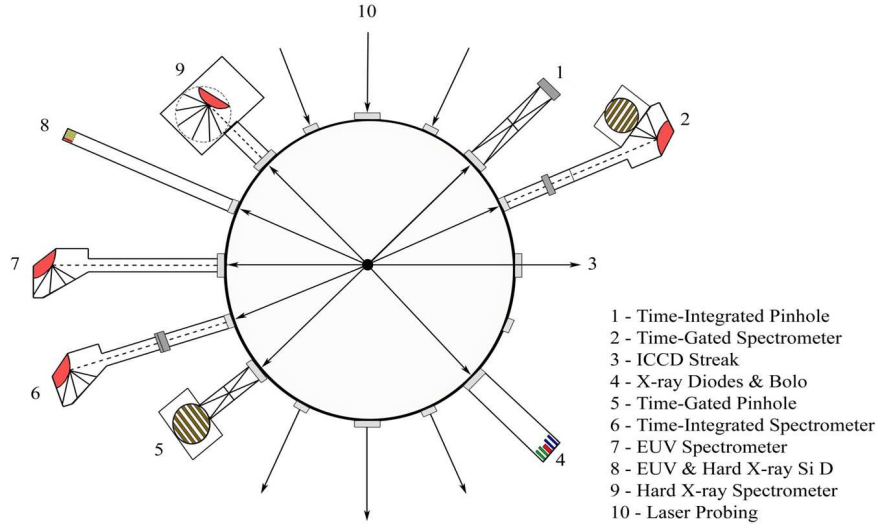


Figure 2.4: Cartoon of a typical diagnostic setup on Zebra with viewports labeled, courtesy of M.E. Weller.

which comes to $n_{cd} \approx 4 \cdot 10^{21} \text{ cm}^{-3}$ for a 532 nm laser pulse.

The TIPH uses layered Bio-max MS Kodak x-ray film to provide images with typical cutoff wavelengths of $\lambda_{1/10} < 10.3, 4.4, 3.7, 3.1, 2.9,$ and 2.7 \AA with spatial resolution of 220 \mu m (calculated from the distance between the source and the pinhole a , the pinhole and the film b , and the pinhole diameter d using the equation

$$\Delta l = d \left(1 + \frac{a}{b} \right). \quad (2.5)$$

The magnification can be calculated as

$$\Gamma = - \left| \frac{b}{a} \right| \quad (2.6)$$

and the Rayleigh Criterion as

$$l_R = 1.22 \lambda \frac{a}{d}, \quad (2.7)$$

which gives a diffraction-limit of the minimum wavelength that can be effectively imaged.

The XRDs used were designed with a Ni mesh and strong permanent magnets to deflect charged particles and prevent them from puncturing the filter or contaminating the surface of the detector, which is biased at 1000 V. Their response time, which is limited by the work function of the Ni mesh, is approximately 500 ps in an energy range between 5 eV and 2 keV. Because these detectors are representative of such a relatively wide energy band, they're often used in conjunction with bolometer data to calculate the power output of the z-pinch experiments, a process which is discussed in further detail in appendix D.1. The spectral response of the PCDs is higher energy, between 50 eV and 5 keV, and are able to operate at a much lower (typically -100 V) bias with a faster time resolution of approximately 200 ps. As most signals from these devices were normalized to emphasize the time evolution of their respective readings, absolute intensity corrections were not necessary, however it should be noted that in cases where they were, a correction had to be applied to the PCD voltages due to saturation effects compressing the signal (Spielman 1997). The correction formula used was:

$$V_R = \frac{V_S}{1 - \frac{V_S}{V_B}}, \quad (2.8)$$

where V_R is the real voltage, V_S is the voltage read from the scope, and V_B is the bias voltage applied to the PCD (typically -100 V).

Also included in Zebra's diagnostic suite are a time-gated x-ray spectrometer (TGXRS), pinhole imager (TGPH), and EUV spectrometer (TGEUV). Each of these devices is essentially the same as its time-integrated counterpart, except that they use micro-channel plate (MCP) photomultipliers with six gold strips and a pulsed bias to obtain time-resolved images. Each gold strip acts as a photocathode, where incident photons are converted to electrons via the photoelectric effect and are accelerated through plate capillaries. This causes a cascading emission of secondary electrons that impact a phosphor screen, which in turn is exposed to visible wavelength film. The TGPH imager has a spatial resolution of 230 μm and uses two 70 μm pinholes per frame, which are typically filtered to provide lower cutoff wavelengths of $\lambda_{1/10} < 10 \text{ \AA}$ and $\lambda_{1/10} < 3.5 \text{ \AA}$ and exposed for 3 ns with 6-10

ns interframe delay. As with its time-integrated counterpart, these wavelength ranges are governed by Bragg's Law,

$$2d \sin \theta = m\lambda, \quad (2.9)$$

where d is the atomic spacing in the crystal lattice, θ is the angle of incidence, m is the order of diffraction, and λ is the diffracted wavelength. A diagram of this layout is shown in Fig. 2.5. The theoretical maximum wavelength λ_{\max} , then, is generally $2d$, for a first-order spectrum, but the actual standardized registration range parameter is given as

$$\Lambda = \frac{2(\lambda_{\max} - \lambda_{\min})}{\lambda_{\max} + \lambda_{\min}}. \quad (2.10)$$

The TGXRS is typically fielded with a KAP crystal that has the same parameters as the TIXRS ($2d = 26.63 \text{ \AA}$) and observes similar wavelengths. The spectral resolution

$$R = \frac{\lambda}{\Delta\lambda} \quad (2.11)$$

is a ratio of wavelength to the minimum difference between simultaneously resolved features and is generally a result of source size and imperfections in the diffraction crystal.

The TGEUV spectrometer (Williamson 2011) utilizes a grazing incidence from a spherical grating. Gratings that are typically used are W/Re or Au with 1200, 600, and 300 mm⁻¹ groove densities, three of which can be used at a time for each experiment, providing wavelength ranges anywhere between 3 and 90 nm, calculated using the grating equation

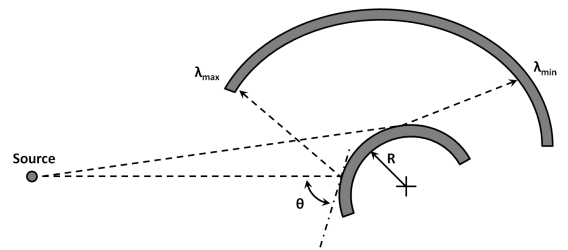


Figure 2.5: Diagram of convex crystal spectrometer, with λ_{\min} and λ_{\max} shown along with the angle of incidence, ϑ .

$$m\lambda = d(\sin \theta_i + \sin \theta_m), \quad (2.12)$$

where m is the order of diffraction, λ is the diffracted wavelength, d is the grating groove spacing, ϑ_i is the angle of incidence, and ϑ_m is the angle of diffraction. ϑ_m is determined using the grating-photofilm distance r_b :

$$r_b = R \cos(\theta_m), \quad (2.13)$$

where R is the grating radius (1000 mm for all gratings used on this spectrometer). Filters used were 395 or 150 nm zirconium.

In addition to plasma diagnostics, a number of machine diagnostics are also available for measuring current and voltage at various locations on Zebra. For the current measurements, this is primarily done using differential B-dot detectors (Stygar 1997), which induce voltage through conductive loops via Lenz’s Law. By experimentally calibrating each of these devices, a coefficient for each loop can be derived that allows direct conversion to the change in current, dI/dt . Generally, each B-dot consists of two loops of opposing windings, resulting in both a “positive” and a “negative” signal that are averaged together after corrections are made for the *DC* off-set, primarily to facilitate a common-mode noise cancellation. Once this noise factor has been subtracted out, the two signals are combined and integrated to give a relatively accurate measurement of current over time. For more information regarding the details of specific B-dots and methods of calibration that were conducted for these experiments, see appendix E.

2.1.2 Cornell University - “COBRA” Facility

COBRA is a pulse power generator similar to Zebra that is located at Cornell University. The two generators have numerous differences that make them ideal for experimental comparisons, however. COBRA also utilizes Marx capacitor banks, which have a maximum charge of 70 kV and drive a current of 1 MA. COBRA’s capacitors are split into two banks, however, and fed into the load chamber via four independent laser-triggered transmission lines. This allows for the customization of current pulse shapes (Greenly 2008) with rise times ranging between 85 and 250 ns. COBRA has a total line impedance of 0.35 Ω , a

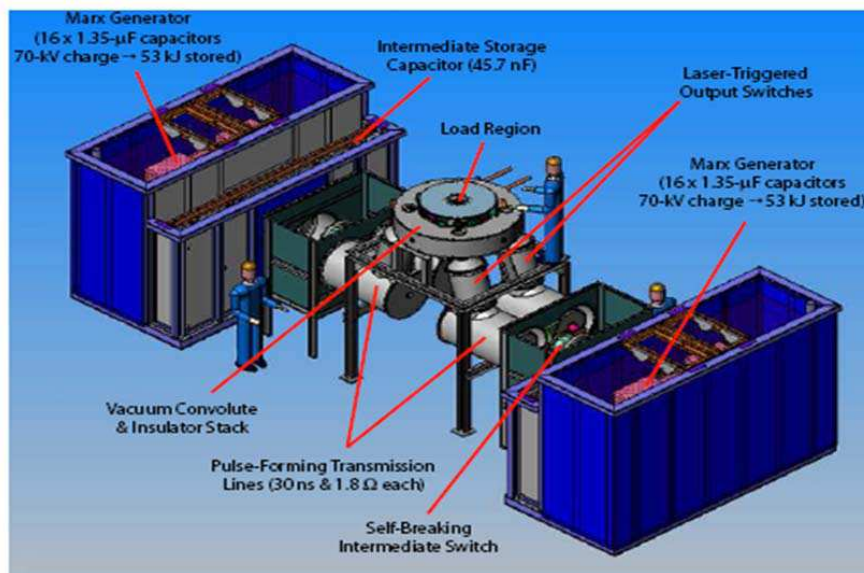


Figure 2.6: Illustration of the COBRA generator at Cornell University (Greenly 2008).

generator inductance of 10 nH, a load inductance of 6-10 nH, and a maximum delivered energy of 100 kJ. The total machine inductance is dependent on the load inductance, which means that unlike Zebra, the efficiency of energy transfer is sensitive to load configuration. COBRA has a load chamber 60 cm in diameter, but it is not used to return the current. Instead, a series of four posts placed 5 cm from the center of the chamber act as return current rods.

On-site diagnostics on COBRA (shown in Fig. 2.7) included a time-gated EUV camera, a time-integrated Mica crystal spectrometer, an array of PCD and Bolo detectors, a time-integrated x-ray pinhole camera, and a time-integrated EUV spectrometer. A few devices were also taken from the Zebra suite to aid in data collection, including the time-gated x-ray spectrometer, the time-integrated LiF spectrometer, and an array of silicon diodes for measurements in both the EUV and hard x-ray regions. Because of COBRA's utilization of return current posts (rather than using the chamber itself to return the current), it was possible to put a number of diagnostics directly into the chamber safely, and those included all three of the time-integrated spectrometers and the time-integrated pinhole camera.

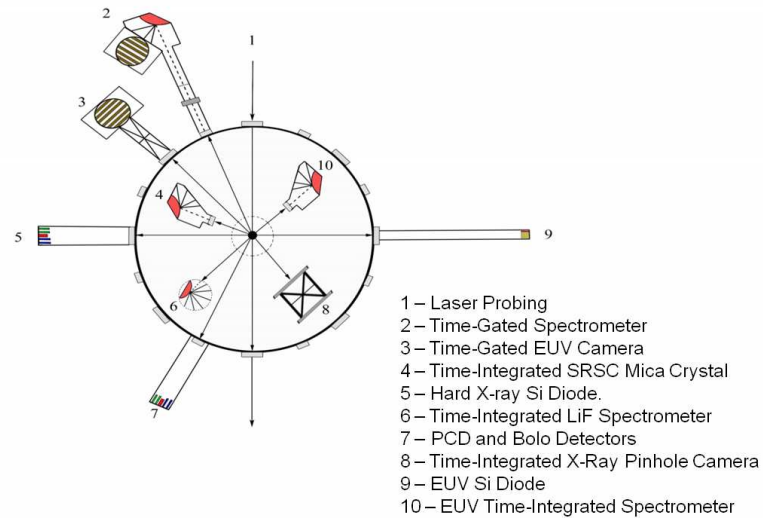


Figure 2.7: Cartoon of a typical diagnostic setup on COBRA. Devices labeled #2, 5, 6, and 9 are the same that were used on Zebra, shown in Fig. 2.4.

2.2 University of Nevada - “Leopard” Laser

Leopard (Wiewior 2012) is a versatile laser system located at the University of Nevada, Reno that is capable of being coupled with the Zebra pulse power generator (see section 2.1.1). It has an energy range of 10-20 J, delivered in pulses as short as 300 fs at a wavelength of 1057 nm. Its maximum pulse intensity is 10^{19} W/cm². It operates using a technique known as Chirped Pulse Amplification (CPA), in which a lower intensity pulse is stretched, amplified, and then recompressed and, finally, focused on its target. The original pulse is generated by a commercial diode-pumped Nd:YVO₃ laser and then amplified using a frequency-doubled Nd:YLF laser that operates at a 500 Hz repetition rate. A chirped pulse stretcher unit, coupled with this system, provides pulses of nearly 10 nm and energy 1 mJ, which are then injected into the flash-lamp amplifier section, and then eventually recompressed using a Falcon optical vacuum compressor. For this research, the laser was focused directly onto solid targets, namely Al.

Once the laser pulse has been generated, it is sent along a beam path into the same room that houses the Zebra generator. There, it can either be injected directly into the Zebra load

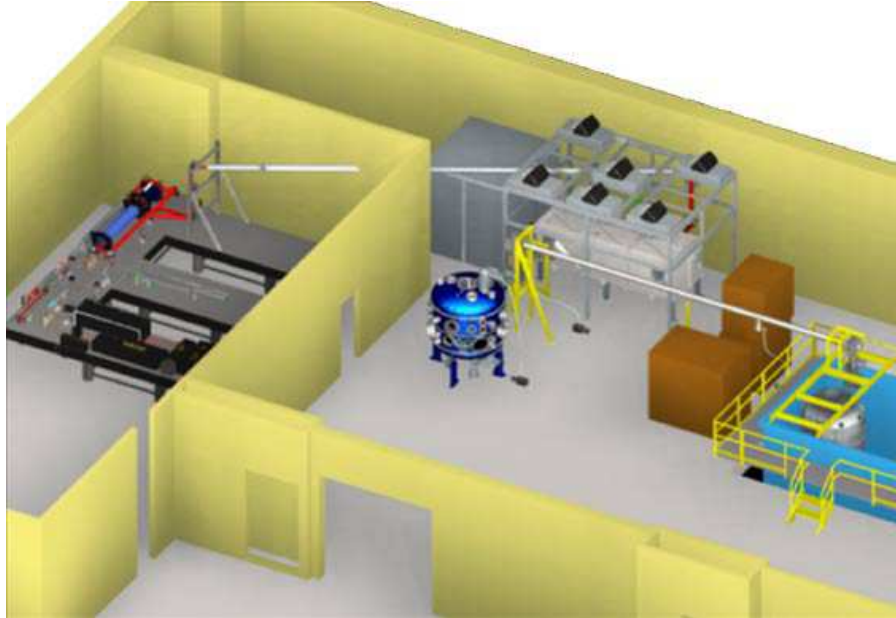


Figure 2.8: Representation of the Leopard laser (left and top) with the Phoenix chamber (center) and Zebra (right) shown.

chamber via one of the 16 radial diagnostic viewports, or it can be sent into the Phoenix targeting chamber for stand-alone experiments. All studies conducted for this research were done in the Phoenix chamber utilizing a number of the same diagnostics that are used on Zebra, including the TIXRS and Si-diodes, both x-ray and EUV range. Other diagnostics also included two time-integrated pinhole imagers and a focusing spectrometer with spatial resolution (FSSR) that uses a spherically bent mica crystal ($2d = 19.91 \text{ \AA}$) that covers a narrow spectral region (14.5 to 17.5 \AA first order, 7.25 to 8.75 \AA second-order reflections) but has a very high resolution of ~ 3000 . This device was further configured to record 8th order reflections between 1.85 and 1.94 \AA using layered x-ray film.

2.3 University of Nevada, Reno - “Sparky” Facility

Sparky (Kantsyrev 2005) is a small pulse power z-pinch and laser device located at the University of Nevada, Reno, within the Department of Physics Plasma Physics and Diagnostics Laboratory (PPDL). The system constructed around a continuum Nd:YAG laser of wavelength 1.06 μm , with pulse repetition rate 10 Hz and duration 3.4 ns and energy 0.45 J. It is

primarily focused directly onto solid targets that are located inside a vacuum chamber that also connects to two radial viewports. Inside the chamber, several diodes and spectrometers can also be mounted. Sparky is capable of producing plasmas with electron temperatures in excess of 300 eV with laser radiation flux density up to $2 \cdot 10^{13}$ W/cm² on the target.

Since Sparky's maximum energy range is on the order of millijoules, hundreds of repetitions are generally required to produce clear spectral data. It is generally used to test and calibrate time-integrated diagnostics that are later used on other larger devices, such as Zebra, however it also provides useful spectra in the EUV range, and has provided data on numerous materials, including Al, W, Cu, Teflon, Alumel, and others.

2.4 Lawrence Livermore National Laboratory - "EBIT-I" Facility

All EBIT data used for this research was generated on the EBIT-I (Levine, 1988) device at Lawrence Livermore National Laboratory. A cartoon of the important operational components of EBIT-I are shown in Fig. 2.11. The electron beam is generated in the electron gun assembly, which creates emission via thermal heating across its concave surface. This surface acts as a cathode, with the electrons being stripped off by an anode located above. A "bucking coil" surrounds the cathode and aids in removing

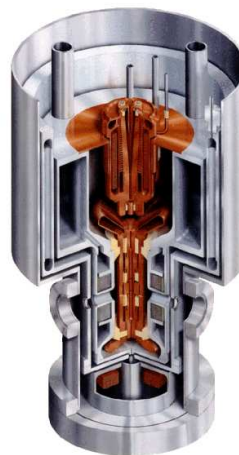


Figure 2.9: An artist rendition of EBIT-I (Levine 1998).

magnetic field components that would accelerate electrons outside the path of the beam. This resulting electron beam then passes through a series of three circular electrodes, called drift tubes, that define the trapping region where ions are injected. These drift tubes create a potential well of variable depth using relatively low bias voltages (typically ~ 400 V) on each individual electrode, while the entire assembly is biased to much higher voltages (~ 30 kV). These biases are primary factors for determining the kinetic energy of the impacting

electrons when they collide with trapped ions.

A series of Helmholtz coils are also used to provide radial compression of the electron beam in the trapping region, which is an approximately 2 cm wide area at the center of the middle drift tube. These magnets provide a 3 T field with a coil current of 160 A, which results in an electron density of $\sim 10^{11} \text{ cm}^{-3}$ for what becomes an approximately 60 μm wide beam. Six radial view ports are located around the center drift tube, where the electron-ion interactions occur, to allow diagnostic connections. Once the electrons have passed through the trapping region beyond the top-most drift tube, they are terminated by a liquid nitrogen-cooled collection magnet.

The ions themselves are injected by a Metal Vapor Vacuum Arc (MeVVA). For these experiments, the ions were injected through the collector. The MeVVA does this by using high-voltage discharges to sputter ions off of a metal surface. Since the timing of these discharge pulses can be defined by the user, ions can be injected at specific intervals into the EBIT, allowing for control of the charge state balance of ions already within the trap before introducing a fresh bundle.

Spectra were recorded using an engineering model x-ray spectrometer (XRS) microcalorimeter (Porter 2000), shown in Fig. 2.10. Photons were filtered and detected by 14 of the 32 available independent pixels, which act as a non-dispersive XRS with resolution of 10 eV. All W spectra were generated with steady-state electron beam ener-

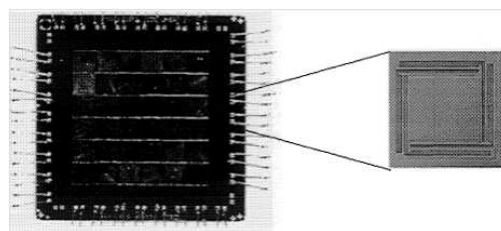


Figure 2.10: EBIT XRS microcalorimeter, with magnified image showing a single pixel (Porter 2000).

gies between 2.3 and 4.1 keV, although the electron gun is capable of a much broader energy band. Each experiment was carried out for a varying length of time, meaning that total electron counts for each pixel are not meaningful, however relative line intensities can be determined and provide diagnostically important information.

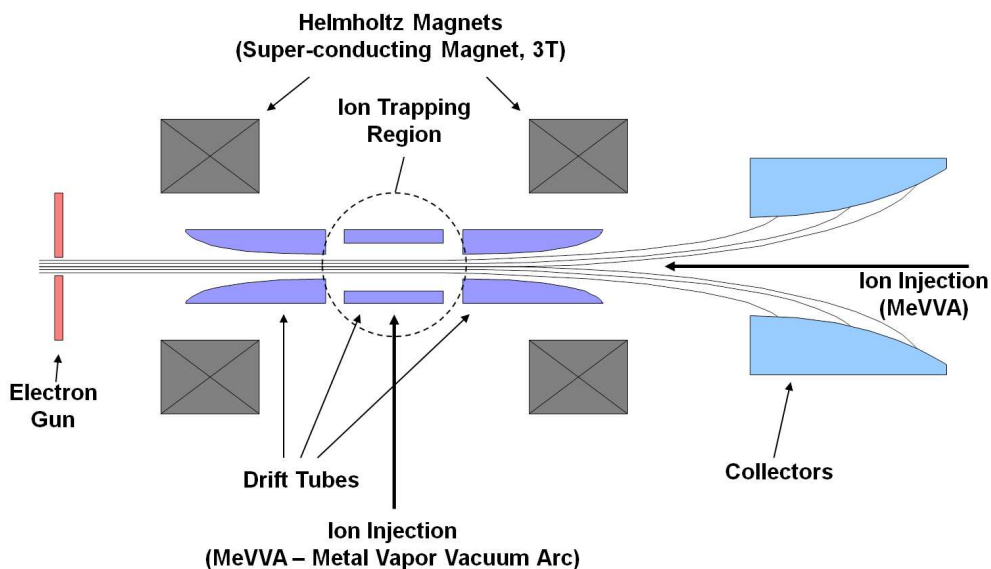


Figure 2.11: Cartoon of EBIT-I assembly with labels for all sections.

Part II

Tungsten/Aluminum Plasma Spectroscopy

This research focuses on both experimentally and theoretically generated M-shell tungsten spectra, with an emphasis on charge-state balancing and utilizing EBIT-generated spectra for analysis of z-pinch data. Focus is given to $3d \rightarrow 5l$ transitions due to their relatively thin optical densities in z-pinch plasma, which makes them ideal for modeling and extraction of plasma parameters. A model that was developed and benchmarked against experimental EBIT spectra is presented here, along with the associated atomic data and comparisons with z-pinch results, primarily from planar wire arrays. A method for using optically thick W plasma as a semi-backlighter for Al absorption lines in z-pinch loads is also presented in section 4.3.

3 EBIT Spectra

All EBIT spectra for this research was generated on the EBIT-I device at LLNL (see section 2.4) at specific electron beam energies of $E_B = 2.3, 2.5, 2.7, 2.9, 3.3, 3.9, 4.1, 4.2, 4.3, 4.7,$ and 5.35 keV. This energy band primarily produces $3d \rightarrow 5l$ and $3d \rightarrow 4l$ W spectral features from Fe, Co, Ni, Zn, Cu, Ga, Ge, As, and Se-like ions. A complete compilation of these spectra is shown in Fig. 3.1 to emphasize the evolution of the W spectra due to increasing electron beam energy, but the focus of this research is primarily on Co, Ni, Zn, Cu, Ga, and Ge-like transitions, which are most prominent for $E_B = 2.5, 2.7, 2.9, 3.3, 3.9,$ and 4.1 keV (see Table 3.1 for ionization potentials), and are discussed in further detail in the following sections.

Since each of the experiments performed on the EBIT were conducted for varying lengths of time, absolute photon counts are not meaningful and all spectra have been normalized to emphasize relative line intensity. Small drifts in wavelength that appear between experiments have been corrected by calibrating to prominent spectral features, which are generally Ni-like lines. Once this correction has been applied, the results from the 16 pixels on the microcalorimeter are averaged together to get the final spectrum. Given the limitations of the microcalorimeter's resolution, a small calculated error in the theoretical data that was used for calibration and a slight margin of error in the calibration curve itself resulted in a discrepancy in experimental wavelengths that range from ± 0.009 at 4.31 Å to 0.017 at 7.93 Å.

Z	Ion	Energy
32	Ge	2.16 keV
31	Ga	2.22 keV
30	Zn	2.37 keV
29	Cu	2.42 keV
28	Ni	4.06 keV
27	Co	4.19 keV

Table 3.1: Ionization potentials for W ($Z = 74$) most prominent in EBIT-I spectra.

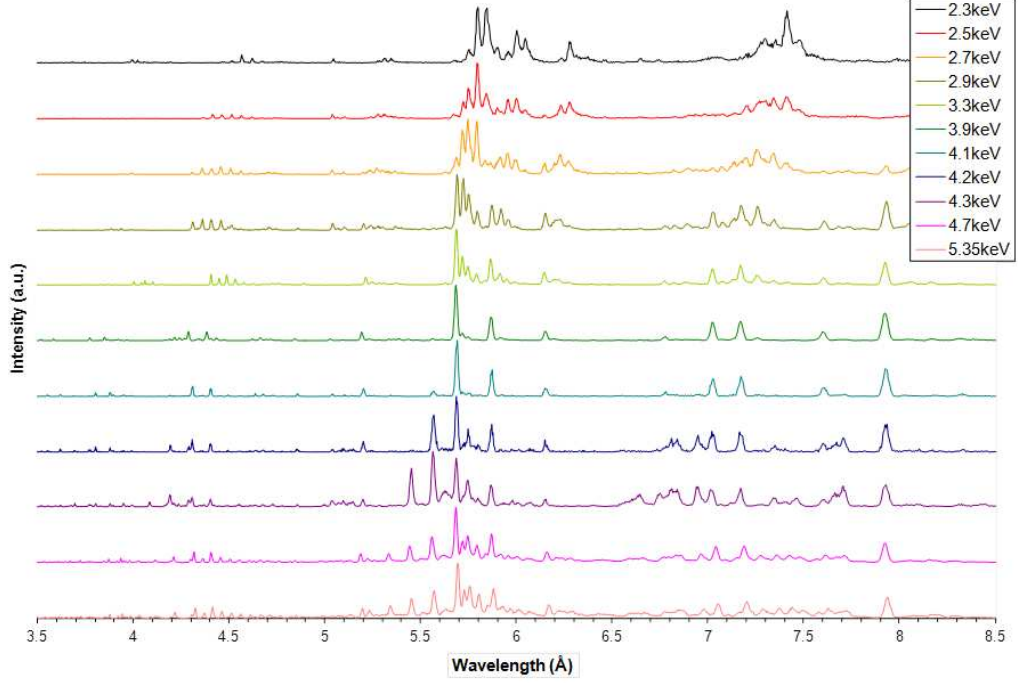


Figure 3.1: Overview of tungsten spectra for varying electron beam energies produced on EBIT-I.

3.1 Identification of M-Shell W Lines

All lines between 5 and 6 Å were identified by Neill et al. (Neill 2004) using the EBIT-II electron beam ion trap at Livermore at $E_B = 2.4$ and 2.8 keV, and were reaffirmed by the fully relativistic many-body perturbation theory (RMBPT) code. These authors identified and assigned the majority of these lines to the $4d \rightarrow 3p$ and $4f \rightarrow 3d$ transition groups. The only exception is the blended line we observed at 5.959 ± 0.013 Å, which was identified by Zigler et al. (Zigler 1980) in laser-produced plasma at 5.956 Å and given the Ni-like assignment $3d^{10} 1S_0 - 3d^9 4f (5/2, 5/2)^0_1$. Fournier (Fournier 1998) calculated a Cu-like line at 5.960 Å, however Kramida and Shirai (Kramida 2009) did not observe any intense line at 5.956 Å in calculations with Cowan's code and chose to omit it. Clementson et al. (Clementson 2010) observed the same line at 5.9545 Å and gave it the Zn-like assignment $3d^{10} 4s^2 1S_0 - 3d^9 ({}^2D_{5/2}) 4s^2 4f_{7/2} (5/2, 7/2)_1$. Comparison of ionization balance in experimental EBIT spectra for varying electron beam energies suggests strong correspondence with Zn-like W, so the identification made by Clementson is preferred.

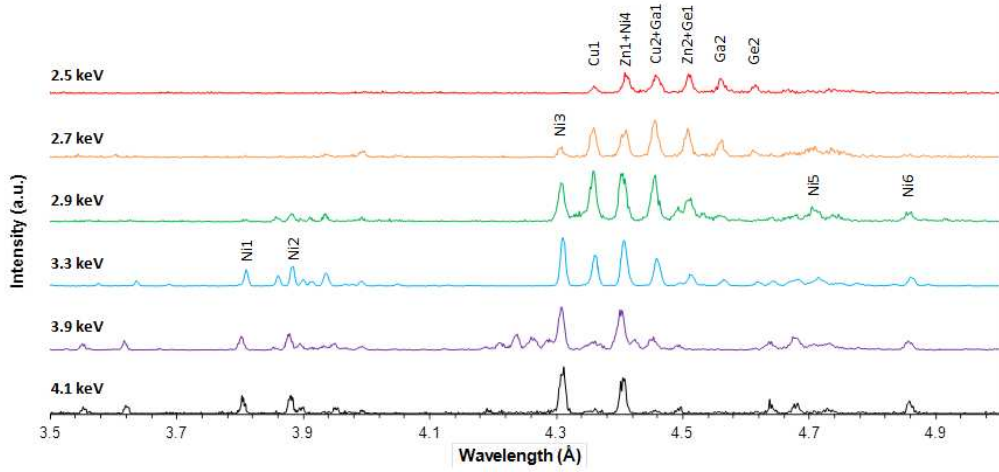


Figure 3.2: Spectra of W on EBIT-I at varying electron beam energies with lines labeled in accordance with Table 3.2. Continuation of these spectra for wavelengths $> 5 \text{ \AA}$ is given in Fig. 3.3. (Osborne 2010)

Lines between 6 and 7.2 \AA were identified by Mandelbaum et al. (Mandelbaum 1983), produced by a 2.5 ns, 15J, Nd glass laser. The majority of lines identified were assigned to the $4d \rightarrow 3p$, $4p \rightarrow 3d$ and $4s \rightarrow 3p$ transitions. They assigned the blended feature that we observed at $6.218 \pm 0.013 \text{ \AA}$ to the Cu-like $3p^6 3d^{10} 4p - 3p^5 3d^{10} 4s 4p$ array at $6.216 \pm 0.003 \text{ \AA}$ (Mandelbaum 1983), which consists of a blend of seven transitions, while Fournier's (Fournier 1998) calculations suggest only a single Zn-like transition at 6.209 \AA . Ionization balance comparisons of experimental EBIT spectra between $E_B = 2.9$ and 2.5 keV suggest close correspondence to Cu-like W, so the results of Mandelbaum et al. (Mandelbaum 1983) are preferred in this paper. The Ni-like $3d^{10} 1S_0 - 3d^9 4p (3/2, 1/2)^o_1$ line we observed at $7.172 \pm 0.015 \text{ \AA}$ was also previously re-measured by Elliot et al. (Elliott 1995) at $7.1733 \pm 0.0003 \text{ \AA}$ using an EBIT.

Measurements made by Neu et al. (Neu 1997) in tokamak plasma confirmed the assignment of the line that Mandelbaum et al. (Mandelbaum 1983) observed at 7.262 \AA to $3d^{10} 4s^2 S_{1/2} - 3d^9 (2D_{3/2}) 4s 4p (1/2, 1/2)^o_1 (3/1, 1)^o_{1/2, 3/2}$ transitions in Cu-like W. Our calculations predict this line to occur at 7.260 \AA , and we observed it at $7.257 \pm 0.016 \text{ \AA}$. Additionally, Neu et al. (Neu 1997) also identified a Ga-like line observed at $7.260 \pm 0.015 \text{ \AA}$, which was confirmed by Kramida and Shirai (Kramida 2009) and designated as $3d^{10} 4s^2 4p^2 P^o_{1/2} -$

Experimental Data from EBIT-I						Kramida and Shirai [20]		
Name	λ (Å)	Intensity (norm.)					λ (Å)	Transition
		2.5 keV	2.7 keV	2.9 keV	3.3 keV	3.9 keV		
Ni1	3.802				0.041	0.020	3.803	$3d^{10}({}^1S_0) - 3d^96f(3/2,5/2)^{\circ}_1$
Ni2	3.874			0.012	0.054	0.033	3.877	$3d^{10}({}^1S_0) - 3d^96f(5/2,7/2)^{\circ}_1$
Ni3	4.307		0.042	0.153	0.171	0.148	4.309	$3d^{10}{}^1S_0 - 3d^95f(3/2,5/2)^{\circ}_1$
Co1	4.309						4.309	$3d^92D_{5/2} - 3d^8({}^1D_2)5f(2,5/2)^{\circ}_{5/2}$ $3d^92D_{5/2} - 3d^8({}^3F_4)5f(4,7/2)^{\circ}_{3/2}$ $3d^92D_{3/2} - 3d^8({}^3F_3)5f(3,7/2)^{\circ}_{3/2}$ $3d^92D_{5/2} - 3d^8({}^3F_4)5f(4,7/2)^{\circ}_{7/2}$
Cu1	4.355	0.030	0.116	0.199	0.082		4.359	$3d^{10}4p^2P^{\circ}_{1/2} - 3d^94p(3/2,1/2)^{\circ}_15f(1,5/2)_{3/2}$ $3d^{10}4s^2S_{1/2} - 3d^94s(3/2,1/2)_15f(1,5/2)^{\circ}_{3/2}$
Zn1	4.402	0.081	0.108	0.190	0.177	0.155	4.411	$3d^{10}4s^2{}^1S_0 - 3d^9({}^2D_{3/2})4s^25f(3/2,5/2)^{\circ}_1$
Ni4							4.406	$3d^{10}{}^1S_0 - 3d^95f(5/2,7/2)^{\circ}_1$
Cu2	4.455	0.072	0.145	0.182	0.081		4.457	$3d^{10}4p^2P^{\circ}_{1/2} - 3d^94s(5/2,1/2)^{\circ}_25f(2,7/2)_{3/2}$ $3d^{10}4s^2S_{1/2} - 3d^94s(5/2,1/2)_25f(2,7/2)^{\circ}_{3/2}$
Ga1							4.457	$3d^{10}4s^24p^2P^{\circ}_{1/2} - 3d^94s^24p(3/2,1/2)^{\circ}_15f(1,5/2)_{3/2}$ $3d^{10}4s^24p^2P^{\circ}_{1/2} - 3d^94s^24p(3/2,1/2)^{\circ}_25f(2,5/2)_{1/2}$
Zn2	4.510	0.071	0.114	0.094	0.026		4.507	$3d^{10}4s^2{}^1S_0 - 3d^9({}^2D_{5/2})4s^25f(5/2,7/2)^{\circ}_1$
Ge1							4.507	$3d^{10}4s^24p^2{}^3P_0 - 3d^9({}^2D_{3/2})4s^24p^2({}^3P_0)(3/2,0)_{3/2}5f(3/2,5/2)^{\circ}_1$
Ga2	4.564	0.031	0.026	0.012			4.564	$3d^{10}4s^24p^2P^{\circ}_{1/2} - 3d^94s^24p(5/2,1/2)^{\circ}_35f(3,7/2)_{1/2}$ $3d^{10}4s^24p^2P^{\circ}_{1/2} - 3d^94s^24p(5/2,1/2)^{\circ}_25f(2,7/2)_{3/2}$
Ge2	4.617	0.005	0.005				4.620	$3d^{10}4s^24p^2{}^3P_0 - 3d^9({}^2D_{5/2})4s^24p^2({}^3P_0)(5/2,0)_{5/2}5f(5/2,7/2)^{\circ}_1$

Table 3.2: $3d \rightarrow 5l$ and $3d \rightarrow 6l$ line identifications for EBIT spectra at various electron beam energies with comparisons to existing tables by Kramida and Shirai (Kramida 2009). If no intensity is given, the line is blended with the one above it. Uncertainties for experimental EBIT data are discussed in the text in section III. Estimated uncertainties for all wavelengths listed from (Kramida 2009) were between ± 0.002 and ± 0.005 Å (see text). (Osborne 2010)

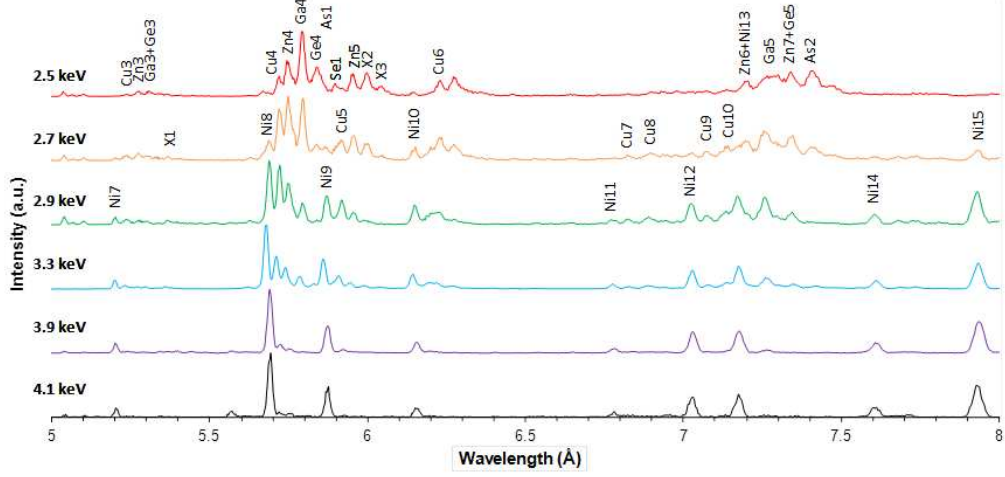


Figure 3.3: Spectra of W on EBIT-I at varying electron beam energies with lines labeled in accordance with Table 3.1 and 3.2. (Osborne 2010)

$3d^9(2D_{5/2})4s^24p^2(1D_2) (5/2,2)_{1/2}$. A possible candidate for the line at $7.344 \pm 0.016 \text{ \AA}$ was classified by Mandelbaum et al. (Mandelbaum 1983) as a band at 7.332 \AA , but Kramida and Shirai (Kramida 2009) were unable to confirm this assignment using Cowan's codes. R. Neu et al. (Neu 1997) also identified a line much closer at $7.340 \pm 0.015 \text{ \AA}$ as a blend of Ge- and Zn-like W transitions, which were assigned by Kramida and Shirai (Kramida 2009) as $3p^63d^{10}4s^24p^2 \ ^3P_0 - 3p^63d^9(2D_{5/2})4s^24p^3(2P^o_{3/2}) (5/2,3/2)_{0_1}$ and $3d^{10}4s^2 \ ^1S_0 - 3d^9(2D_{3/2})4s^24p (3/2,1/2)_{0_1}$.

Ralchenko et al. (Ralchenko 2006) identified the line they observed at $7.607(6) \text{ \AA}$ as a Ni-like transition. Clementson et al. (Clementson 2010) recently re-measured this line at $7.6073(14) \text{ \AA}$. We observed it at $7.604 \pm 0.016 \text{ \AA}$. The line we measured at $7.929 \pm 0.017 \text{ \AA}$ was first observed in tokamak plasma by Neu et al. (Neu 1997) and identified as the electric quadrupole transition $3d^{10} \ ^1S_0 - 3d^94s (5/2,1/2)_2$ at 7.93 \AA . Earlier investigation by Beiersdorfer (Beiersdorfer 1991) had found that the line is also accompanied by a second energetically close dipole-forbidden magnetic octupole transition. Ralchenko et al. (Ralchenko 2006) later concluded that this forbidden line was due to a blend of two closely spaced transitions. This line pair continues to be the subject of much attention, including a discussion in the more recent paper by Clementson et al. (Clementson 2010) where it was re-measured at $7.9280(6) \text{ \AA}$ and $7.9374(7) \text{ \AA}$.

Experimental Data from EBIT-I							Kramida and Shirai [20]	
Label	λ (Å)	Intensity (norm.)					λ (Å)	Transition
		2.5 keV	2.7 keV	2.9 keV	3.3 keV	3.9 keV		
Ni5	4.682			0.026	0.019	0.024	4.680	$3s^23p^63d^{10}5s_0 - 3s3p^63d^{10}4p (1/2,1/2)^{\circ}_1$
Ni6	4.860			0.029	0.036	0.021	4.857	$3p^63d^{10}5s_0 - 3p^53d^{10}4f (3/2,7/2)_2$
Ni7	5.199		0.042	0.126	0.138	0.157	5.1963	$3p^63d^{10}5s_0 - 3p^53d^{10}4d (3/2,5/2)^{\circ}_1$
Cu3	5.238	0.034	0.083	0.085	0.058	0.029	5.2350	$3p^63d^{10}4s^25_{1/2} - 3p^5(^2P^{\circ}_{3/2})3d^{10}4s4d (1/2,5/2)_3 (3/2,3)_{3/2}$
Zn3	5.280	0.045	0.083	0.071	0.026		5.2723	$3p^63d^{10}4s^25s_0 - 3p^5(^2P^{\circ}_{3/2})3d^{10}4s^24d (3/2,5/2)^{\circ}_1$
Ga3	5.304	0.085	0.078	0.052	0.032		5.302	$3p^63d^{10}4s^24p^2P^{\circ}_{1/2} - 3p^53d^{10}4s^24p (3/2,1/2)_24d (1,5/2)_{3/2}$
Ge3							5.3134	$3p^63d^{10}4s^24p^2D_2 - 3p^5(^2P^{\circ}_{3/2})3d^{10}4s^24p^2(^1D_2) (3/2,2)_{3/2}4d (3/2,5/2)^{\circ}_2$
X1	5.369	0.034	0.045	0.048	0.022			
Ni8	5.687	0.075	0.319	1.000	1.000	1.000	5.6900	$3d^{10}5s_0 - 3d^94f (3/2,5/2)^{\circ}_1$
Cu4	5.722	0.341	0.771	0.931	0.512	0.174	5.7192	$3d^{10}4s^25_{1/2} - 3d^94s (3/2,1/2)_14f (1,5/2)^{\circ}_{3/2}$
Zn4	5.749	0.527	1.000	0.646	0.309	0.065	5.7471	$3d^{10}4s^25s_0 - 3d^9(^2D_{3/2})(4s4p_{3/2})^{\circ}_14d_{3/2} (1,3/2)^{\circ}_{1/2} (3/2,1/2)^{\circ}_1$
Co2							5.7482	$3d^92D_{5/2} - 3d^8(^1D_2)4f (2,7/2)^{\circ}_{7/2}$
Ga4	5.792	1.000	0.964	0.346	0.169		5.7951	$3d^{10}4s^24p^2P^{\circ}_{1/2} - 3d^94s^24p (3/2,1/2)^{\circ}_24f (1,5/2)_{3/2}$
Ge4	5.842	0.744	0.626	0.150			5.8378	$3d^{10}4s^24p^23P_0 - 3d^9(^2D_{5/2})4s^24p^2(^3P_1) (5/2,1)_{5/2}4f (5/2,5/2)^{\circ}_1$
As1	5.853	0.335	0.170				5.8551	$3d^{10}4s^24p^32D^{\circ}_{3/2} - 3d^9(^2D_{3/2})4s^24p^3(^2P^{\circ}_{3/2}) (3/2,3/2)_34f (3,5/2)_{1/2}$
Ni9	5.870		0.223	0.454	0.454	0.412	5.8665	$3d^{10}5s_0 - 3d^94f (5/2,7/2)^{\circ}_1$
Se1	5.896	0.201	0.201	0.148	0.120	0.041	5.8929	$3d^{10}4s^24p^43P_2 - 3d^9(^2D_{5/2})4s^24p^4(^3P_2) (3/2,2)_{7/2}4f (7/2,5/2)^{\circ}_2$ $3d^{10}4s^24p^43P_2 - 3d^9(^2D_{5/2})4s^24p^4(^3P_2) (3/2,2)_{3/2}4f (3/2,5/2)^{\circ}_3$ $3d^{10}4s^24p^43P_2 - 3d^9(^2D_{5/2})4s^24p^4(^3P_2) (3/2,2)_{7/2}4f (7/2,5/2)^{\circ}_1$
Cu5	5.918	0.175	0.305	0.386	0.192	0.025	5.9127	$3d^{10}4s^25_{1/2} - 3d^94s (5/2,1/2)_24f (2,7/2)^{\circ}_{3/2}$ $3d^{10}4s^25_{1/2} - 3d^94s (5/2,1/2)_34f (3,7/2)^{\circ}_{1/2}$
*Zn5	5.959	0.299	0.336	0.198	0.078		5.9545	$3d^{10}4s^25s_0 - 3d^9(^2D_{5/2})4s^24f (5/2,7/2)_1$
X2	6.000	0.332	0.208	0.065	0.046	0.014		

Table 3.3: $3I \rightarrow 4I'$ line identifications for EBIT spectra at various electron beam energies with comparisons to existing tables by Kramida and Shirai (Kramida 2009). (*) denotes a line identified by J. Clementson (Clementson 2010) that was not included in (Kramida 2009). If no intensity is given, the line is blended with the one above it. Uncertainties for experimental EBIT data are discussed in the text in section III. Estimated uncertainties for all wavelengths listed from (Kramida 2009) were between ± 0.002 and ± 0.005 Å (see text). (Osborne 2010)

Experimental Data from EBIT-I						Kramida and Shirai [20]		
Label	λ (Å)	Intensity (norm.)					λ (Å)	Transition
		2.5 keV	2.7 keV	2.9 keV	3.3 keV	3.9 keV		
Ni10	6.151	0.036	0.208	0.309	0.232	0.126	6.155	$3p^6 3d^{10} 1s_0 - 3p^5 3d^{10} 4s (3/2, 1/2)^{\circ}_1$
Cu6	6.218	0.245	0.350	0.194	0.083		6.216	$3p^6 3d^{10} 4p^2 P_{1/2} - 3p^5 ({}^2P_{3/2}) 3d^{10} 4s 4p (1/2, 1/2)^{\circ}_1 (3/2, 1)_{1/2}$ $3p^6 3d^{10} 4p^2 P_{1/2} - 3p^5 ({}^2P_{3/2}) 3d^{10} 4s 4p (1/2, 1/2)^{\circ}_1 (3/2, 1)_{3/2}$ $3p^6 3d^{10} 4p^2 P_{3/2} - 3p^5 ({}^2P_{3/2}) 3d^{10} 4s 4p (1/2, 3/2)^{\circ}_2 (3/2, 2)_{5/2}$
X3	6.277	0.290	0.237	0.084				
Ni11	6.775			0.072	0.072	0.077	6.779	$3d^{10} 1s_0 - 3d^9 4p (3/2, 3/2)^{\circ}_1$
Cu7	6.824		0.055	0.049	0.016		6.827	$3d^{10} 4s^2 S_{1/2} - 3d^9 ({}^2D_{3/2}) 4s 4p (1/2, 3/2)^{\circ}_1 (3/2, 1)_{1/2}$
Co3							6.827	$3d^9 {}^2D_{5/2} - 3d^8 ({}^1D_2) 4p (2, 3/2)^{\circ}_{5/2}$
Cu8	6.893		0.072	0.080	0.027		6.884	$3d^{10} 4s^2 S_{1/2} - 3d^9 ({}^2D_{3/2}) 4s 4p (1/2, 3/2)^{\circ}_2 (3/2, 2)_{3/2}$
Ni12	7.024		0.097	0.297	0.255	0.270	7.028	$3d^{10} 1s_0 - 3d^9 4p (5/2, 3/2)^{\circ}_1$
Cu9	7.077		0.093	0.106	0.038		7.075	$3d^{10} 4p^2 P_{3/2} - 3d^9 ({}^2D_{5/2}) 4p^2 (3/2, 3/2)_2 (5/2, 2)_{3/2}$ $3d^{10} 4p^2 P_{3/2} - 3d^9 ({}^2D_{5/2}) 4p^2 (3/2, 3/2)_2 (5/2, 2)_{5/2}$ $3d^{10} 4s^2 S_{1/2} - 3d^9 ({}^2D_{5/2}) 4s 4p (1/2, 3/2)^{\circ}_1 (5/2, 1)^{\circ}_{3/2}$
Cu10	7.138		0.237	0.271	0.112		7.137	$3d^{10} 4s^2 S_{1/2} - 3d^9 ({}^2D_{5/2}) 4s 4p (1/2, 3/2)^{\circ}_2 (5/2, 2)^{\circ}_{3/2}$
Zn6	7.172	0.228	0.275	0.448	0.305	0.307	7.162	$3d^{10} 4s 4p (1/2, 3/2)^{\circ}_2 - 3d^9 ({}^2D_{5/2}) 4s 4p^2 ({}^3P_2) (1/2, 2)_{5/2} (5/2, 5/2)_3$ $3d^{10} 4s 4p (1/2, 1/2)^{\circ}_1 - 3d^9 ({}^2D_{5/2}) 4s 4p^2 ({}^1D_2) (1/2, 2)_{3/2} (1/2, 3/2)_2$ $3d^{10} 4s 4p (1/2, 3/2)^{\circ}_1 - 3d^9 ({}^2D_{5/2}) 4s 4p^2 ({}^3P_2) (1/2, 2)_{3/2} (5/2, 3/2)_2$
Ni13							7.1733	$3d^{10} 1s_0 - 3d^9 4p (3/2, 1/2)^{\circ}_1$
Ga5	7.257	0.319	0.426	0.434	0.167	0.029	7.26	$3d^{10} 4s^2 4p^2 P_{1/2} - 3d^9 ({}^2D_{5/2}) 4s^2 4p^2 ({}^1D_2) (5/2, 2)_{1/2}$ $3d^{10} 4s^2 4p^2 P_{1/2} - 3d^9 ({}^2D_{5/2}) 4s^2 4p^2 ({}^1D_2) (5/2, 2)_{3/2}$
Cu11							7.262	$3d^{10} 4s^2 S_{1/2} - 3d^9 ({}^2D_{3/2}) 4s 4p (1/2, 1/2)^{\circ}_1 (3/1, 1)^{\circ}_{1/2, 3/2}$
Ge5	7.344	0.339	0.389	0.199	0.051		7.340	$3d^{10} 4s^2 4p^2 {}^3P_0 - 3d^9 ({}^2D_{5/2}) 4s^2 4p^2 ({}^3P_{3/2}) (5/2, 3/2)^{\circ}_1$
Zn7							7.332	$3d^{10} 4s 4p (1/2, 3/2)^{\circ}_2 - 3d^9 ({}^2D_{3/2}) 4s 4p^2 ({}^1D_2) (1/2, 2)_{5/2} (3/2, 5/2)_1$ $3d^{10} 4s 4p (1/2, 1/2)^{\circ}_1 - 3d^9 ({}^2D_{3/2}) 4s 4p^2 ({}^3P_0) (1/2, 0)_{1/2} (3/2, 1/2)_2$ $3d^{10} 4s 4p (1/2, 3/2)^{\circ}_1 - 3d^9 ({}^2D_{3/2}) 4s 4p^2 ({}^3P_1) (1/2, 1)_{1/2} (3/2, 1/2)_1$ $3d^{10} 4s 4p (1/2, 3/2)^{\circ}_1 - 3d^9 ({}^2D_{3/2}) 4s 4p^2 ({}^3P_1) (1/2, 1)_{1/2} (3/2, 1/2)_2$ $3d^{10} 4s^2 1s_0 - 3d^9 ({}^2D_{3/2}) 4s^2 4p (3/2, 1/2)^{\circ}_1$
As2	7.411	0.388	0.171	0.031	0.030		7.410	$3d^{10} 4s^2 4p^3 - 3d^9 4s^2 4p^4$
Ni14	7.604		0.026	0.168	0.142	0.127	7.607	$3d^{10} 1s_0 - 3d^9 4s (3/2, 1/2)_2$
Ni15	7.929		0.126	0.520	0.372	0.462	7.930	$3d^{10} 1s_0 - 3d^9 4s (5/2, 1/2)_2$
Zn8	8.172	0.121	0.131	0.138	0.045		8.15	$3d^{10} 4s 4p (1/2, 1/2)^{\circ}_1 - 3d^9 ({}^2D_{5/2}) 4s^2 4p (5/2, 1/2)^{\circ}_3$ $3d^{10} 4s 4p (1/2, 1/2)^{\circ}_1 - 3d^9 ({}^2D_{5/2}) 4s^2 4p (5/2, 1/2)^{\circ}_2$

Table 3.4: Table 3.3 contd. (Osborne 2010)

There are three lines that remain unidentified in our observed spectra, and they are labeled in Table 2 as X1 to X3 with wavelengths 5.369 ± 0.012 , 6.000 ± 0.013 , and 6.277 ± 0.014 Å. A method for identifying these lines using charge state balancing is presented and discussed in detail in section 3.3.

3.2 Modeling of M-Shell W

Each ion species was modeled separately using the Hebrew University Lawrence Livermore Atomic Code (HULLAC) (Safronova 2000). This allowed for an extremely large number of calculated transitions. The relativistic version of HULLAC's parametric potential method, including multi-configuration interactions, was employed to calculate intermediate-coupling detailed level energies. Existing identifications of prominent lines in experimental EBIT spectra were used to determine appropriate target states, which were used to define the ion transitions included in the model calculations. Collisional strengths and decay rates were calculated between all pairs of these defined target states for Co-, Ni-, Cu-, Zn-, Ga-, and Ge-like W ions. Lines were artificially broadened using a Doppler profile fit,

$$\phi(v) = \frac{1}{v_D \sqrt{\pi}} e^{\left(\frac{v-v_0}{v_D}\right)^2} \quad (3.1)$$

$$v_D = v_0 \sqrt{\frac{2T_{ion}}{Mc^2}}, \quad (3.2)$$

where T_{ion} is the ion temperature, M is the ion mass, and v_0 is the initial ion velocity $v_0 = \Delta E/h$, to keep them consistent with EBIT spectra for benchmarking purposes.

Cross sections are calculated from the collisional strengths generated by HULLAC using the formula

$$\sigma_{if} = \frac{R_y \pi a_0^2}{g_i \varepsilon} \Omega_{if} \text{ (cm}^2\text{)}, \quad (3.3)$$

where i and f are indexes for the initial and final states, respectively, R_y is the Rydberg constant, a_0 is the Bohr radius, g is the statistical weight, ε is the initial energy of the impact

electron, and Ω is the collisional strength. The excitation rate is then calculated using

$$\langle v\sigma_{if} \rangle = \int v\sigma_{if}(\varepsilon)F(\varepsilon)d\varepsilon \text{ (cm}^3\text{s}^{-1}\text{)}, \quad (3.4)$$

where ε is again the impact electron energy, v is the impact electron velocity

$$v = \sqrt{\frac{2\varepsilon}{m_e}} \left(\frac{\text{cm}}{\text{s}}\right), \quad (3.5)$$

and $F(\varepsilon)$ is the electron energy distribution function, which, in the case of the charge-limiting electron beam of the EBIT, is approximated by the delta function

$$F(\varepsilon) = \delta(\varepsilon - \varepsilon_0). \quad (3.6)$$

Collisional de-excitation is calculated from the collisional cross section using the Klein-Rosseland formula

$$g_f\varepsilon\sigma_{if}^{dex}(\varepsilon + \Delta E)\sigma_{fi}^{ex}(\varepsilon + \Delta E) \text{ (s}^{-1}\text{)}, \quad (3.7)$$

where ΔE is the change in energy from states f to i ,

$$\Delta E = E_f - E_i \text{ (keV)}. \quad (3.8)$$

Since recombination rates and other complex atomic processes are negligible in the high energy regime where $3d \rightarrow 5l$ transitions are being calculated, the total steady-state population of each level can be estimated accurately using only the radiative decay rates (A_{if}^{rad}) and the collisional excitation (Eq. 3.3) and de-excitation (Eq. 3.7) rates:

$$X_i = A_{if}^{rad} + \sigma_{if}^{dex} - \sigma_{if}^{ex}. \quad (3.9)$$

This creates a square matrix as large as the number of levels being considered for calculation that becomes solvable (and normalized) by setting the population of the highest level to 1 and removing its associated row and column. Once the populations have been found, the

total energy emission between levels i and f can be calculated for an optically thin plasma over 4π steradians as

$$n_{ion}X_iA_{if}^{rad}hv_{if}, \quad (3.10)$$

which means that with line profiling taken into consideration, the spectral intensity can be calculated as the sum of the contributions from each decay at any given energy:

$$I(E) = n_{ion} \sum X_iA_{if}^{rad}hv_{if}\phi(v). \quad (3.11)$$

As the $E_B = 4.1$ keV EBIT spectrum was evaluated as having primarily Ni-like transitions (with very small contributions from Co-like W), it was the simplest to model with the best benchmark available for early development of theoretical modeling, which was published in (Osborne 2008). From there, the EBIT spectra become increasingly complex as the corresponding electron beam energy is lowered, with $E_B = 3.9$ keV introducing traces of Cu-like ions, $E_B = 3.3$ keV introducing Zn-like ions, and so on. In particular, the spectra below $E_B = 3.3$ keV have the highest variety of ion species, with the $E_B = 2.7$ keV spectrum showing noticeable concentrations of all modeled ions and the $E_B = 2.5$ keV spectrum even displaying weak contributions by Se-like and As-like W. A more detailed analysis of these charge concentrations is discussed in section 3.3.

3.3 Charge State Balancing of W Ions

To calculate charge balance, each ionization state was modeled independently and then summed together, after which scaling coefficients for intensity were determined. The modeled absolute intensities for each ionization state were also compared against normalized percentage-based values. All charge balancing for EBIT spectra was done between 4 and 5 Å for $3d \rightarrow 5l$ transitions, primarily due to these lines being relatively optically thin in z -pinch plasma and more easily discernible than the $3d \rightarrow 4l$ transitions that are also observed. Because individual counts for the EBIT microcalorimeter spectra are not meaningful, the experimental data was normalized and charge states were balanced against relative intensity.

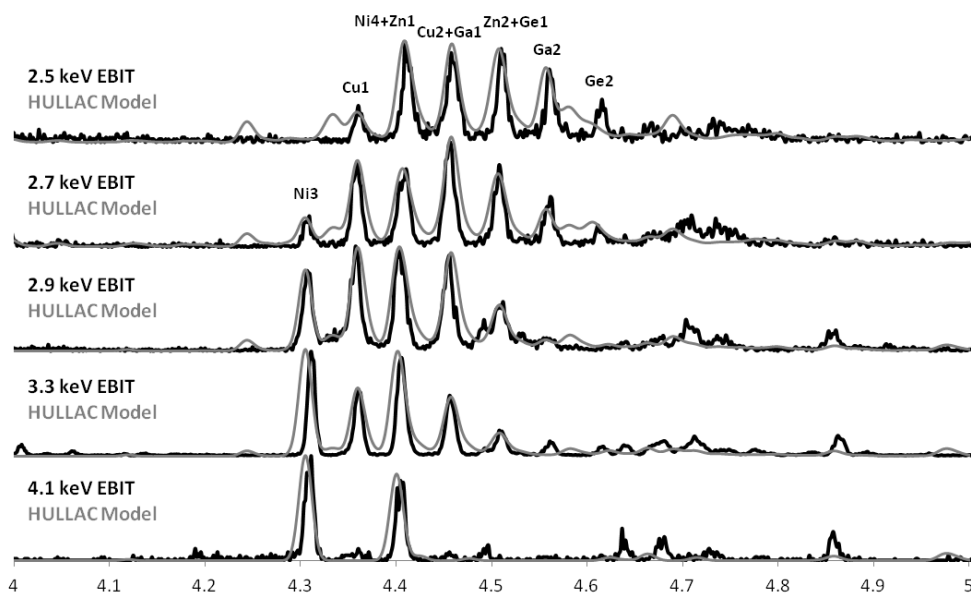


Figure 3.4: $3d \rightarrow 5l$ model fitting and charge state balancing for EBIT-I spectra of various electron beam energies. Vertical axis is scaled linearly. (Osborne 2010)

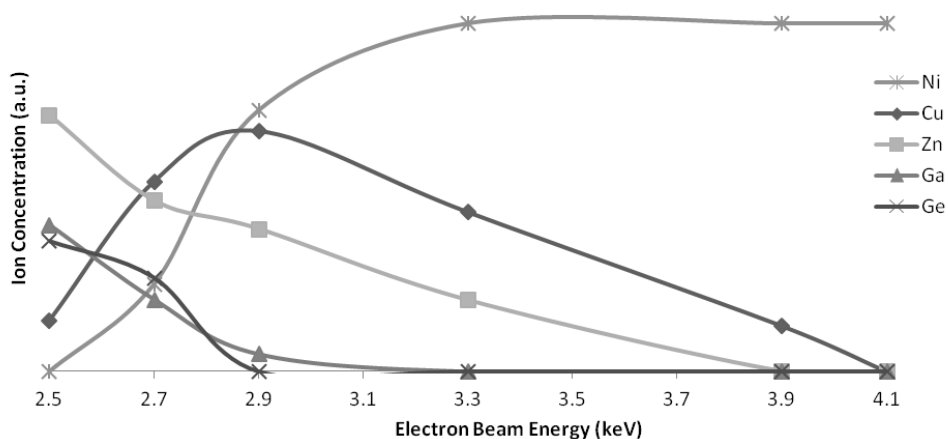


Figure 3.5: Fractional populations of prominent ion species in EBIT-I spectra, derived using synthesized spectra calculated by HULLAC. Vertical axis is scaled linearly. (Osborne 2010)

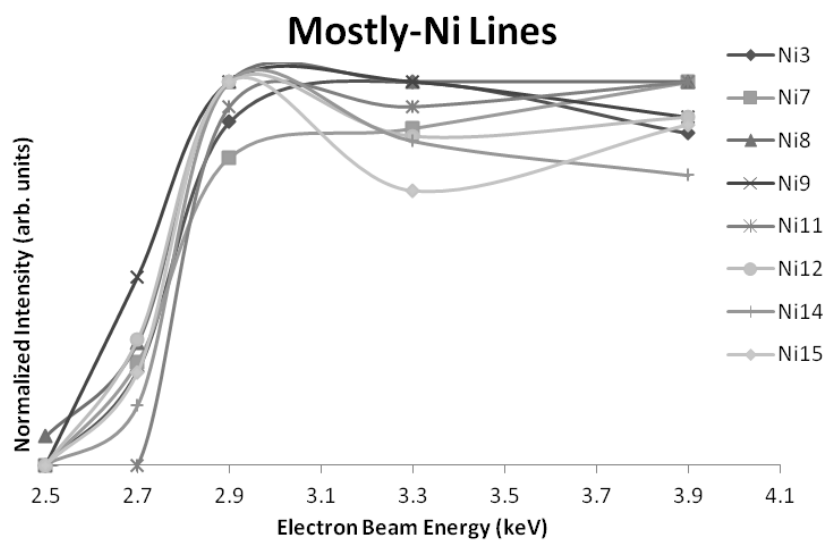


Figure 3.6: Trends of independently normalized observed intensities of Ni-like W lines in EBIT-I spectra of various electron beam energies. Vertical axis is scaled linearly. (Osborne 2010)

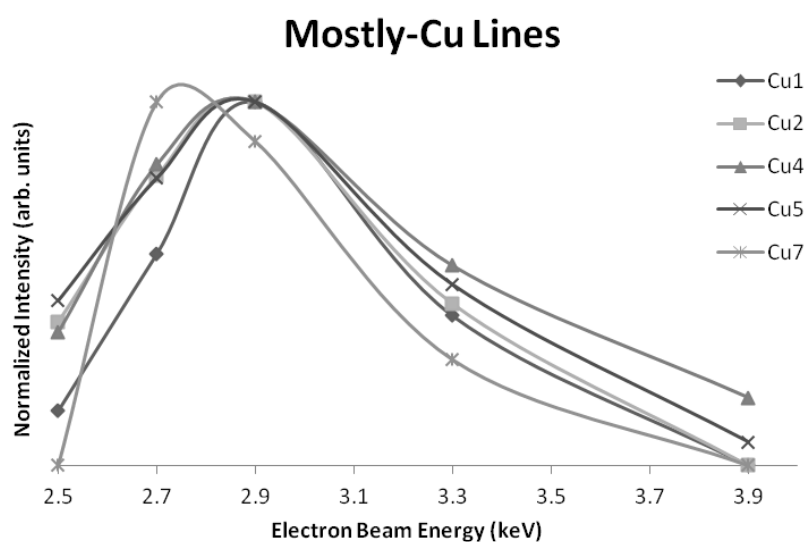


Figure 3.7: Trends of independently normalized observed intensities of Cu-like W lines in EBIT-I spectra of various electron beam energies. Vertical axis is scaled linearly. (Osborne 2010)

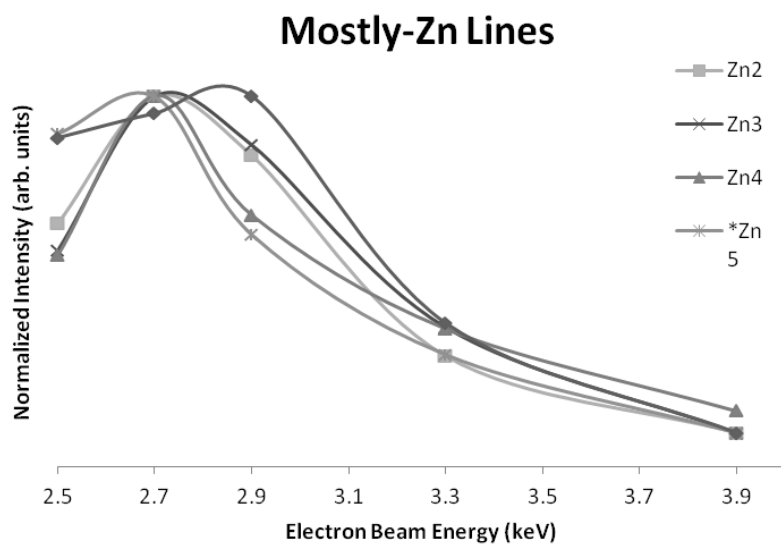


Figure 3.8: Trends of independently normalized observed intensities of Zn-like W lines in EBIT-I spectra of various electron beam energies. Vertical axis is scaled linearly. (Osborne 2010)

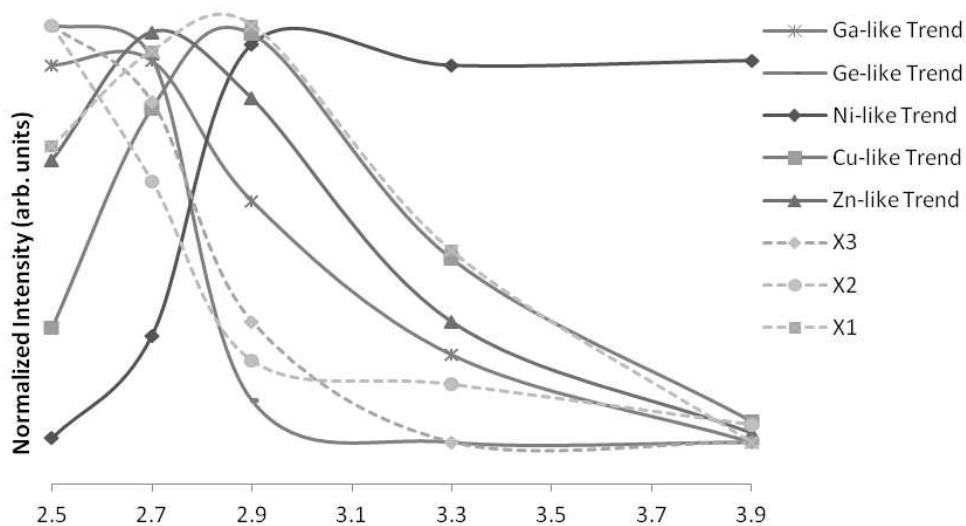


Figure 3.9: Normalized intensities of unknown lines compared to averaged balancing trends of prominent ions in EBIT-I spectra at various electron beam energy. Vertical axis is scaled linearly. (Osborne 2010)

E_B (keV)	Ni	Cu	Zn	Ga	Ge	$\langle Z \rangle$
2.5	0.000	0.087	0.439	0.251	0.223	43.5
2.7	0.142	0.309	0.279	0.118	0.153	44.2
2.9	0.395	0.363	0.215	0.265	0.000	45.0
3.3	0.602	0.275	0.123	0.000	0.000	45.4
3.9	0.884	0.116	0.000	0.000	0.000	45.8
4.1	1.000	0.000	0.000	0.000	0.000	46.0

Table 3.5: Theoretical fractional populations of prominent ion species in EBIT-I spectra of various electron beam energies shown in Fig. 3.4.

Results from this charge balancing method for appropriate electron beam energies are shown in Fig. 3.4, with Table 3.5 showing the numerical values for each calculated coefficient and the total average ionization charge per corresponding beam energy. A graphical comparison of these coefficients is shown in Fig. 3.5. The average ionization charge was calculated for each of these ions using by summing the contributions of each individual species, or more specifically,

$$\langle Z \rangle = \sum_i Z_i X_i, \quad (3.12)$$

where Z_i is the ion charge and X_i is its fractional population. It is of particular note that the spectra corresponding to electron beam energies of 2.9 and 3.3 keV have small variations in their average ion charge, despite their prominent features being significantly different.

Independently normalized intensities for non-blended lines (or lines with very small blending) are graphed in Figs. 3.6, 3.7, and 3.8 for Ni-like, Cu-like, and Zn-like W, respectively, for the purpose of analyzing trends of ionization balance in the experimental EBIT data, particularly to aid in the identification of unknown lines, such as the one at 5.956 Å where conflicting identifications have been made by previous publications. Charge-state balancing of the three unidentified lines in comparison with averaged trends shown in Fig. 3.9 indicates that the 5.367 Å line shows closest correspondence to either Zn or Cu-like W. Both the 6.000 and 6.277 Å lines more closely follow the trend of Ge-like W, however none of these lines could be explained by our current modeling, so no configurations are assigned to them.

4 Z-Pinch Combined Tungsten/Aluminum Spectra

The majority of the spectra used for modeling comparisons and line identifications were from the TIXRS on Zebra (see section 2.1.1). Each film recording had line intensity adjustments made to account for background noise, filters, and film sensitivity, a process that is detailed further in appendix C. Spectrogram tracings from the x-ray films were integrated along the spatially resolved axial direction of the pinch in areas that minimized noise and where the spectral features of interest were most prominent. Like the EBIT spectra, the z-pinch spectra are also normalized to emphasize relative line intensity.

4.1 Aluminum Tracer Wires and Modeling of K-Shell Aluminum Plasma

In many of the experiments done with W wires, a small number of alloyed Al(5056) wires were also included as diagnostic tracers. Al(5056) makes a good tracer for W due to it having K-shell Al and Mg emission lines that are near the M-shell W lines of interest, but without significant overlap. This means that the well-resolved Al and Mg lines can be helpful for wavelength calibrations of the resulting films, particularly in cases where the W lines are not easily discernible. Just as importantly, the more fully developed methods for diagnosing Al data using spectral feature comparisons are useful for determining plasma parameters of the pinch (Yilmaz 2012), and it has also been shown (Safronova 2006) that mixture with a lighter material can produce better quality and resolution M-shell W spectra.

Modeling of Al plasma parameters was done using a variant of the Spectroscopic Collisional-Radiative Atomic Model (SCRAM) (Hansen 2003). In particular, the electron temperature T_e and density n_e were calculated for the Al plasma in each combined Al/W shot. In the cases where the Al plasma was relatively optically thin, the Al lines were modeled directly, but due to

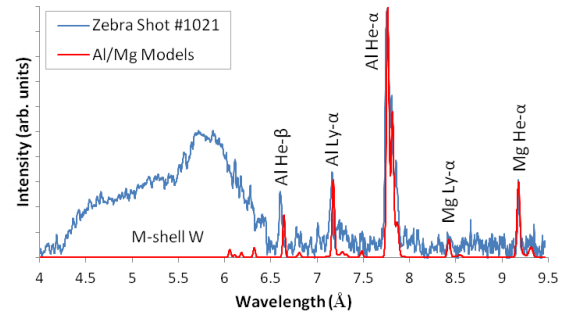


Figure 4.1: Identification and modeling of diagnostically important Al and Mg lines in a combined Al/W Zebra experiment, recorded with the TIXRS.

Ion	Line	Transition	λ (Å)	Ar (s^{-1})
He	Mg He- α	$1s2p\ ^1P_1 \rightarrow 1s^2\ ^1S_0$	9.1695	1.97E+13
H	Mg Ly- α	$2p\ ^2P_{3/2} \rightarrow 1s\ ^2S_{1/2}$	8.4192	1.31E+13
He	Mg He- β	$1s3p\ ^1P_1 \rightarrow 1s^2\ ^1S_0$	7.8507	5.48E+13
He	Mg He- γ	$1s4p\ ^1P_1 \rightarrow 1s^2\ ^1S_0$	7.4733	2.23E+12
H	Mg Ly- β	$3p\ ^2P_{3/2} \rightarrow 1s\ ^2S_{1/2}$	7.1058	3.49E+12
He	Al He- α	$1s2p\ ^1P_1 \rightarrow 1s^2\ ^1S_0$	7.7578	2.78E+13
H	Al Ly- α	$2p\ ^2P_{3/2} \rightarrow 1s\ ^2S_{1/2}$	7.1709	1.80E+13
He	Al He- β	$1s3p\ ^1P_1 \rightarrow 1s^2\ ^1S_0$	6.6349	7.70E+13
He	Al He- γ	$1s4p\ ^1P_1 \rightarrow 1s^2\ ^1S_0$	6.3140	3.10E+13
He	Al He- δ	$1s5p\ ^1P_1 \rightarrow 1s^2\ ^1S_0$	6.1734	1.58E+12
H	Al Ly- β	$3p\ ^2P_{3/2} \rightarrow 1s\ ^2S_{1/2}$	6.0543	4.76E+12

Table 4.1: Transitions of K-shell Al and Mg spectral features prominent in z-pinch experiments, where λ is wavelength and Ar is rate of radiative decay.

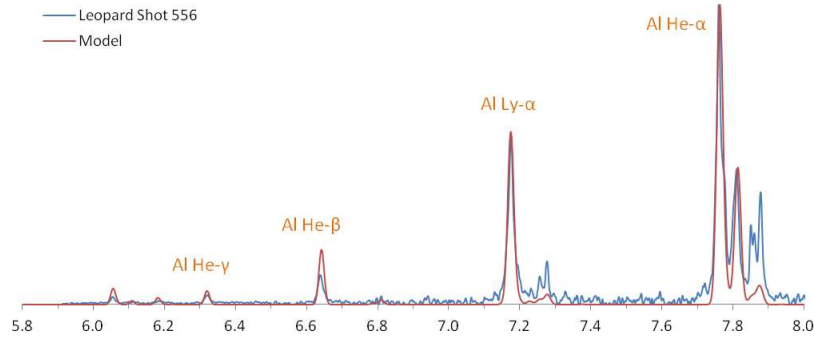


Figure 4.2: Spectrogram tracing from leopard shot #556, a low contrast (10^5) laser shot with pulse length 0.8 ns with a thin pure Al target. Lines are identified in accordance with Table 4.1 with modeling shown.

film saturation caused by opacity, the more

optically thick plasmas had to be analyzed via Mg lines. The most prominent and highly resolved Al and Mg lines observed by the TIXRS for these experiments are shown in Table 4.1, and modeling focused on the He- α , Ly- α , and He- β Al and the He- α and Ly- α Mg lines, which are shown in Fig. 4.1. In this Zebra shot, #1021, electron temperature was calculated to be approximately 475 eV with a density of 5.10^{18} cm^{-3} .

This model was also tested against laser produced plasma from the Leopard laser at NTF, with the intention of benchmarking and ensuring its reliability for simulating different types of plasmas beyond those generated in a z-pinch. The same TIXRS from Zebra was used for the Leopard experiments (with no slit, so there was no spatial resolution) with the same

crystal (KAP), and all procedures for film development, wavelength calibration, and intensity corrections were identical. The results of a spectrogram tracing and the corresponding theoretical modeling are shown in Fig. 4.2. Interestingly, the calculated electron temperature ($T_e = 520$ eV) was higher and the density ($n_e = 4.10^{19}$ cm $^{-3}$) was approximately the same compared to typical z-pinch Al measurements.

4.2 Charge State Balancing of 3d-5l Transitions in Z-Pinch Spectra

Charge state balancing can be a useful diagnostic for z-pinch W plasmas and is important in the analysis of experiments discussed in later sections. As with the charge balancing of EBIT spectra, all ion species were summed together after multiplying by their respective balancing coefficients. The most prominent spectral features that were modeled and balanced from the z-pinch data included Ni3, Ni4, Zn1, Zn2, Cu1, Cu2, Ga1, Ga2, and Ge1 as listed in Table 3.2. A sample of a z-pinch shot taken on Zebra with modeling and balancing of W 3d \rightarrow 5l is shown in Fig. 4.3, where all relevant Al lines have also been identified and labeled. Charge state fractions calculated for this spectrum are 0.329 for Ni-like, 0.208 for Cu-like, 0.149 for Zn-like, 0.173 for Ga-like, and 0.142 for Ge-like W, which corresponds to an average ion charge $\langle Z \rangle = 44.45$.

4.3 Wire Array Plasma Absorption Spectroscopy with Semi-Backlighter Source

Spectroscopic analysis provides a nonintrusive and accurate method for diagnosing electron temperature, electron density, and optical thickness in wire array z-pinch plasmas. One drawback to this, however, is that emission spectra are primarily only produced in the most energetic stages of the z-pinch when the plasma is at its most radiative, which means plasma parameters are more difficult to extract for early and late times. Luckily, absorption spectroscopy offers a method for extracting information at pre- and post-stagnation times, which occur when the backlighting plasma is radiative enough to photoionize the cooler and less dense plasma surrounding it. The radiation field from the inner plasma must be intense enough that photoionization dominates over collision processes in the outer plasma, which

itself must be low density to mitigate collisional excitation. Such conditions have been achieved using combined W/Al single planar wire array (SPWA) loads on Zebra, where a single Al wire is placed on the edge of a row of W wires. This allows the resulting W plasma to act as a semi-backlighter source for Al K-shell absorption features (Osborne 2012). As previous experiments in the generation of absorption features have traditionally used external sources, such as colder laser-produced plasma [see, for example, (Ivanov 2011)], this new method has the advantage of allowing absorption to occur in a single z-pinch load. All Al wires used in these experiment were alloys with a 5% Mg impurity.

The two shots presented in Fig. 4.4 were both of the same configuration, each being an 11-wire single planar array (Kantsyrev 2007) with a $0.7\ \mu\text{m}$ inter-wire gap composed of W wires and, at one end, a single Al wire (for 12 total wires). In shot #1297,

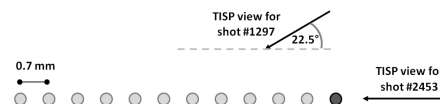


Figure 4.5: Configuration and orientations of spectroscopic diagnostics of Zebra shots #1297 and #2453. Light circles indicate tungsten wires where the dark circle indicates the aluminum tracer. (Osborne 2011)

where absorption lines were observed, the orientation of the load was 22.5° from being parallel to the field of view of the TIXRS, whereas shot #2453 was done exactly parallel to (with the Al wire facing) the spectrometer, as shown in Fig. 4.5. It had $16\ \mu\text{m}$ (linear mass $38.8\ \mu\text{g}/\text{cm}$) diameter W wires and a $30\ \mu\text{m}$ ($19.1\ \mu\text{g}/\text{cm}$) Al wire for a total load mass of $446\ \mu\text{g}/\text{cm}$ where 4.5% was composed of Al. Although the specific mechanics that cause absorption lines in regards to ablation dynamics and the z-pinch lifecycle are not yet fully understood, the purpose of orienting the arrays in this manner is to put the W plasma “behind” the Al wire (as viewed by the TIXRS) and allow it to act as a semi-backlighter for Al K-shell absorption features. Shot #2453 used $8.9\ \mu\text{m}$ W ($111.3\ \mu\text{g}/\text{cm}$) wires and a $49.8\ \mu\text{m}$ Al ($73.6\ \mu\text{g}/\text{cm}$) wire for a total linear mass of $185\ \mu\text{g}/\text{cm}$ and Al concentration of 39.8%. Another primary difference between these two loads is that shot #1297 utilized the LCM, reaching a current maximum of 1.2 MA, whereas shot #2453 was imploded by Zebra in its standard configuration and reached a current maximum of 0.91 MA. Films and positions of spectrogram tracings for both shots are shown in Fig. 4.4 along with corresponding pinhole images.

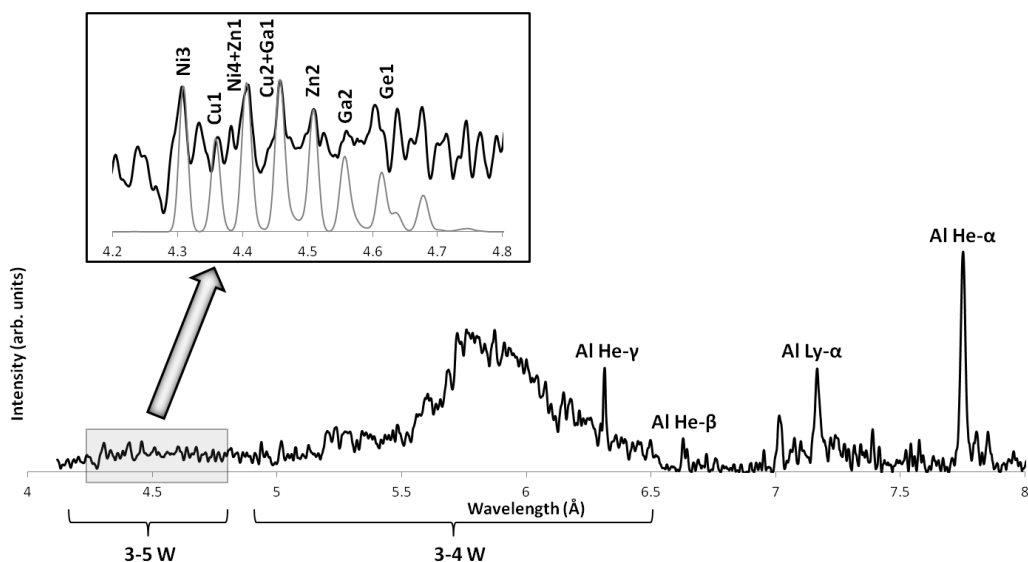


Figure 4.3: Spectrum from z-pinch combined W/Al experiment. Prominent Al lines are indicated and model for charge state balancing of $3d-5l$ transitions is shown. (Osborne 2010)

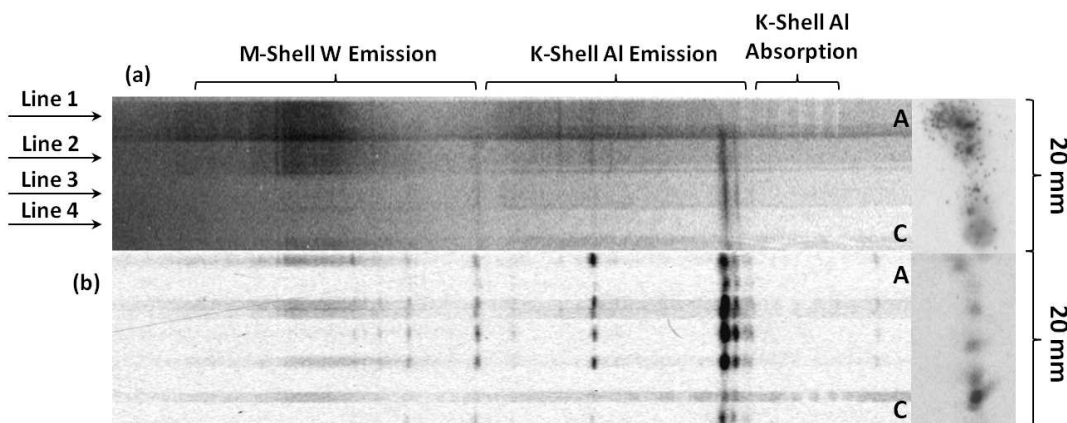


Figure 4.4: Film scans of experimental results from shots (a) #1297 and (b) #2453, with time-integrated spectrometer data on the left. Positions where tracings were taken (shown in Fig. 4.7) are indicated by a corresponding line number, and regions where spectral features are most prominent are indicated above. Pinhole images are shown to the right of their appropriate spectrometer film, with (a) being a time-gated pinhole image and (b) a time-integrated pinhole image. The letters A and C indicate the orientation of the film images, denoting anode and cathode positions, respectively. (Osborne 2011)

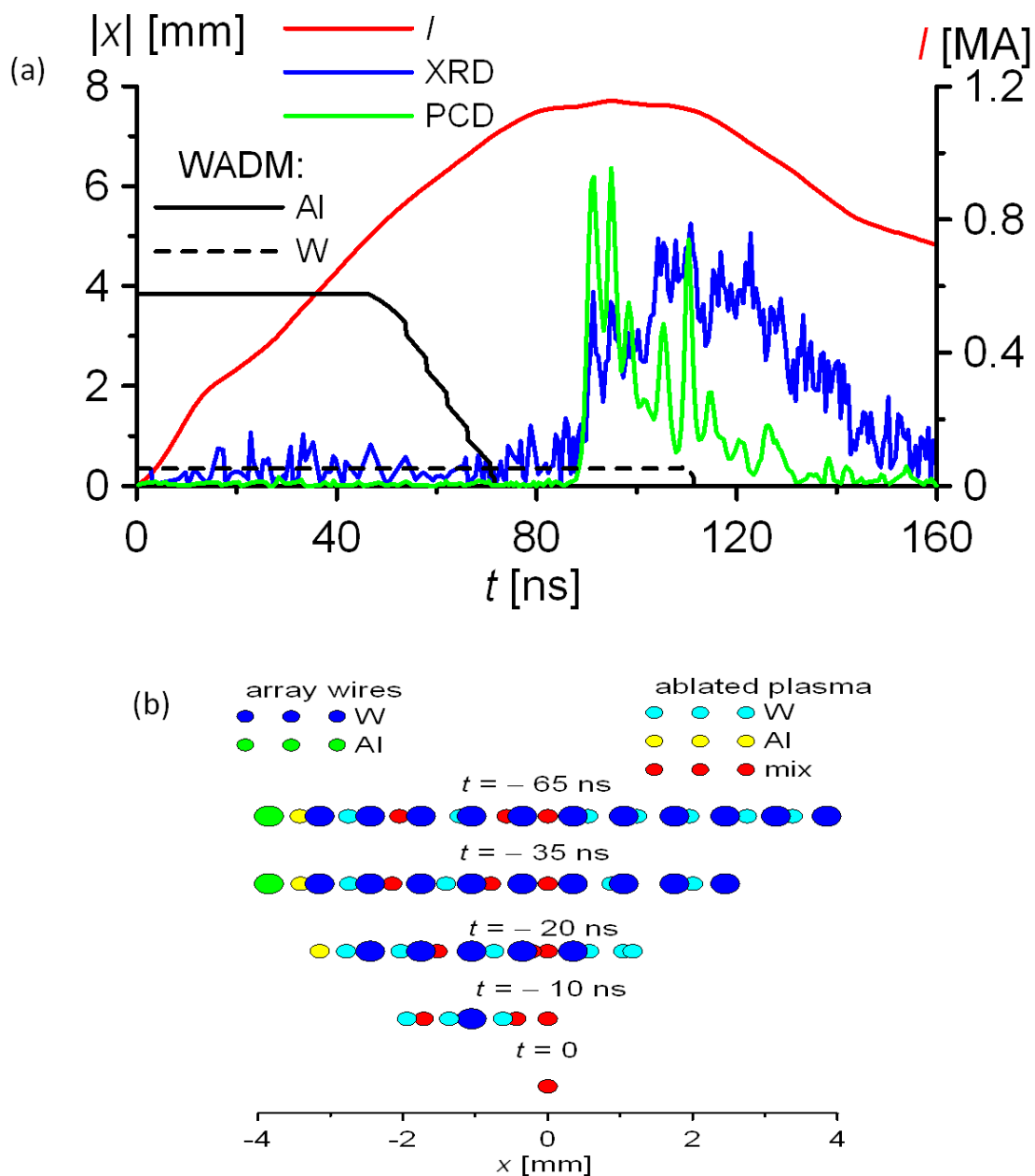


Figure 4.6: Wire Ablation Dynamics Modeling for shot #1297. Experimental signals (XRD, PCD, and Current, as labeled) in (a) use arbitrary units, the estimated absolute value of the maximum distance where wire mass of each material is relative to the center of the array is given on the left axis, and the current scale is shown to the right. The horizontal axis scales the time evolution of the shot from the beginning of the current rise. A graphical representation showing the motion of plasma from each individual wire is given in (b).

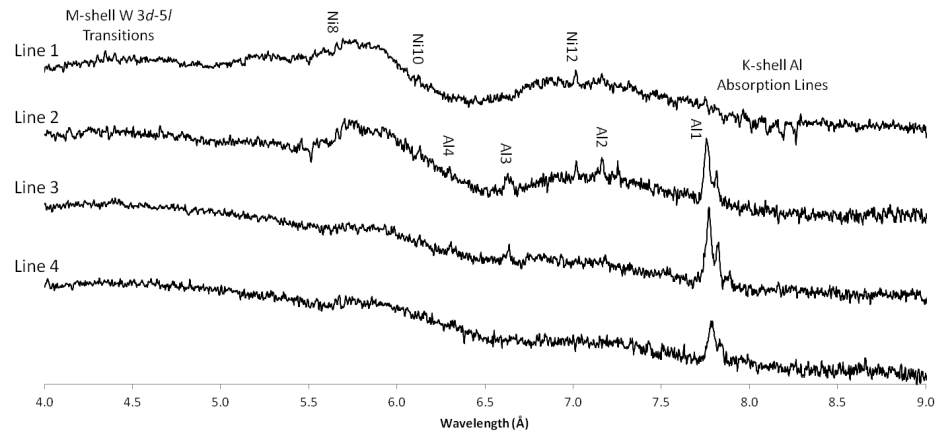


Figure 4.7: Spectrogram tracings of shot #1297 with axial locations as indicated in Fig. 4.4. Prominent lines are labeled accordingly along with groupings of features shown in greater detail in Figs. 4.8 and 4.9. Vertical axis is in arbitrary units. (Osborne 2011)

WADM (Esaulov 2009) calculations were also performed for shot #1297, and are shown in Fig. 4.6. More specifically, Fig. 4.6(a) shows the experimental XRD, PCD, and current signals overlaid with the modeled distance of Al and W plasma from the central axis, and Fig. 4.6(b) gives a graphical representation of the individual wire ablations. As is common with planar array experiments on Zebra, the outer wires receive current first and begin ablating first (see part IV for more details), and this is reflected in the modeling shown. More importantly, however, it shows clearly how the Al wire is ablating completely and moving to axis before the W wires.

One of the most notable features of the two films from shots #1297 and #2453 shown in Fig. 4.4 is that the absorption lines occur spatially in regions of the plasma source where Al K-shell emission lines are least prominent, if they're present at all, indicating a cold Al plasma at those locations. They also accompany areas where M-shell W features are most intense. More specifically, the prominence of $3d \rightarrow 5l$ M-shell W features in the 4-5 Å range suggests a relatively hot W plasma. Comparison with pinhole images also indicates that areas where absorption features occur correspond to sections of the plasma column with high radiation yields.

Spectrogram tracings of shot #1297 are displayed for four different spatial locations throughout the plasma column, as indicated in Fig. 4.4. Each of these tracings are inte-

Label	Ion Species	Wavelength (\AA)	Expected Electron Temp. (eV)
Al1	Al He- α	7.75	150 - 350 eV
Al2	Al Ly- α	7.17	450 - 600 eV
Al3	Al He- β	6.63	150 - 350 eV
Al4	Al He- γ	6.31	150 - 350 eV
Ni3	W Ni	4.31	1000 - 1500 eV
Ni4	W Ni	4.41	1000 - 1500 eV
Ni8	W Ni	5.69	1000 - 1500 eV
Ni10	W Ni	6.16	1000 - 1500 eV
Ni12	W Ni	7.03	1000 - 1500 eV
Cu1	W Cu	4.36	800 - 1000 eV
Cu2	W Cu	4.46	800 - 1000 eV
Zn1	W Zn	4.40	760 - 900 eV
Zn2	W Zn	4.51	760 - 900 eV
Ga1	W Ga	4.56	720 - 850 eV
Ge1	W Ge	4.51	700 - 800 eV

Table 4.2: Listing of prominent spectral emission features found in Fig. 4.7 along with estimations for the electron temperatures each line is commonly found at in Zebra-generated plasmas.

Label	Ion Species	Wavelength (\AA)	Expected Electron Temp. (eV)
Be	Al Be	7.94	20 - 40 eV
B	Al B	8.01	20 - 40 eV
C	Al C	8.10	10 - 40 eV
N	Al N	8.19	10 - 40 eV
O	Al O	8.26	10 - 40 eV

Table 4.3: Listing of prominent spectral absorption features found in Fig. 4.7 along with estimations for the electron temperatures each line is commonly found at in Zebra-generated plasmas.

grated axially over a narrow strip to reduce noise and are shown in Fig. 4.7. Prominent Ni-like W lines that represent the most intense $3d \rightarrow 4l$ M-shell transitions shown are labeled in accordance with a previous publication (Osborne 2011). In particular, line Ni8 is $3d^{10} \ ^1S_0 - 3d^9 4f (3/2, 5/2) \ ^\circ_1$, Ni10 is $3p^6 3d^{10} \ ^1S_0 - 3p^5 3d^{10} 4s (3/2, 1/2) \ ^\circ_1$, and Ni12 is $3d^{10} \ ^1S_0 - 3d^9 4p (5/2, 3/2) \ ^\circ_1$. Al K-shell emission and absorption lines are also defined appropriately. Al1 is the He- α line at 7.75 Å, Al2 is the Ly- α line at 7.17 Å, Al3 is the He- β line at 6.63 Å, and Al4 is the He- γ line at 6.31 Å.

Fig. 4.8 displays Al K-shell absorption in greater detail, with clusters of lines labeled by their respective ionization species (from O-like to Be-like Al) (Ivanov 2011, Renaudin 2006), and the spectrum from line 2 is shown for reference. Comparison with modeling in previous publications (Ivanov 2011) and charge-state balance of absorption features suggests an electron temperature between 10 and 40 eV, which is significantly lower than the expected values for emission lines.

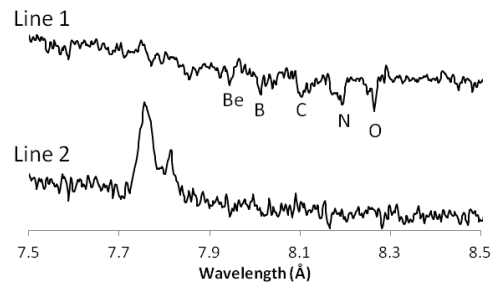


Figure 4.8: Spectrogram tracings of lines 1 and 2 shown in Fig. 4.7 with emphasis given to the K-shell absorption features in line 1 (with line 2 shown for comparison). Clusters of lines are labeled according to their respective ion species. Vertical axis is in arbitrary units. (Osborne 2011)

A full listing of all resonant Mg and Al emission lines and prominent W lines are given in Table 4.2 and Al absorption lines in Table 4.3, along with estimates for the expected electron temperature for which they’re generally observed in z-pinch plasma on Zebra. The $3d \rightarrow 5l$ M-shell W lines from the same tracing are shown in greater detail in Fig. 4.9, where the prominent Ge- to Ni-like lines clearly indicate a high temperature tungsten plasma.

Additional shots with slightly varying load configurations were also performed in an effort to create more highly resolved and intense Al K-shell absorption features. All load variations were SPWA arrangements with 0.7 μm inter-wire gaps, but the placing of the Al wire within the array was altered in each shot. Experiments were carried out both with the LCM and without. One alteration, which was named an “edge” shot, placed a comparatively heavier Al wire 2.1 μm from the end of the W array instead of the original 0.7 μm . Another,

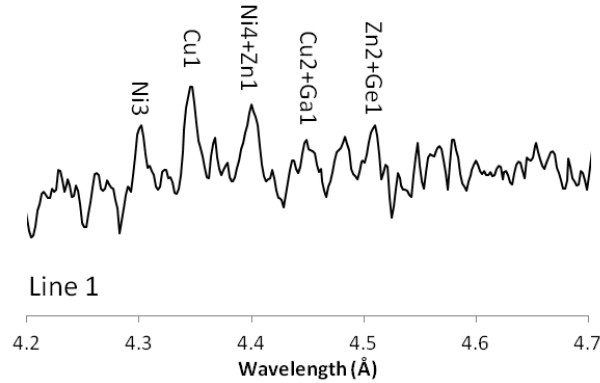


Figure 4.9: Spectrogram tracing of $3d \rightarrow 5l$ M-shell W lines labeled in accordance with (Osborne 2010) from the first line indicated in Fig. 4.4. Vertical axis is in arbitrary units. (Osborne 2011)

Shot	Type	Bolo (kJ)	Peak Current (MA)	Al/W Mass Percent	Absorption Lines?
1297	End	22.8	1.15	4.47%	Yes
2453	End	14.3	0.91	39.8%	Yes
2572	End	24.9	0.98	39.8%	No
2573	Wing	28.2	0.88	39.8%	No
2574	Edge	28.2	0.95	39.8%	No
2608	End	-	1.37	45.5%	No
2609	Wing	25.8	1.34	45.5%	Yes
2610	Edge	-	1.46	45.5%	Yes

Table 4.4: List of Zebra shots performed with the intension of creating K-shell Al absorption features. Shot configurations are given along with bolometer energy readings, the peak current through the load, the percentage of Al to W mass in the initial wire array, and whether or not the experiment produced absorption lines. Entries with '-' marks indicate data that was unobtainable for that particular experiment.

dubbed a “wing” shot, again used a heavier Al wire and placed it 2 wires from the end, creating an array that consisted of 9 W wires, an Al wire, and then 2 more W wires. The original load type was named an “end” shot to delineate it from the modified configurations.

Of all the attempted shots, absorption features were only observed in a limited number. Absorption spectra were observed in at least one of each of the three tested configurations, with the “wing” shot having the least intense absorption lines between them. Nearly all shots that were performed without the LCM did not show noticeable absorption features, with the exception of shot #2453. Table 4.4 shows a list of all shots that attempted to generate absorption features, including the load type, maximum current and energy readings, and the percentage of the load mass that was composed of aluminum. One important thing

to note from the data presented in the table is that the original shot, which had the most intense absorption lines of all experiments listed, had the smallest percentage of Al material in comparison to the total load mass.

Results from each of the modified configuration shots that produced absorption lines are shown in Figs. 4.10 and 4.12 for the edge and wing shots, respectively, along with accompanying WADM calculations (which are continued in Figs. 4.11 and 4.13). Visual comparison of the TIXRS films from these two experiments to those from the original two shots (Fig. 4.4) shows an obvious decrease in intensity of the alternate configurations. Since changes in geometry using heavy Al wires did not produce expected results, further experimentation will be required in the future to test the dependency of the intensity of absorption features against Al/W mass ratios for each load type.

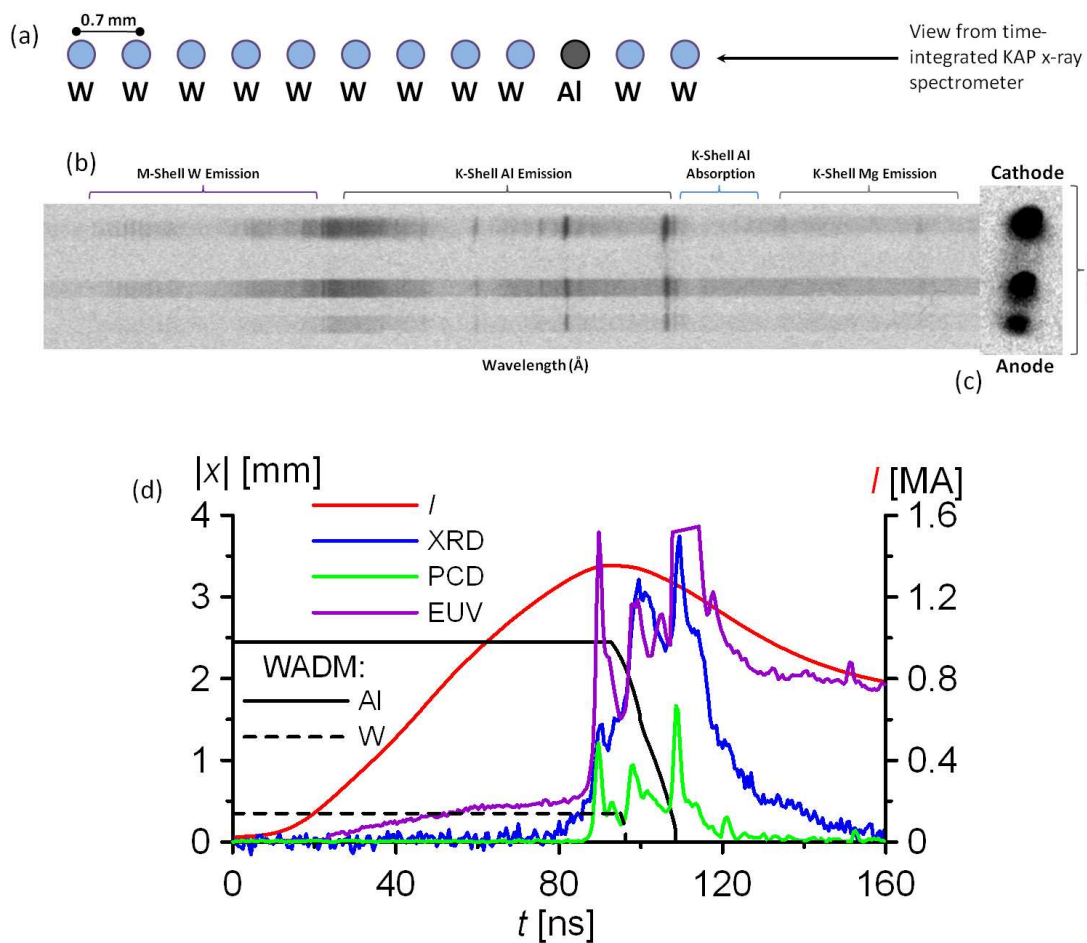


Figure 4.10: Configuration (a) and film scans (b) of experimental results from shot #2609, with time-integrated spectrometer data on the left. A pinhole image (with cutoff wavelength $< 2.7 \text{ \AA}$) is shown to the right of the spectrometer film and is labeled (c). Wire Ablation Dynamics Modeling is shown in (d). Experimental signals (XRD, PCD, and Current, as labeled) in (d) use arbitrary units, the estimated absolute value of the maximum distance where wire mass of each material is relative to the center of the array is given on the left axis, and the current scale is shown to the right. The horizontal axis scales the time evolution of the shot from the beginning of the current rise.

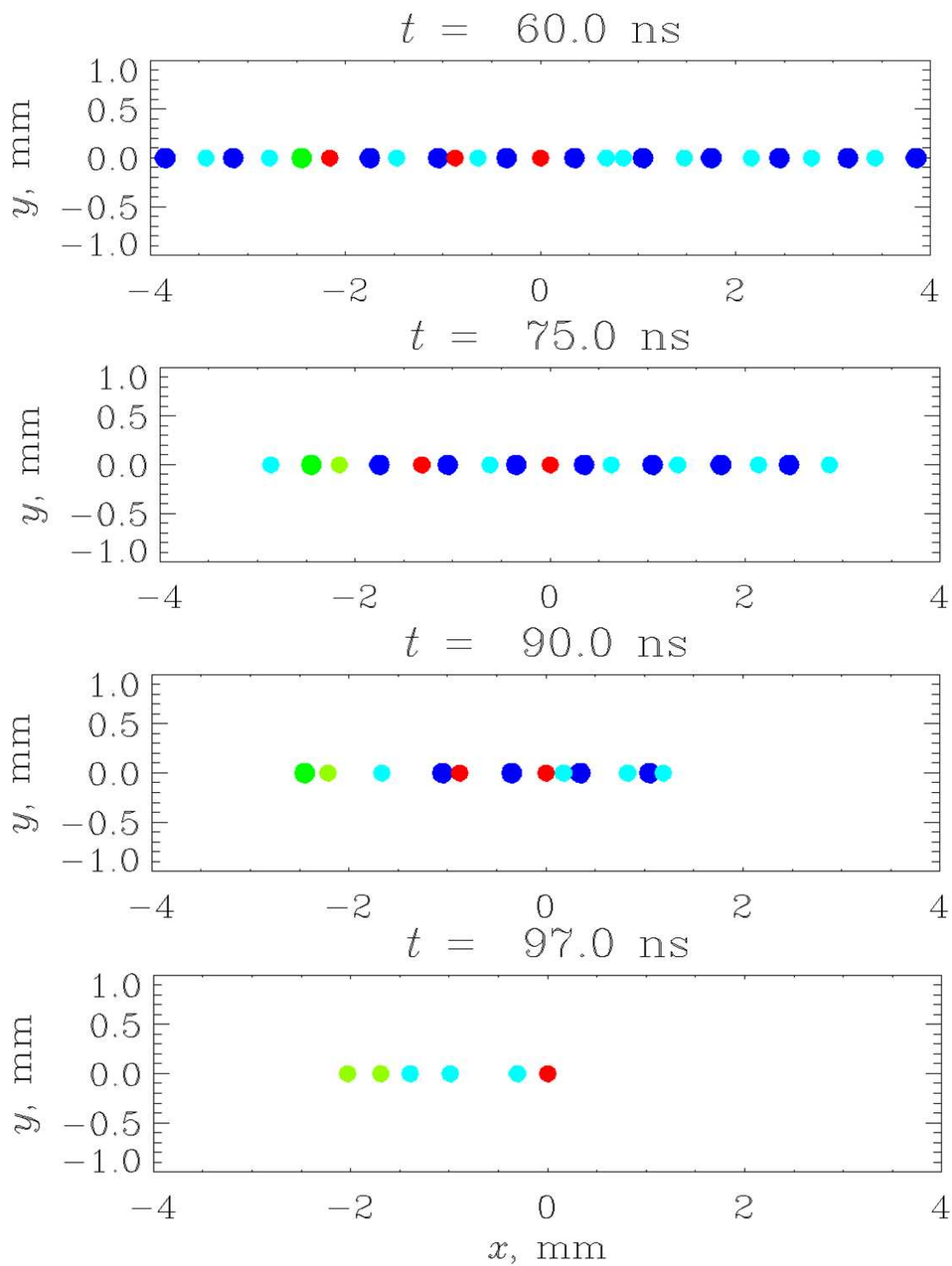


Figure 4.11: A graphical representation showing the motion of plasma from each individual wire from shot #2609, calculated using Wire Ablation Dynamics Modeling.

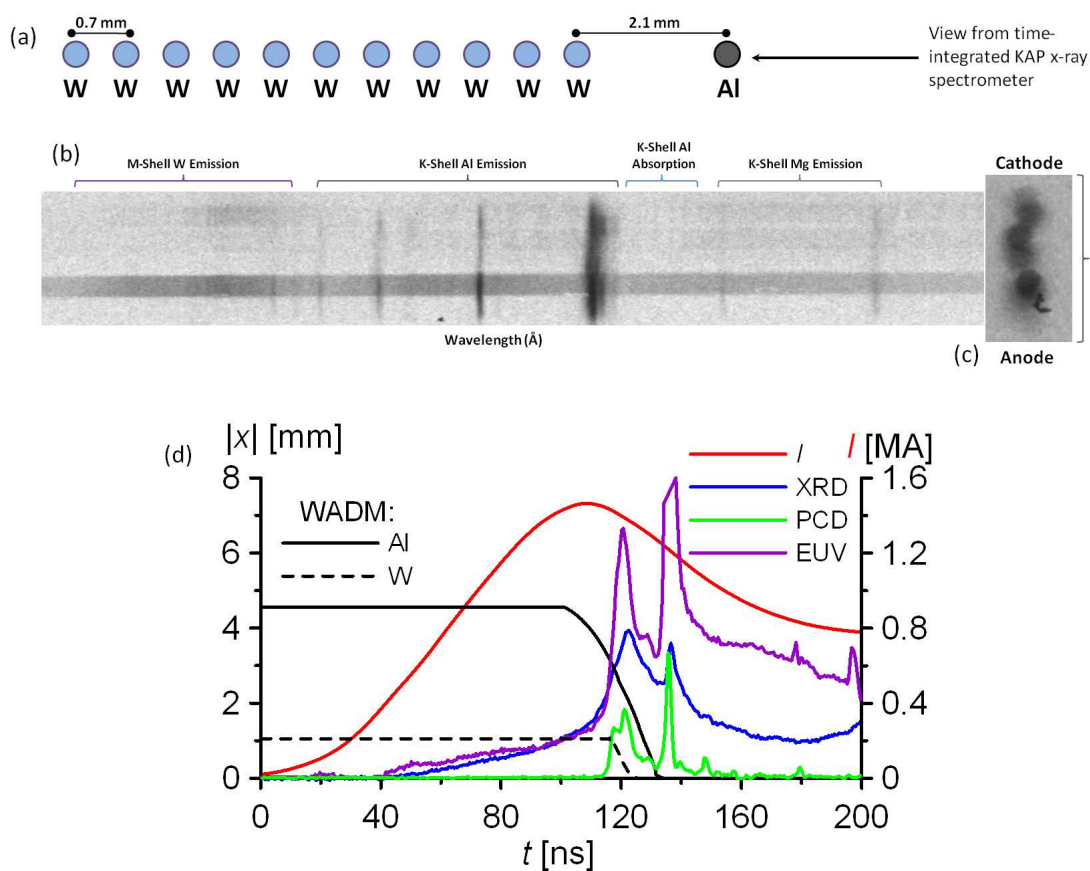


Figure 4.12: Configuration (a) and film scans (b) of experimental results from shot #2610, with time-integrated spectrometer data on the left. A pinhole image (with cutoff wavelength $< 2.7 \text{ \AA}$) is shown to the right of the spectrometer film and is labeled (c). Wire Ablation Dynamics Modeling is shown in (d). Experimental signals (XRD, PCD, and Current, as labeled) in (d) use arbitrary units, the estimated absolute value of the maximum distance where wire mass of each material is relative to the center of the array is given on the left axis, and the current scale is shown to the right. The horizontal axis scales the time evolution of the shot from the beginning of the current rise.

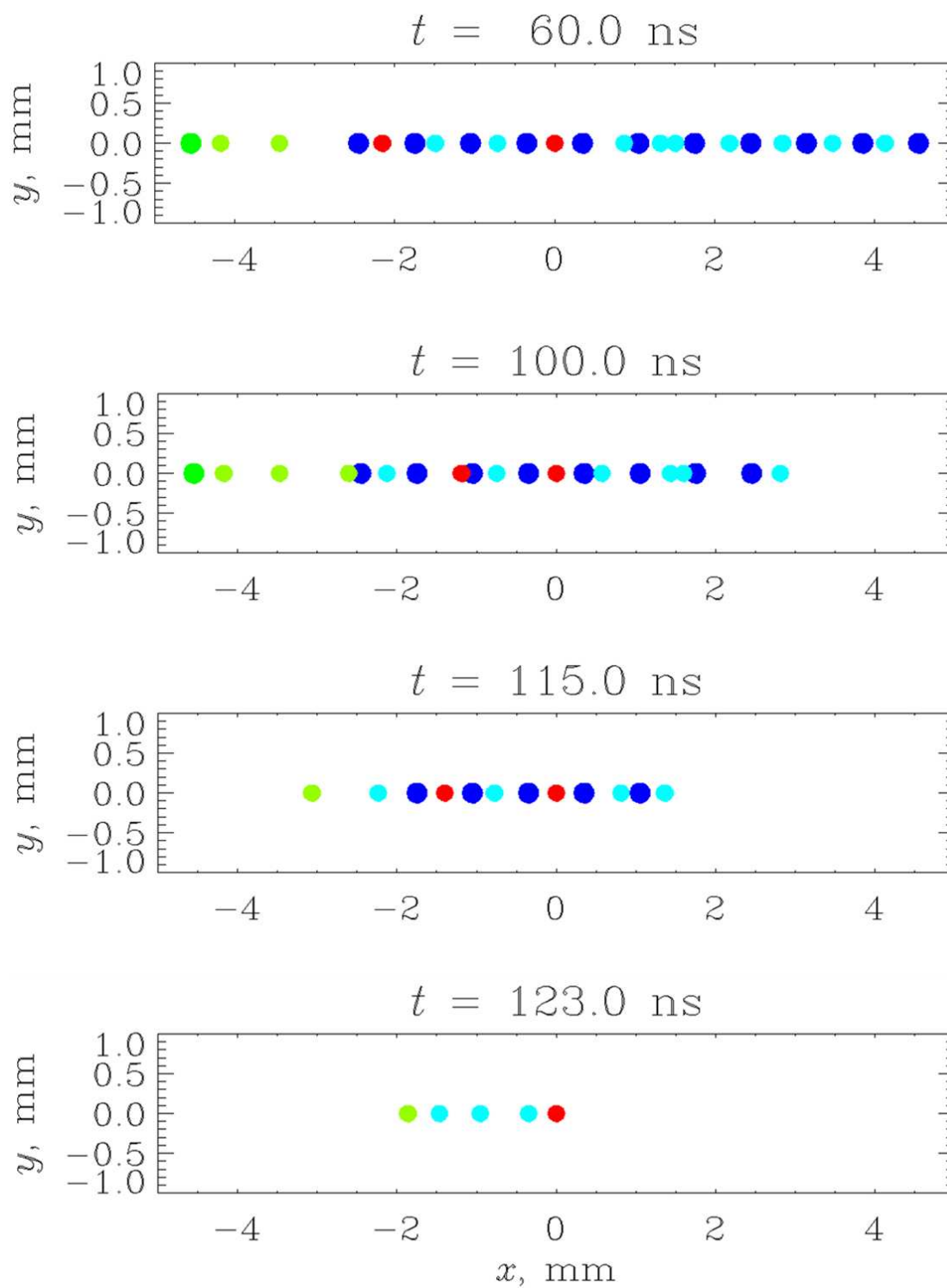


Figure 4.13: A graphical representation showing the motion of plasma from each individual wire from shot #2610, calculated using Wire Ablation Dynamics Modeling.

Part III

The Z-Pinch Ablation “Bubbling”

Phenomenon

Observed in this research is an effect in which incoming ablated plasma from outer wires of an array is hindered from converging on axis, as would normally occur due to Lorentz forces, due to interactions with plasma expanding out from the central wire of a different material (for detailed information regarding the z-pinch lifecycle, see section IV). The term “bubbling” arose from the appearance of bubble-shaped instabilities at the interaction points of these two plasmas. This phenomenon was first witnessed in SPWA loads where a 10 μm W wire was placed central to an array of widely spaced (2 mm) Al(5056) wires with thickness 28 μm . The wire diameters were chosen such that they would have similar linear mass, which combined made the array 82 $\mu\text{g}/\text{cm}$. Shadowgraphy and TIPH images for this shot are shown in Fig. 4.14(a), and the timings for all shadowgraphs are given in Fig. 4.16. The bubbling that occurs around the central W wire is shown clearly in contrast to the comparatively much more stable and uniform Al ablation plasma on either side. An ICCD camera image is also shown in Fig. 4.14(a) and gives evidence of the aluminum wires ablating much earlier than the tungsten. The inverse case where the Al wire is placed on the center and is surrounded by tungsten wires is shown in Fig. 4.14(b) for comparison; it shows “standard” plasma column formation on its central axis where the Al wire resides. Comparing the two TIPH images reveals that the amount of x-ray output with energy > 4 keV is substantially less in the case of the shot where bubbling occurred than when it did not. Additionally, the comparison of XRD signals shown in Fig. 4.16 (with significant values tabulated in Table 4.5) show that while both the original bubbling load and its inverse case

Shot	Configuration	K-shell			Zone 1 Time (ns)	Zone 2 Time(ns)	Current Rise to X- Ray Peak (ns)	Pre-pulse Percentage
		Al/Mg Te (eV)	K-shell Ne (cm ⁻³)	Al/Mg M-shell W <Z>				
1931	● ● ● ● ●	300	1.5×10^{20}	44.4	47	12	87	25%
1955	● ● ● ● ●	375	6×10^{19}	44.3	20	7	93	25%
1765	● ● ● ● ●	420	1.5×10^{20}	44.5	22	-	77	-
2456	● ● ● ● ●	370	2×10^{20}	44.2	29	11	116	25%
1037	■ ■ ■ ■ ■	-	-	-	26	15	87	17%
2301	■ ■ ■ ■ ■	-	-	44.3	44	26	63	30%
2161	● ● ● ● ●	390	1×10^{20}	44.4	23	-	78	-
2162	● ● ● ● ●	355	1.5×10^{20}	-	53	7	87	14%
1961	■ ■ ■ ■ ■	-	-	44.7	22	16	105	31%

Table 4.5: Comparison of parameters of W and W/Al shots. Single planar configurations are denoted using dots that represent single wires and multi planar arrays are shown using bars that indicate wire rows. Black indicates Al wires, gray indicates W, and light gray indicates Au. Implosion time measured from current start to PCD x-ray peak. The section of time between the start of the of x-ray output on the XRD signal and the implosion peak is given as Zone 1, and the section between the pre-pulse peak and the implosion peak is given as Zone 2. Pre-pulse percentage is calculated as the integral of the XRD signal from time $t = 0$ to the minimum point between the pre-pulse peak and the implosion peak divided by the integral of the entire signal.

implode at nearly the same time, each with gradually increasing x-ray output of nearly the same duration (approximately 20 ns), only the bubbling load forms a pre-pulse. It should also be noted that the bubbles observed are relatively stable for a period of time, as shown in Fig. 4.15, where Fig. 4.15(b) takes place approximately 6 ns after Fig. 4.15(a). Comparing these two images shows that there is little discrepancy between the two images taken at the two different times.

One of the earlier hypotheses about the cause of the bubbling instabilities was that they were due to the method in which the tungsten wires are manufactured, which leaves a thin coating of hydrocarbons on the wire that could be blown off during the current rise and cause destabilization of the imploding plasma. Tungsten wires also tend to be less uniform than thin wires of other materials, so it was postulated that the wire shapes could possibly seed instabilities, despite recent publications to the contrary (Chittenden 2008). To test both of these postulates, a load was developed that replaced the central tungsten wire with gold, which is more uniform and lacks any hydrocarbon coating. The results of this experiment are shown in Fig. 4.14(c). Evidence of bubbling in this shot shows that neither of tungsten's manufacturing imperfections are the cause, and it is more likely due to the differences in radiative properties of high-Z and low-Z elements.

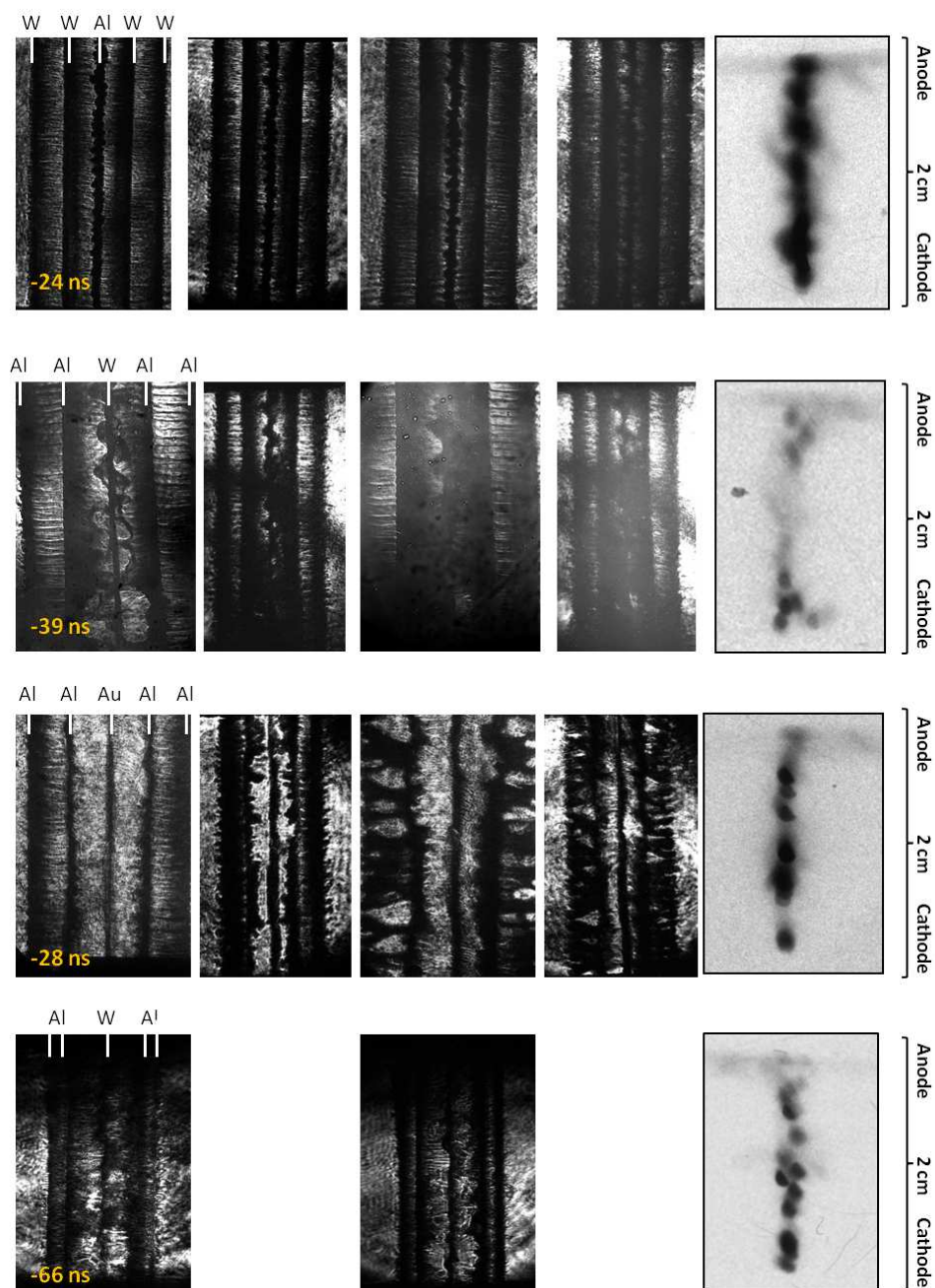


Figure 4.14: Shadowgraphy (shown at the left four positions of each row of images, viewed parallel to the laser probe with the exception of the first row, which is at a 12.5° angle) and pinhole imaging (resolution of $220 \mu\text{m}$ and lower cutoff wavelength $\lambda_{1/10} < 3.1 \text{ \AA}$, viewed at a 45° angle, shown to the right of the shadowgraphy image) for shots (top row) 1765 – SPWA with wires spaced 2 mm apart, taken 24 ns before stagnation, (second row) 1955 – SPWA with wires spaced 2 mm apart, taken 39 ns before stagnation, (third row) 2162 – SPWA with wires spaced 2 mm apart, taken 28 ns before stagnation, and (fourth row) 2161 – SPWA with Al wires spaced 1.4 mm apart and 2.8 mm from the central W wire, taken 66 ns before stagnation.

Slight variations in load geometry were also investigated in an attempt to better understand the mechanics behind the bubbling phenomenon. First, it was postulated that if the effect was caused by a pinching of the magnetic field around the tungsten wire, it could be significantly mitigated by reducing the inter-wire gap of the entire load, and indeed, the results of these experiments showed no noticeable evidence of bubbling. Furthermore, investigation of the radiation output indicates a lack of pre-pulse x-ray radiation output commonly associated with bubbling, however this hypothesis was later proven incorrect by modeling (see section 4.5). Second, the converse case was considered, where the aluminum wires were moved

a greater distance from the central tungsten wire, such that the gap between Al and W was 2.8 mm and the distance between the Al wires was 1.4mm. This was done to investigate whether or not the instabilities would be localized around the tungsten wire, however the shadowgraph displayed in Fig. 4.14(d) shows clearly that this is not the case, and the bubbling spans the entire 2.8 mm gap between the W and Al wires. Comparison of the signal data shown in Fig. 4.16(c) displays a much earlier (by approximately 9 ns) and more pronounced pre-pulse peak than the original bubbling load, as well. This ability to adjust the time of the pre-pulse with minor changes to load geometry is one of the reasons these shots could be of particular interest in the development of Z-pinch driven hohlraum configurations (Vesey 2007).

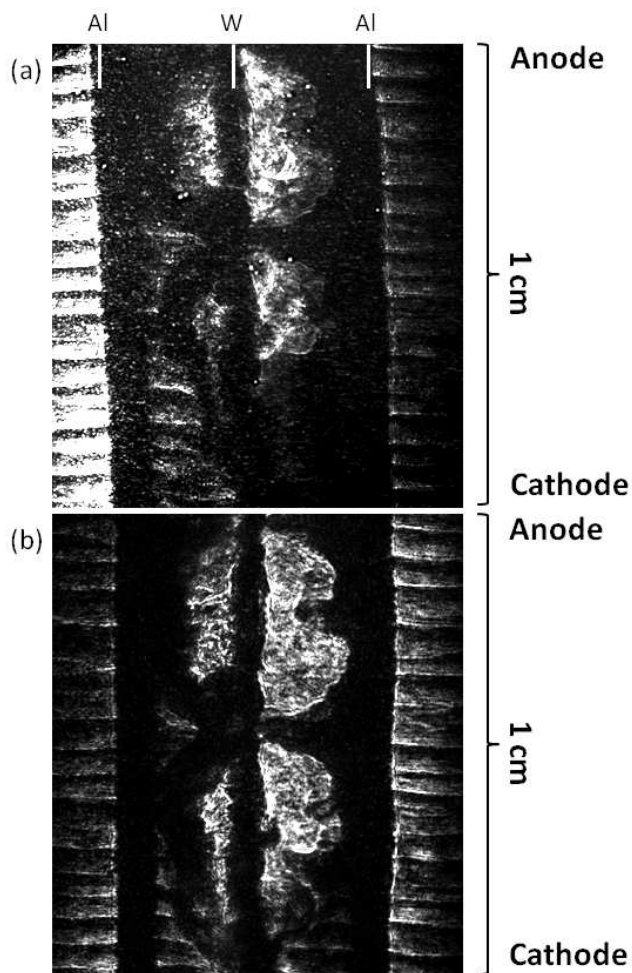


Figure 4.15: Shadowgraphy images of bubbling shot showing time evolution of instabilities over an approximately 6 ns time frame, cropped for emphasis on the center of the array.

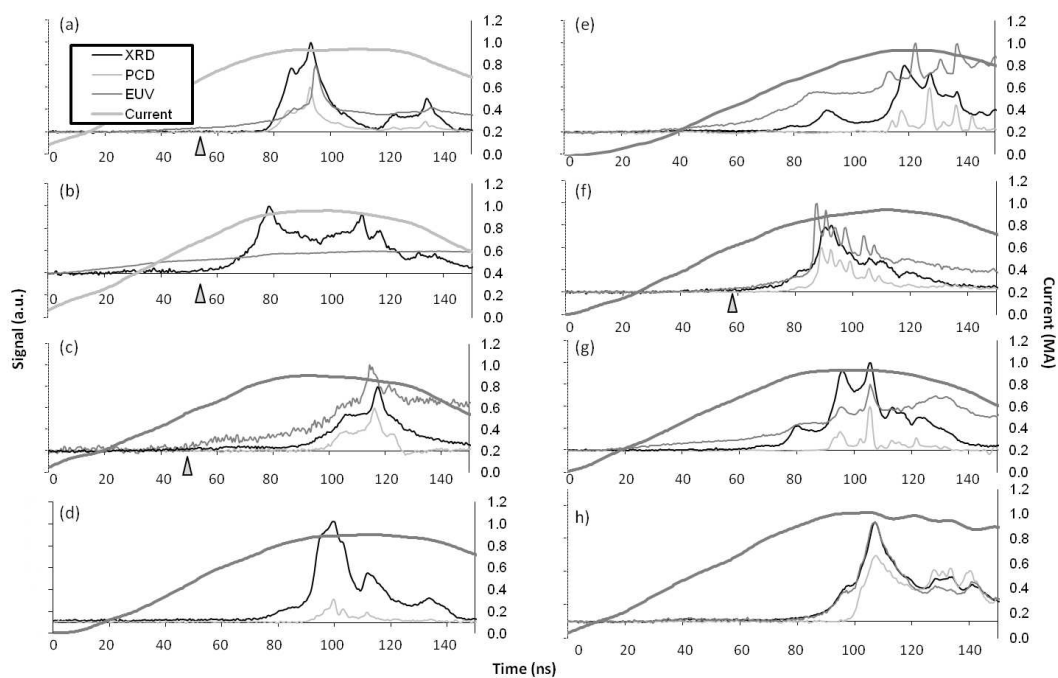


Figure 4.16: Signals for shots a) 1955 – Al/W/Al SPWA, 2 mm inter-wire gap, b) 1765 – W/Al/W SPWA, 2 mm inter-wire gap, c) 2456 – Al/W/Al SPWA, 1.4/2.8/1.4 mm inter-wire gap, and d) 2162 – Al/Au/Al SPWA, 2 mm inter-wire gap. Arrows indicate timing of shadowgraphy images shown in Fig. 4.14.

4.4 Spectroscopic Analysis of “Bubbling” Shots

Analysis of time-integrated, spatially resolved spectral data was performed in an attempt to make comparisons between plasma parameters of bubbling shots of various configurations and non-bubbling shots. Spectral tracings were taken at axial positions where the plasma column was radiating most brightly, as these areas are not only the most feature-rich, but also because these bright spots are formed early in the plasma’s lifecycle, during the ablation phase, and so plasma parameters extracted at those locations from the time-integrated spectra tend to correlate closely with data taken at pre-stagnation times (Ouart 2010). All aluminum used in this research was the alloy Al(5056), which contains 95% Al and 5% Mg, so spectroscopic modeling was done for both K-shell Al and Mg, as well as M-shell W, to estimate the density and temperature of the Al plasma and the charge balance of the W ions, respectively. The K-shell Al and Mg data was generated using a model developed at UNR. In most cases, the Al lines could be modeled and parameters extracted from them directly, however in optically thick cases, film saturation of the most intense Al lines often occurs. In the converse case (more optically thin plasma), K-shell Mg lines are barely observed at all, which makes it a simple matter to determine which model should be applied. A more detailed discussion of this method is available in (Osborne 2008). The Hebrew University Lawrence Livermore Atomic Code (HULLAC) was used to calculate charge balancing and average atomic number $\langle Z \rangle$ of the W lines (Safronova 2000). All spectra were calibrated against prominent and well known Al He and H-like (particularly He- α , He- β , He- γ , Ly- α) and W Ni-like lines.

Modeling for the K-shell Al or K-shell Mg lines for each shot (see Table 4.5) do not show any obvious gradients in density, but do indicate significantly lower temperatures for K-shell plasma in the shots with bubbling compared to without. Examples of this modeling are provided in Figs. 4.17, 4.18, and 4.19, where the optically thin K-shell Mg lines for shot #1955 were modeled in Fig. 4.18 and optically thin K-shell Al lines of shot #1765 were modeled in Fig. 4.17. Of particular note are the calculations from shot #2456 (modeling shown in Fig. 4.19), where the Al wires were spaced further from the central W wire than

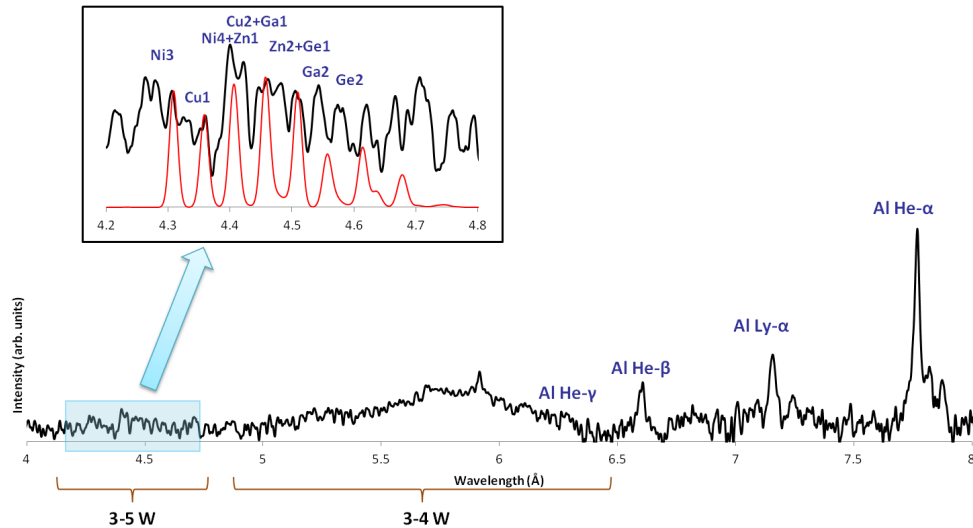


Figure 4.17: Time-integrated spectra of shot 1765 (W/Al/W non-bubbling load with 2 mm inter-wire gap), with prominent K-shell Al/Mg and M-shell W lines marked. W lines follow the identification labels used in section 3. Modeling of W $3d-5l$ transitions is shown, with model indicated in color and experiment in black.

in other experiments. While it might be expected that the wider spacing would cause a decrease in density in the Al plasma, it's actually high in comparison to other bubbling shots, which is in agreement with the shadowgraphy image shown in Fig. 4.14(d) where it appears that the ablated Al material is accumulating near the inner-most Al wire instead of passing directly into the broad gap, as would happen in a non-bubbling configuration. It is also worth noting that the change in geometry for this experiment also altered the load impedance in such a way that current distribution favored the central wire more than in other experiments, resulting in the W wire carrying higher current at an earlier time. This is the primary reason the central wire visually appears less stable than in shadowgraphy images for other shots shown in Fig. 4.14(a-c) and is also a large contributing factor to why bubbles were witnessed at such early times (66 ns before stagnation).

Charge state balancing of the W $3d-5l$ lines (which are much less optically thick than the most intense $3d-4l$ lines) show no discernible trend toward higher or lower ionization states, suggesting that the tungsten plasma undergoes no significant temperature change in shots where the instabilities occur. Examples of the W modeling are shown in Figs. 4.17, 4.18, and 4.19. The calculated $\langle Z \rangle$ for all of the SPWAs considered in Table 4.5 is 44.4

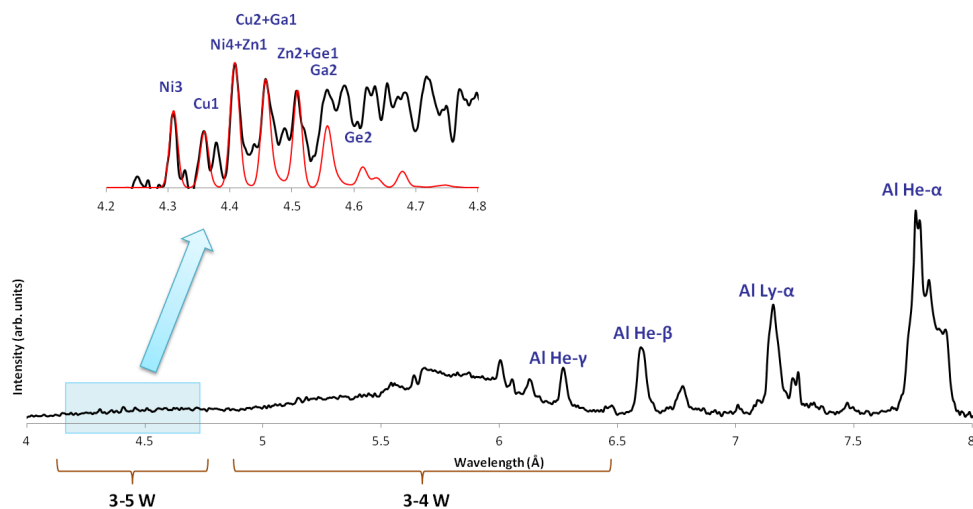


Figure 4.18: Time-integrated spectra of shot 1955 (Al/W/Al bubbling load with 2 mm inter-wire gap), with prominent K-shell Al/Mg and M-shell W lines marked. W lines follow the identification labels used in section 3. Modeling of W $3d-5l$ transitions is shown, with model indicated in color and experiment in black.

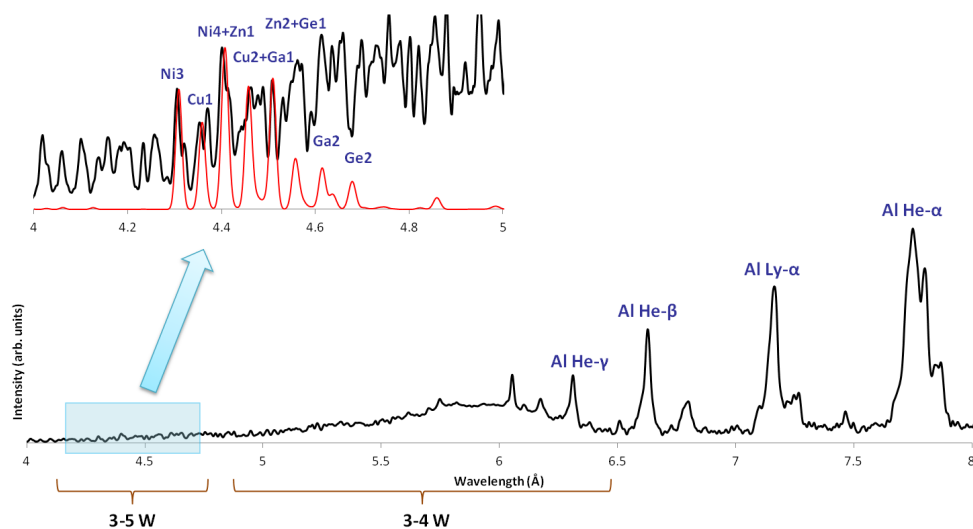


Figure 4.19: Time-integrated spectra of shot 2456 (Al/W/Al bubbling load with 1.4/2.8/1.4 mm inter-wire gaps), with prominent K-shell Al/Mg and M-shell W lines marked. W lines follow the identification labels used in section 3. Modeling of W $3d-5l$ transitions is shown, with model indicated in color and experiment in black.

± 0.3 . The benefit of modeling these lines instead of the more intense $3d-4l$ transitions is discussed in further detail in section 4.2, and lines in Figs. 4.17, 4.18, and 4.19 are labeled in accordance.

4.5 Wire Array Dynamics Modeling

In an attempt to better understand the mechanisms behind bubbling instabilities, the Wire Array Ablation Dynamics Model (WADM) (Esaulov 2008) and a radiation magnetohydrodynamic (RMHD) (Esaulov 2008, Esaulov 2009) model were employed. Previous studies of numerous planar wire array configurations (see, for example, (Esaulov 2008)) don't indicate any cause for magnetic field strengthening around the central wire regardless of its material, so focus was given instead to understanding the differences in parameters between the tungsten and aluminum plasmas. Results from the WADM for wire ablation at times corresponding to the shadowgraphy image shown in Fig. 4.14 for shot #1955 are presented in Fig. 4.20. It also shows the approximate boundaries of the bubble region around the central tungsten wire, averaged vertically, or along the array axis. In order for the ablated aluminum plasma flow to be stopped from converging on the central tungsten wire due to Lorentz forces, the following condition should be fulfilled at the boundary between the two materials:

$$\frac{\rho_{Al}v_{Al}^2}{2} + p_{Al}\frac{\gamma}{\gamma-1} = \frac{\rho_Wv_W^2}{2} + p_W\frac{\gamma}{\gamma-1} \quad (4.1)$$

Equation 1 is derived from the Bernoulli Equation for compressible flow, where the indexes Al and W correspond to the parameters of the aluminum and tungsten plasmas, respectively. Velocity of ablated plasma is denoted as v , p corresponds to pressure, ρ to flow density, and γ to the adiabatic index. Since the spatial gradients of the magnetic field at the center of single planar arrays has been shown to be negligibly small (Esaulov 2008), the magnetic pressure terms on both sides of the equation can be neglected. It can also be assumed that the velocity of incoming aluminum plasma at the interaction region in the center of the array is much larger than the radial expansion velocity of the tungsten plasma, such that $v_A \gg v_W$ (in fact, modeling predicts $v_A \approx 150 \mu\text{m/ns}$ and $v_W \approx 15 \mu\text{m/ns}$), which

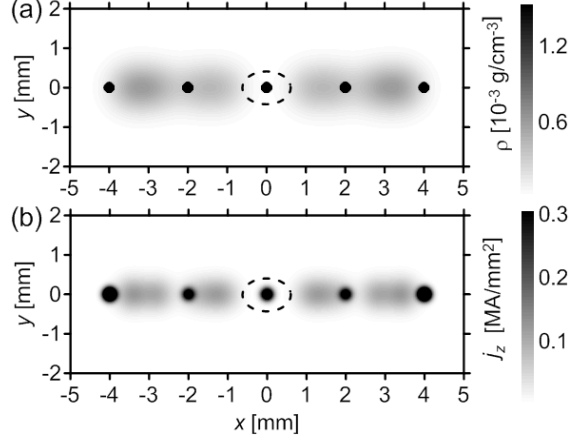


Figure 4.20: Quasi-continuous two dimensional (overhead view) distribution of the (a) plasma mass density $\rho(x,y)$ and (b) current density through the plasma $j_z(x,y)$ calculated by the WADM for Zebra shot #1955 (Al/W/Al bubbling load with 2 mm inter-wire gap) at time $t = 65$ ns, where the shadowgraphy image shown in Fig. 4.14 (second row) is taken. Dotted lines show approximate boundaries of the bubble region.

means that the first term from the right-hand side of the equation can also be neglected.

WADM calculations predict the flow density of aluminum plasma at the boundary to be $\rho_A = 3 \times 10^{-4} \text{ g/cm}^3$. The pressure of the aluminum plasma can be estimated assuming a temperature of $T_e = 20 \text{ eV}$ (Esaulov 2006) as $p_A = 1.3 \times 10^8 \text{ Pa}$. The adiabatic index at this condition can be taken as $\gamma = 1.3$ (Esaulov 2006), and as a result, the second term on the left side of Eq. (1) comes out to approximately 15% of the value of the right-hand term, so its contributions are insignificant as well. The reduced formula, then, is

$$p_W \approx \frac{\gamma - 1}{\gamma} \frac{\rho_{Al} v_{Al}^2}{2} = 8 \times 10^8 \text{ Pa}. \quad (4.2)$$

Unfortunately, this equation is still unable to determine parameters of the tungsten plasma, since pressure itself is a function of plasma mass density ρ (or ion number density n_i) and temperature. To calculate the pressure of the tungsten plasma using the ion number density, if we assume that $T_i \approx T_e$, it can be written that

$$p_W = n_i(1 + \bar{Z})T_e, \quad (4.3)$$

where \bar{Z} is the mean ion charge.

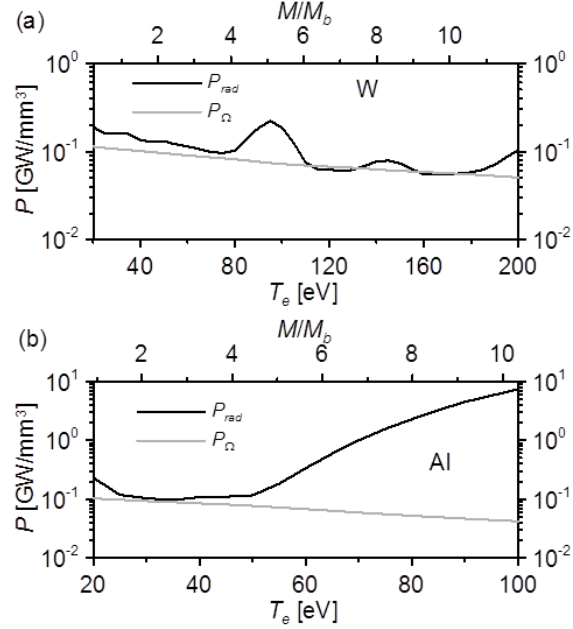


Figure 4.21: Volume densities of the radiation power losses P_{rad} and Ohmic heating P_{Ω} in (a) tungsten and (b) aluminum plasmas at constant pressure 8×10^8 Pa, as a function of electron temperature T_e or the ratio of total wire mass M to the mass of the ablated plasma M_b .

Fig. 4.21 shows the volume power density for the radiation emission P_{rad} and Ohmic heating P_{Ω} in both tungsten (a) and aluminum (b) plasmas, calculated by the RMHD model. The current through the bubbling region is calculated by the WADM to be $I_b = 60$ kA (9% of the total 670 kA being delivered to the load at time $t = 65$ ns, which corresponds to shadowgraphy imaging shown previously). Calculations from the WADM indicate that the ablated mass of the central tungsten wire at $t = 65$ ns is approximately 10% of its total starting mass, or $M / M_b \approx 10$, where M is the total wire mass and M_b is the ablated mass. This corresponds to a parameter window shown in Fig. 4.21 where Ohmic heating is fully compensating the plasma radiation and therefore fulfilling power conservation, leading to the conclusion that the instabilities observed in shadowgraphy images are likely to be formed by higher temperature ($T_e \sim 200$ eV) tungsten plasma. A higher temperature (and consequently lower density) would explain the transparency of the bubble formations to laser optical probing. The appearance of instabilities between these two plasmas can then be explained by the large differences in density and temperature.

The modeling remains consistent for the gold comparison as well, since its plasma prop-

erties and radiation features are quite similar to that of tungsten. The reason bubbling is not observed in the inverse case, where Al is central and W surrounds it, is apparent in Fig. 4.21(b) where we can see that the only parameter window for Ohmic heating compensation occurs at high ablation mass ($M / M_b \approx 2$, or 50% of the initial wire mass). This means that the Al won't be able to ablate material fast enough to create the pressures required for creating bubbles before the plasma from the outer wires has already reached axis.

Part IV

Z-Pinch Radiation Pulse Shaping with Combined Tungsten and Aluminum Planar Wire Array Loads

Planar wire arrays are currently being considered for driving hohlraum-based inertial confinement fusion experiments at Sandia National Laboratory (Jones 2010). Pre-pulses are important for driving these hohlraums (Vesey 2007), so it has become a point of interest to study the dependencies of variations in pulse shapes, particularly with regard to load configuration. These pre-pulses are generally caused by precursor plasma, which is the convergence of ablated material onto the central axis, due to Lorentz forces, during the ablation phase, which is the first stage of the z-pinch lifecycle, as shown in Fig. 4.22. Precursors for traditional single planar wire arrays can be described in three distinct stages (Bott 2006); the first stage is the formation, which is characterized by a plasma column with large diameter. In the second stage, the plasma column contracts, and during this period also radiates intensely. The column then expands throughout the third stage until the z-pinch implosion. The initial precursor column diameter is highly dependent on the plasma collisionality (Sherlock 2004). Precursor formation for planar wire arrays roughly follow the same mechanics, and a detailed discussion implosion dynamics for planar arrays can be found in (Williamson 2011).

Plasma collisionality is defined as the likelihood that the ions within the plasma will interact with one another, and is primarily dependent on their kinetic energy, $E_{ion} = \frac{1}{2}m_{ion}v_{abl}^2$. Since ablation velocity is nearly constant (Jones 2010), this means ion mass is almost solely

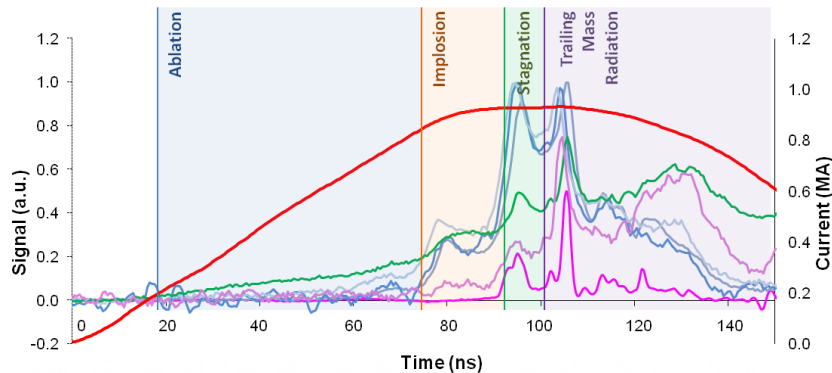


Figure 4.22: Sample shot with z-pinch lifecycle phases indicated. Signals shown are current (red), XRDs (blue), EUV (green), and PCDs (purple).

responsible for variations in collisionality. Greater kinetic energy leads to a higher mean free path, so plasmas of various materials get less collisional the more massive their ions are. For example, aluminum has a mean free path ~ 0.5 mm and tungsten has a mean free path of ~ 10 mm (Bott 2006), resulting in tungsten being much less collisional than aluminum. Highly collisional plasmas like aluminum experience a large amount of interaction on axis with flows from other ablating wires, where ions from less collisional materials like tungsten will often pass through the convergence point entirely, undisturbed; this is a major contribution factor to the differences in precursor plasma column width.

The second stage of the precursor formation, the contraction of the plasma column and subsequent radiation burst, is due to a complex process in which the column is subjected to external kinetic pressure from incoming plasma flows (Bott 2006). As more material converges and is compressed on axis by this pressure, ion density is gradually increasing as well, and both processes cause additional heating of the coronal plasma. Radiation loss rate is proportional to the square of the ion density, so as the column becomes denser, it begins to radiate more strongly and shed thermal energy. As thermal pressure is the primary force counteracting the external kinetic pressure, decreases in temperature result in more compression and a greater ion density of the precursor plasma column.

Ideally, the soft x-ray emission period for a z-pinch ICF scheme caused by a precursor will include three steps: a pre-pulse 20-25 ns before the main x-ray burst, a foot pre-pulse at

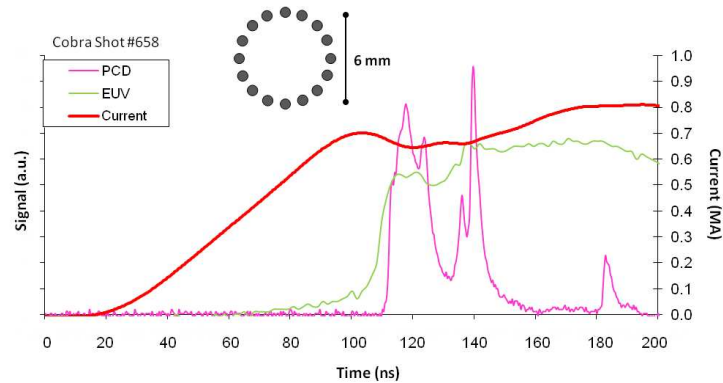


Figure 4.23: Radiation yields (PCD with 10 μm Be filter and EUV Si-Diode with 0.2 μm Al filter) of a cylindrical wire array experiment on COBRA, with current and a cartoon representation of the load configuration shown. All wires in the array were 10 μm Al (5005), an alloy consisting of 99.2% Al and 0.8% Mg.

the front of the main x-ray burst, and then the implosion peak itself. The first two steps fall within the z-pinch ablation phase during precursor formation, while the last step composes the implosion phase.

Previously, nested cylindrical wire arrays were the focus of driving core foam targets (Cuneo 2005) and have been studied extensively (Safronova 2008, Cuneo 2006, Deeney 1998) in various configurations. A typical sample of one such shot from the COBRA generator at Cornell University is shown in Fig. 4.23 for reference, where a standard “foot” pre-pulse can be seen leading into the primary x-ray burst. More recently, however, PWAs have been shown to have radiation yields that exceed those of cylindrical loads (Kantsyrev 2007) and have demonstrated near quadratic scaling factors between peak current and total power yield, where CCWAs have only shown linear scaling. These radiation yields exceed what can be accounted for through direct kinetic energy conversion E_K ($E_K < 4\text{-}6$ kJ) by a factor of 3-5 times. It is theorized that this is caused by an energy coupling mechanism due to the enhanced resistivity of the strongly inhomogeneous plasma (Chuvatin 2006). PWAs also benefit from the advantage of low opacity effects.

All multi-planar and many single-planar geometries that were tested in this survey resulted in cascade-type wire array implosions with complex multi-step precursor formation (Chuvatin 2006, Kantsyrev 2008). In the case of the multi-planar arrays, it is also of interest

that the individual planar arrays in a multi-planar load can implode independently and at different times in cases where they are not identical, such as when the arrays are composed of different materials or are of different initial wire mass. The studies presented in this section focus on the results of pulse shaping experiments performed with both pure and mixed aluminum and tungsten loads. The data presented from this research is not intended to show which loads are “best” for fulfilling precursor and pre-pulse requirements for any specific application, but simply to explain results from various loads in an attempt to better understand how pulse shapes are dependent on initial array configuration. The wire array geometries that were investigated include single, double, and triple planar loads of varying configurations. Complete tables for all shots in the survey are shown in section 9. It should be noted that all timings given throughout this section are subject to experimental error, with an estimated typical discrepancy of ± 3 ns.

5 Single Planar Bubbling Arrays

The single planar wire array offers implosion characteristics that are significantly different than the traditional cylindrical wire arrays that have been the primary focus of pulse shaping experiments in the past (Cuneo 2005). Most importantly, the amount of magnetic energy coupled to the plasma compression during the ablation and implosion phases is reduced, which causes a fundamental change in ablation dynamics and the formation of magnetically driven instabilities. Ultimately, this also causes differences in pulse shape. Due to the SPWA’s “open” configuration, it also allows for improved diagnostic viewing, whereas in CWAs, outer wire ablation often makes it difficult to see to the central axis where precursor formation is taking place. One other major difference worthy of note is that for all experiments on Zebra, the outer wires of the array received current before the inner wires, whereas in a CWA, the current is evenly distributed between the wires, since each wire is equidistant from the return current path.

The results from SPWA loads presented here are from bubbling configurations (see section III), specifically. Of these, many different configurations that generate bubbling effects

have been surveyed in an attempt to collect information on the magnitudes and timings of the x-ray radiation pulses from these implosions. This study on how bubbling effects pulse shape is then also extended to non-uniform triple planar wire array (TPWA) loads (discussed further in section 8) and non-uniform DPWA loads (discussed further in section 6). Each of these load types utilize various arrangements of W and/or Al wires only, with the exception of a single Au shot that was done for the purpose of comparison.

The SPWA bubbling load that was shown in previous sections in Fig. 4.16(a) clearly shows the formation of a strong pre-pulse that occurs 7 ns before the primary x-ray peak on both the x-ray diode and the photo-conducting detector. Comparing to the other bubbling shots surveyed (shown in Table 9.1), we can see that this configuration had the fastest total implosion time, due primarily to its relatively small size and low number of wires. The ratio of pre-pulse output to total x-ray output shown in Table 9.1 is calculated by integrating the XRD signal. First, the pre-pulse is calculated by integrating from the signal start to past the first peak and ending at the minimum point between the pre-pulse peak and the primary peak. Then an integration of the entire signal is performed and is used to calculate the ratio.

Two more SPWA configurations were also tested. The first was the same as the original bubbling load, except that the wires were each spaced 1 mm apart instead of 2 mm. This load was attempted numerous times, and in each attempt, no bubbling instabilities were witnessed on shadowgraphy and pre-pulse formation was nonexistent. In the second configuration, the Al wires were spaced further away from the central W wire. While the original uniform 2 mm gap configuration often shows pre-pulse formation near the implosion peak, it was postulated that this load with wider spacing would have a much more pronounced pre-pulse. Indeed, both XRD and PCD pre-pulses are apparent, and though they are smaller in magnitude than the shots with uniform 2 mm spacing, the pre-pulse signal on the XRD is still approximately 25% of the total integrated output.

6 Double Planar Wire Arrays

As described previously, a double planar wire array (DPWA) consists of two parallel SPWAs arranged off-axis an equal distance from the center of the chamber. As with SPWAs, the outer wires of each array receive current and begin ablating before the wires at the center of the arrays. This means that the streaming coronal plasma that forms the precursor is driven initially by the four edge wires. Because the ablated plasma from each wire does not cascade across other wires during their journey to the central axis, these loads are characterized by unique implosion dynamics. This is further complicated by the fact that the global magnetic field penetrates between the arrays at the edges, so the position of the arrays with respect to one another has a significant impact on the implosion characteristics of the load as a whole. It should also be noted that this configuration is even more beneficial to diagnostic viewing than the SPWA, as precursor formation takes place in the gap between the two arrays, where it can be easily seen. These characteristics have made DPWAs a source of extensive study on Zebra since their inception (Kantsyrev 2010).

First, two asymmetric double planar wire arrays (DPWA) were tested in which both were composed of $6\ \mu\text{m}$ W and $15\ \mu\text{m}$ Al arrays, putting the two planes at similar total linear mass. Both shots yielded similar results. While shadowgraphy, displayed for a sample of one of the shots in Fig. 6.1(c), shows some formation of instabilities similar to bubbling where the two arrays meet, the signals in Fig. 6.1(a) lack the prominent pre-pulse witnessed in other bubbling shots. A pre-pulse still exists at the foot of the primary implosion peak on the XRD signal, however one is not apparent on the PCD, suggesting that it's formed by soft radiation only, as is often common for precursors. No-

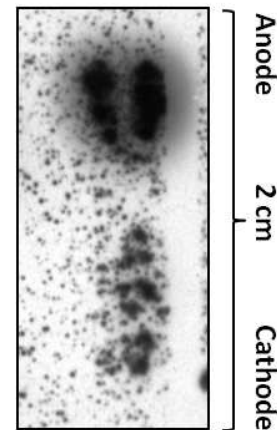


Figure 6.3: Time-gated pinhole image of shot #1965, taken ~ 30 ns before the implosion peak, filtered to show radiation energies > 1 keV.

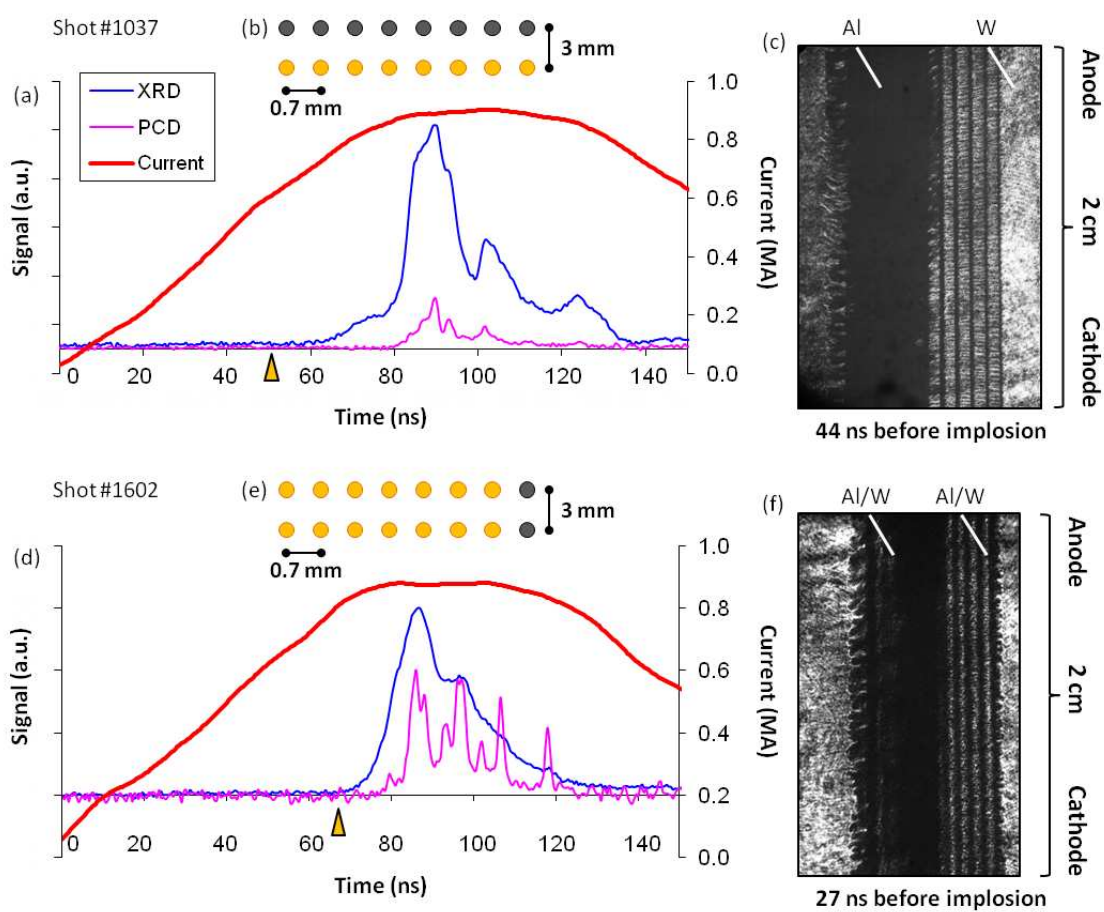


Figure 6.1: Sample shots from two of the DPWA configurations tested. Arrows on signals indicate the approximate times when the corresponding shadowgraphy images were taken. Initial positions of the arrays are indicated with white lines overlaid on shadowgraphy images, with slanted markers representing arrays that are viewed at an angle rather than parallel to the field of view.

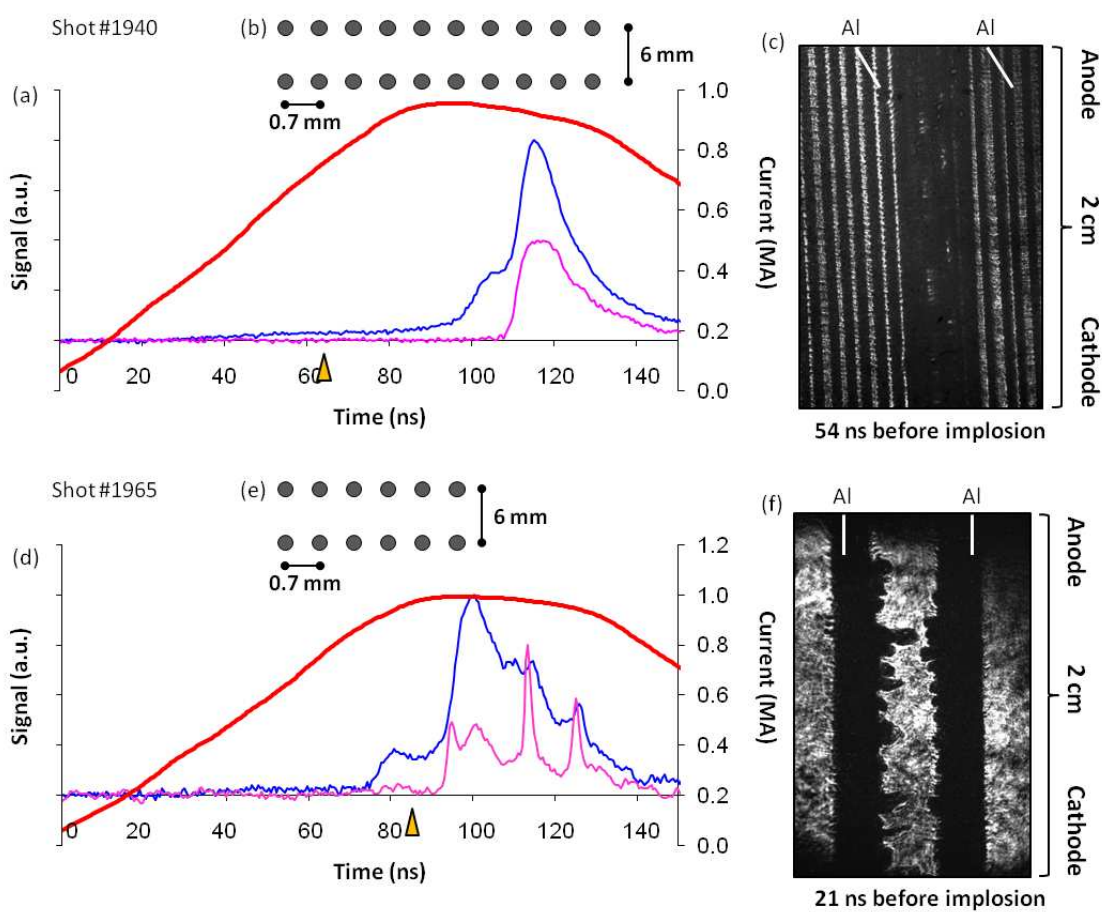


Figure 6.2: Sample shots from two of the DPWA configurations tested. Arrows on signals indicate the approximate times when the corresponding shadowgraphy images were taken. Initial positions of the arrays are indicated with white lines overlaid on shadowgraphy images, with slanted markers representing arrays that are viewed at an angle rather than parallel to the field of view.

tably, the pre-pulse to total output ratio is much lower than in other bubbling shots (17%).

A configuration in which the two end wires of a W DPWA were replaced with Al tracers was also included in the survey and is shown in Fig. 6.1(d-f). Shadowgraphy clearly shows the Al wires ablating and disintegrating first (the Al wires are located at the left sides of the arrays in the image) and a small x-ray burst prior to the implosion peak can be seen on the PCD signal. The corresponding XRD signal indicates a gradual (compared to other z-pinch shots illustrated in this section) build-up of soft radiation during this time period leading up to the peak radiation pulse. This small precursor pulse is most likely due to the formation of a coronal plasma at the center of the array composed primarily of Al material from the tracer wires, which ablate much earlier and more quickly than the W wires. It is also worth noting that this shot had the lowest total percentage of integrated precursor signal to total radiation output out of all shots surveyed in this research.

Two other less complex load configurations were tested that were similar to one another, the first being two arrays of 10 Al wires of the same linear mass, and the second exactly the same, except that each array was composed of only 6 thicker, heavier wires. Despite their similarities, the two shots showed distinctly different pre-pulse shapes, as indicated in Fig. 6.2. Shadowgraphy for the second shot, shown in Fig. 6.2(f), sheds some light as to why, namely through the observation that there is no precursor formation in the center of the array despite the fact that the image was taken during the pre-pulse. This suggests that the two arrays must have simultaneously formed precursors independent of each other, and this is further reinforced by examining the TGPH images, a sample of which is shown in Fig. 6.3 (taken 10 ns before the shadowgraphy image in Fig. 6.2(f) at the start of the pre-pulse) that clearly illustrates intense radiative output from two separate columns in the $E > 1$ keV range. This is due to the low aspect ratio, defined as the width of the array W_{array} divided by the inter-planar gap Δ , or $K = W_{array}/\Delta$, allowing the magnetic field to completely penetrate the area between the arrays. For a detailed discussion of these ablation dynamics, see (Williamson 2011).

7 Skewed Double Planar Wire Arrays

Results were recently obtained and published (Kantsyrev 2011) from a novel DPWA configuration that introduces an axial component to the magnetic field by leaning the wires in each of the rows opposite directions from their original angles along their respective planes. An optical image taken with the ICCD camera during the early stages of the ablation phase is shown in Fig. 7.2 to illustrate this new configuration, where the angle of view is perpendicular to the two planes. The purpose of testing this geometry is to explore how the precursor formation and subsequent pre-pulse radiation yield is affected by the introduction of an axial magnetic field component B_z to the $\mathbf{j} \times \mathbf{B}$ Lorentz force, which in a traditional DPWA load is dependent almost entirely on the azimuthal magnetic field B_θ . This axial component to the magnetic field generally counteracts precursor formation and array implosion because the Lorentz force component that it introduces is directed away from the center of the array toward the load periphery.

The angle of the wires in the skewed double planar wire array (Sk-DPWA) loads tested were 16° and 28° , and all loads that showed evidence of precursor formation had 6 mm gaps between wire planes, whereas a number of experiments with 3 mm gap configurations that were also tested showed little to no pre-pulse on either the XRD or PCD, despite evidence of precursor column formation. Results from sample Al and W shots with 6 mm gaps that did generate pre-pulses are shown in Fig. 7.1.

As with straight DPWA loads with low aspect ratio discussed in the previous section, the independent precursor formations occur locally for each array, however the shadowgraphy image taken at the start of the pre-pulse signal in Fig. 7.1(c) indicates that the primary source of radiation that forms the pre-pulse is emitted during the convergence of the two plasma columns into a centralized precursor. A shadowgraphy image taken at a much earlier time for a shot with the same configuration, shown in Fig. 7.3, reinforces this theory by showing a lack of centralized precursor formation prior to the pre-pulse burst measured on the XRD. The appearance of the V-shaped gap at the top of the shadowgraphy image in Fig. 7.1(c) is a result of the two precursor columns being formed at an angle relative to

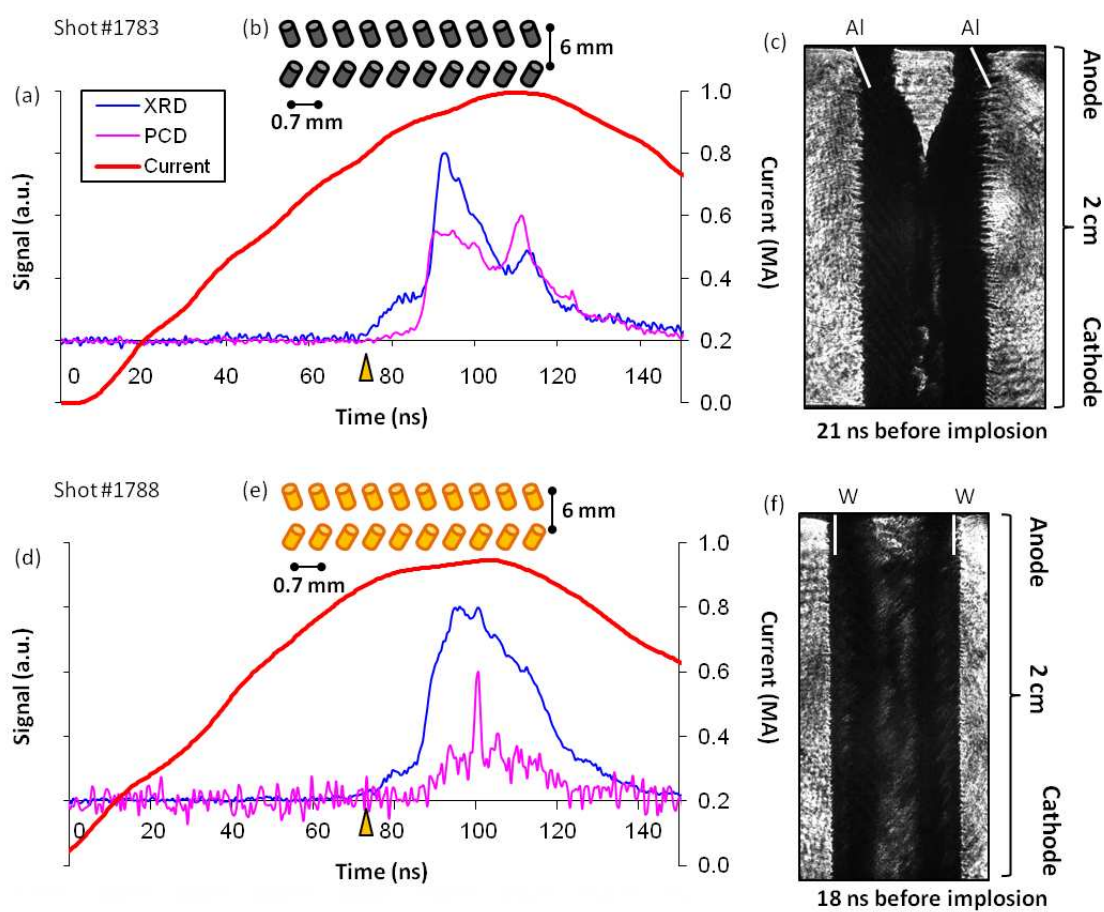


Figure 7.1: Sample shots from two of the skewed DPWA configurations tested. Arrows on signals indicate the approximate times when the corresponding shadowgraphy images were taken. Initial positions of the arrays are indicated with white lines overlaid on shadowgraphy images, with slanted markers representing arrays that are viewed at an angle rather than parallel to the field of view.

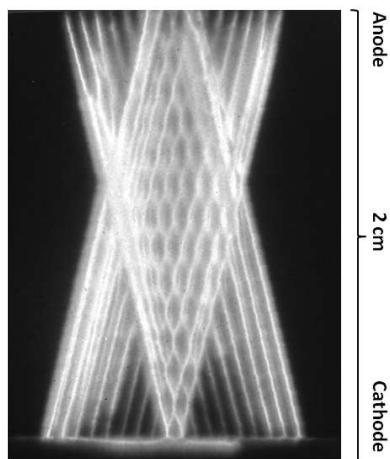


Figure 7.2: ICCD image of shot #1783, a skewed planar wire load, taken early in the implosion phase perpendicular to the planes of the array.

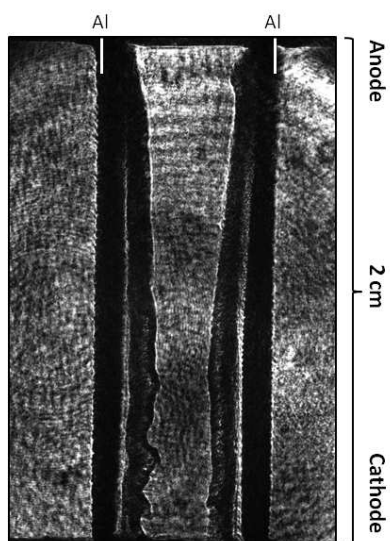


Figure 7.3: Shadowgraphy image of shot #1778, a skewed planar wire load, taken 54 ns before the implosion peak at an angle parallel to the planes of the wires.

the lean of the wire planes. It should be noted that the suppression of $m = 1$ and $m = 2$ instabilities observed in (Kantsyrev 2011) were for loads with 3 mm gaps and wide array widths, suggesting that the presence of sausage-like instabilities shown in the shadowgraphy for the two shots in Fig. 7.1 may be due to the decrease in aspect ratio.

8 Triple Planar Wire Arrays

Triple planar wire arrays, which consist of three SPWAs arranged parallel to one another, have previously been shown to have implosion dynamics similar to that of a DPWA (Kantsyrev 2008, Kantsyrev 2009). Most importantly for this pulse shaping survey is that they also undergo multi-step precursor formation. Furthermore, it was observed that TPWAs also typically form precursors in multiple off-axis locations prior to their convergence to the center of the array and subsequent implosion. Like the DPWA, the global magnetic field penetrates between the arrays at their edges, so variations in their configurations and positions relative to each other can significantly alter the load's implosion characteristics. These traits make TPWAs particularly interesting for applications in pulse shaping, so a large variety of different configurations were included in this survey.

Samples of each TPWA configuration that were tested are shown in Figs. 8.1, 8.2, and 8.3. The first of these shots, #1617, is analogous to shot #1765 from the SPWA bubbling loads and is composed of two outer W arrays with wire diameter $5\ \mu\text{m}$, while the central array is $12.7\ \mu\text{m}$ Al wires. These wire diameters were chosen to equalize the linear mass of the two arrays (each Al wire is $3.42\ \mu\text{g}/\text{cm}$ and each W wire is $3.79\ \mu\text{g}/\text{cm}$). The purpose of this configuration was to take advantage of the generally slower ablation rate of the W wires and place them in the outer arrays to mitigate the speed of precursor formation enough to that the ablation plasma of the inner Al wires would converge on axis at nearly the same time. The result was a complex multi-step pulse generation of which it is difficult to differentiate at what point the precursors are radiating and when the radiation peak itself occurs. For the sake of the survey, the primary radiation peak was taken as the highest point in the XRD signal. While further investigation of this load arrangement may reveal

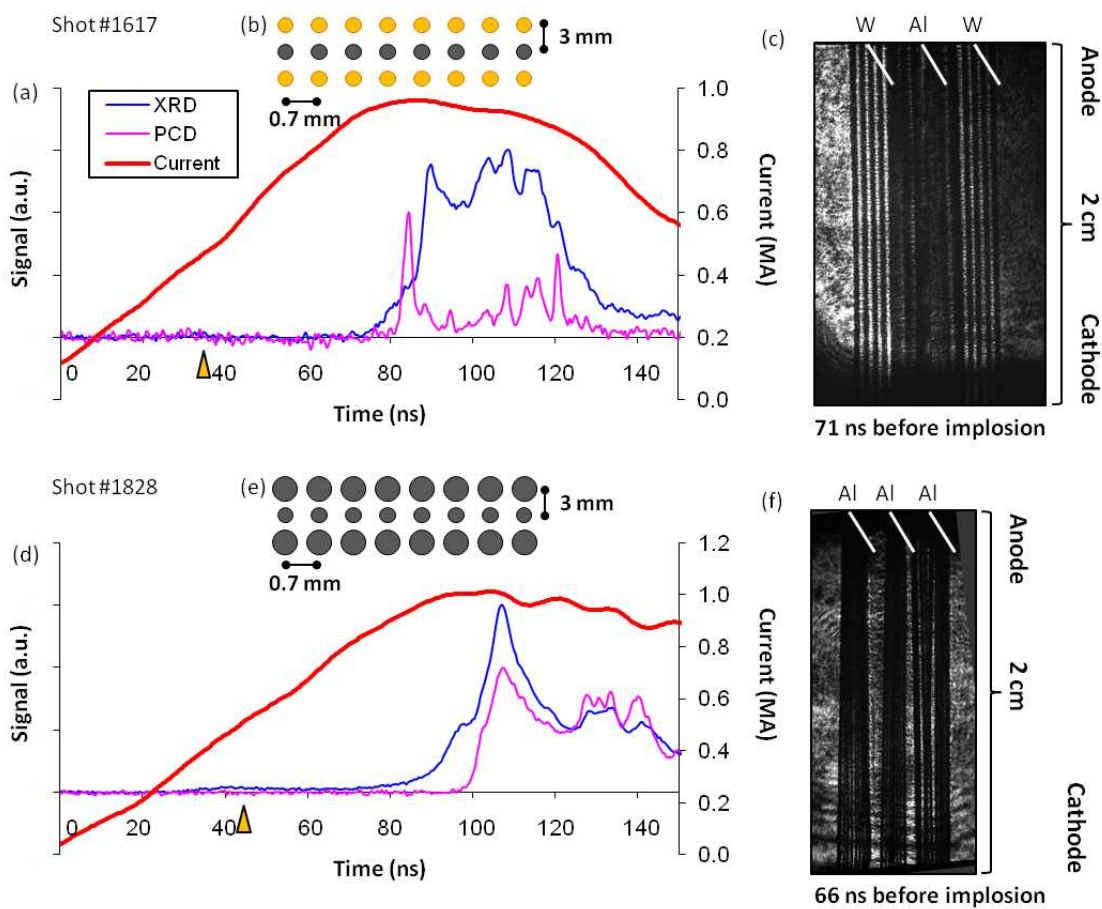


Figure 8.1: Sample shots from two of the TPWA configurations tested. Arrows on signals indicate the approximate times when the corresponding shadowgraphy images were taken. Initial positions of the arrays are indicated with white lines overlaid on shadowgraphy images, with slanted markers representing arrays that are viewed at an angle rather than parallel to the field of view.

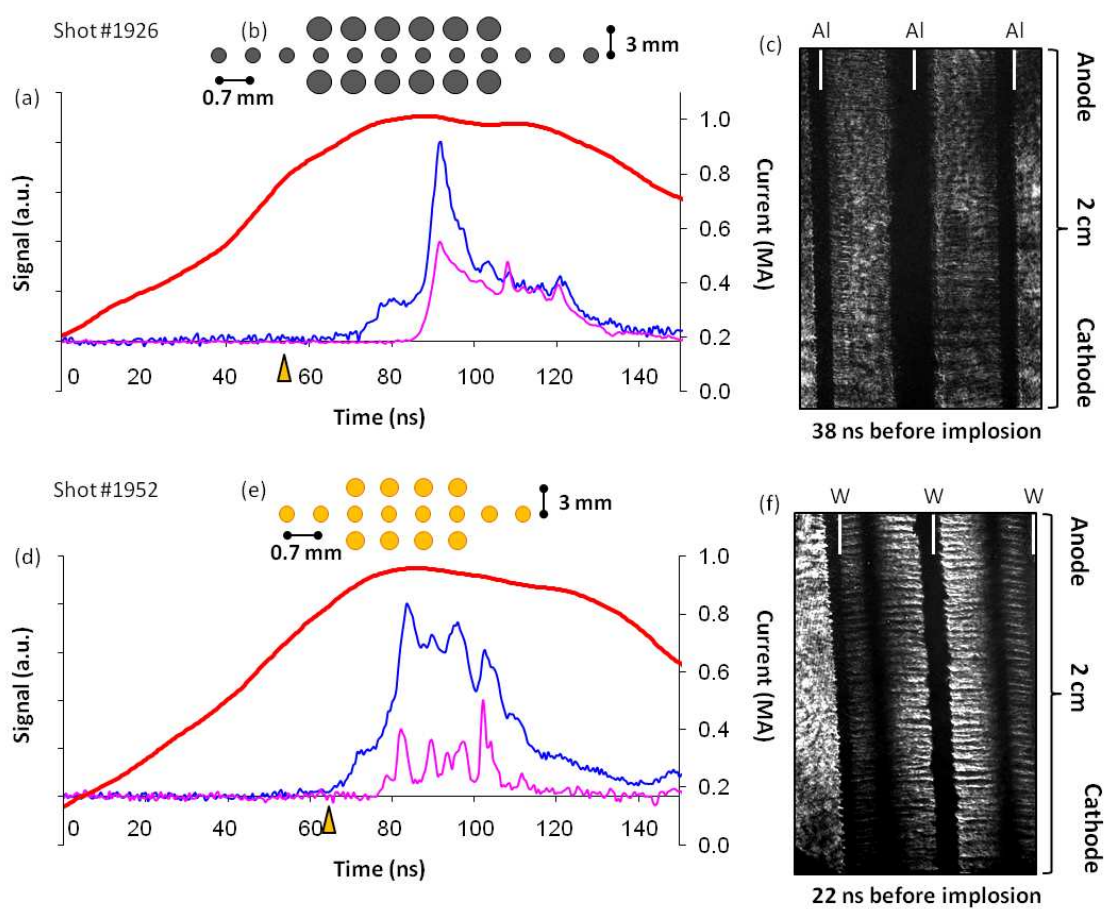


Figure 8.2: Sample shots from two of the TPWA configurations tested. Arrows on signals indicate the approximate times when the corresponding shadowgraphy images were taken. Initial positions of the arrays are indicated with white lines overlaid on shadowgraphy images, with slanted markers representing arrays that are viewed at an angle rather than parallel to the field of view.

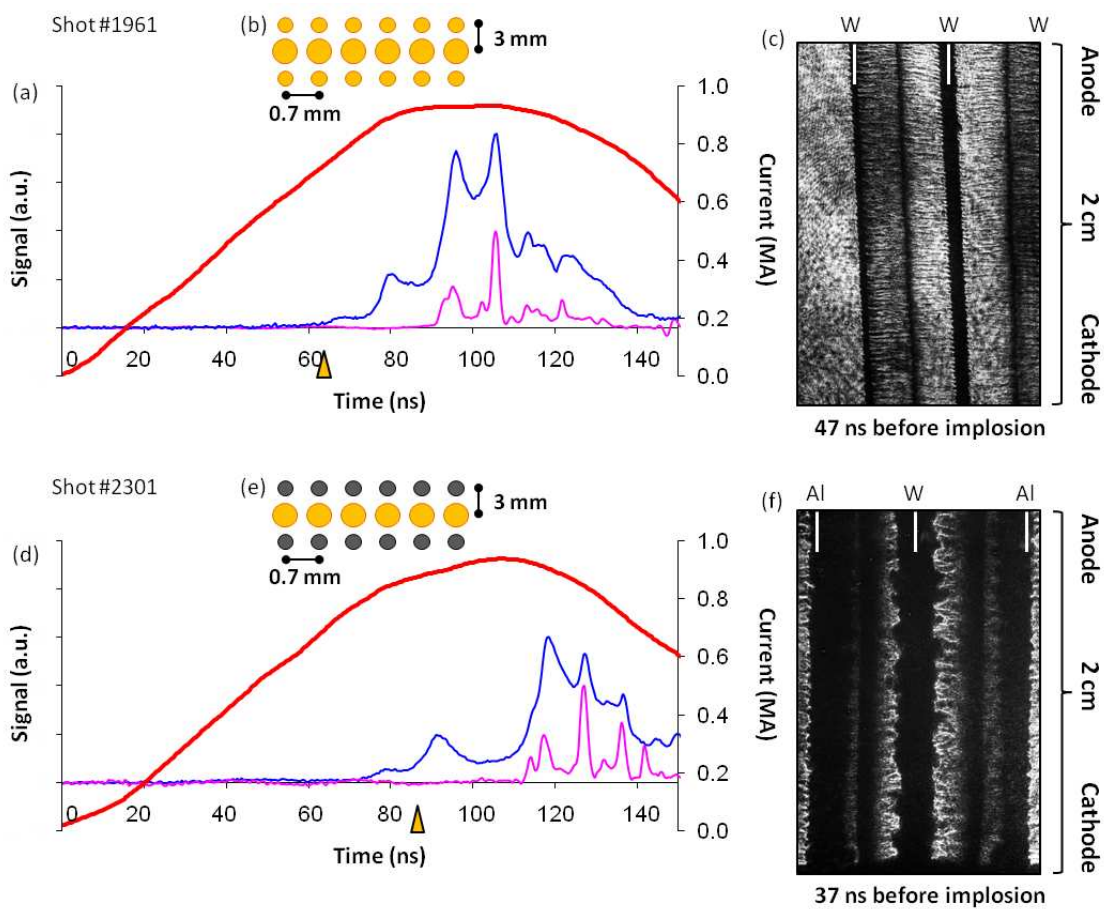


Figure 8.3: Sample shots from two of the TPWA configurations tested. Arrows on signals indicate the approximate times when the corresponding shadowgraphy images were taken. Initial positions of the arrays are indicated with white lines overlaid on shadowgraphy images, with slanted markers representing arrays that are viewed at an angle rather than parallel to the field of view.

more information regarding its implosion dynamics and pulse shape, the erratic nature of the radiation output made it less worthwhile to pursue than other configurations.

Next, a pure Al load is tested where the two outer arrays are composed of thicker wires and, consequently, heavier linear mass. Specifically, the outer arrays are more than twice the linear mass of the inner array (the wires in the inner array are $10\ \mu\text{m}$ or $2.12\ \mu\text{g}/\text{cm}$, and the wires in the outer array are $15\ \mu\text{m}$ or $4.77\ \mu\text{g}/\text{cm}$). The purpose of this load was similar to that of the previous configuration, where heavier Al wires were used in the outer arrays to delay the load implosion until after the inner array had fully ablated and formed a highly radiative precursor column. As expected, the signals in Fig. 8.1(d) show a pronounced foot pulse leading into the primary radiation burst lasting $\sim 8\ \text{ns}$.

Following the successful generation of a foot-pulse in shot #1828 using arrays of wires with varying mass, it is reasonable to postulate that if plasma could be ablated from the inner array at earlier times, the pre-pulse foot would also occur sooner, effectively separating it further from the primary radiation peak. This was accomplished with the configuration shown in Fig. 8.2(b), where the inner array was extended well beyond the width of the two outer arrays, allowing the outer-most wires from the inner array to receive current much earlier than in TPWA loads with uniform planar widths. A similar configuration was also repeated for W, shown in Fig. 8.2(e), and signals from both shots show prominent pre-pulse formation $\sim 13\ \text{ns}$ before the radiation peak, which is $\sim 5\ \text{ns}$ earlier than the foot pulse observed in shot #1828.

The case inverse to shot #1828 was also tested in a W configuration, where the inner array was composed of the heavier wires instead of the outer array. In this particular experiment, $5\ \mu\text{m}$ wires with a linear mass of $3.79\ \mu\text{g}/\text{cm}$ were used in the outer array and $12.7\ \mu\text{m}$ wires with a linear mass of $24.45\ \mu\text{g}/\text{cm}$ made up the inner array, making the center plane ~ 6 times the mass of the two outer planes. This array was designed to generate a pronounced pre-pulse from the ablated plasma of the two smaller outer arrays prior to the later convergence of the inner array and subsequent implosion. This configuration formed a pre-pulse even earlier than shot #1926, discussed previously, at $\sim 16\ \text{ns}$ prior to the primary radiation peak. These results are shown in Fig 8.3(a).

TPWAs were also chosen to be tested in an attempt to create bubbling effects in a new configuration similar to the shot in Fig. 8.3(a) with the purpose of exaggerating the pre-pulse formation by preventing the plasma from the outer arrays from converging on axis until near stagnation time. In the TPWA bubbling shot, #2301, 12.7 μm Al and 16 μm W was used, also making the central W array heavier in total linear mass than the two outer Al arrays. This configuration is shown in Fig. 8.3(e). The shadowgraphy results in Fig. 8.3(f) clearly show bubble-like instabilities along the center array that are not apparent in the pure W load. Both shots have three pronounced XRD peaks, including a pre-pulse. Of particular note is that neither of the pre-pulses in these two shots registered on the PCD, suggesting they radiated at a much lower energy than the SPWA loads. The bubbling shot also took significantly longer (44 ns) to implode than its SPWA counterparts and had an earlier pre-pulse (26 ns prior to stagnation), yet the total integrated ratio of pre-pulse to total x-ray output was still 30%.

9 Load Type Comparisons

Table 9.1 contains a list of all shots included in the pulse shaping survey where pre-pulse formations were observed, and Table 9.2 includes all shots where pre-pulses were not observed. It is important to note while viewing these tables that all measurements shown are subject to experimental error. In particular, all timings have errors up to ± 3 ns and all pre-pulse ratio approximations typically have value discrepancies of $\pm 5\%$. It can be clearly seen from the first table that shots of the same configuration generally have similar results.

Comparing the two tables, a number of observations are worthy of note. First, W DPWA configurations with Al tracers that were significantly lighter than the W wires did not form pre-pulses of any kind. The case where the linear masses of the two wire materials were nearly equal resulted in one shot with a pre-pulse and many without, though given that the pre-pulse signal from the first shot was one of the smallest observed, this should not be surprising. None of the DPWA configurations with 3 mm inter-planar gaps (high aspect ratio) made from a single material formed pre-pulses, and of the low aspect ratio loads that

Shot #	Configuration	Material	Wire Number	Dia. (μm)	Spacing/Gap (mm)	Linear Mass ($\mu\text{g}/\text{cm}$)	Bolo (kJ)	Implosion Time (ns)	Pre-pulse Time(ns)	Pre-pulse Percentage
1931	SPWA	Al/W/Al	2/1/2	28/10	2.1	82	20.4	87	12	25%
1955	SPWA	Al/W/Al	2/1/2	28/11	2.1	82	23.4	93	7	25%
2456	SPWA	Al/W/Al	2/1/2	35/10	2.8/1.4	117	12.0	116	11	25%
2161	SPWA	Al/W/Al	2/1/2	28/10	2.1	82	31.2	78	-	-
2162	SPWA	Al/Au/Al	2/1/2	28/10	2.1	82	22.9	87	7	14%
1037	DPWA	W/Al	8/8	6/15	0.7/3	82	21.3	87	15	17%
1039	DPWA	W/Al	8/8	6/15	0.7/3	82	18.6	83	13	9%
1602	DPWA	W+Al	7+1x2	6+15	0.7/3	86	18.2	86	7	5%
1789	DPWA	Al	10/10	10	0.7/6	42	17.3	86	10	11%
1939	DPWA	Al	10/10	15	0.7/6	95	11.6	118	12	16%
1940	DPWA	Al	10/10	15	0.7/6	95	16.6	116	13	20%
1963	DPWA	Al	10/10	12.7	0.7/6	66	15.5	107	12	9%
1964	DPWA	Al	10/10	12.7	0.7/6	66	16.9	103	13	13%
1965	DPWA	Al	6/6	17.8	0.7/6	81	15.9	99	19	10%
1966	DPWA	Al	6/6	17.8	0.7/6	81	16.2	104	22	22%
1967	Sk-DPWA (28°)	Al	10/10	10	0.7/6	42	13.1	95	9	11%
1630	Sk-DPWA (16°)	Al	10/10	10	0.7/6	42	10.6	96	11	8%
1777	Sk-DPWA (28°)	Al	10/10	10	0.7/6	42	17.5	90	10	12%
1778	Sk-DPWA (28°)	Al	10/10	10	0.7/6	42	14.2	90	10	10%
1780	Sk-DPWA (28°)	Al	10/10	10	0.7/6	42	16.1	98	32	14%
1783	Sk-DPWA (28°)	Al	10/10	10	0.7/6	42	16.1	92	10	11%
1788	Sk-DPWA (28°)	W	10/10	5	0.7/6	76	29.2	96	16	6%
1617	TPWA	W/Al/W	8/8/8	5/12.7/5	0.7/3	87	17.5	108	18	-
1828	TPWA	Al	8/8/8	15/10/15	0.7/3	93	28.5	106	8	11%
1926	TPWA	Al	6/12/6	15/10/15	0.7/3	83	13.8	90	13	12%
1952	TPWA	W	4/8/4	7/5/7	0.7/3	90	28.3	84	13	6%
1961	TPWA	W	6/6/6	5/12.7/5	0.7/3	180	27.7	105	16	20%
2301	TPWA	Al/W/Al	6/6/6	12.7/16/12.7	0.7/3	274	22.0	115	28	19%
2302	TPWA	Al/W/Al	6/6/6	12.7/16/12.7	0.7/3	274	23.5	113	30	21%

Table 9.1: List of all shots in the pulse shaping survey where pre-pulse formations were observed. Graphical representations of each of the load configurations can be found in Figs. 8.1, 8.2, and 8.3. Pre-pulse percentages correspond to the ratios of integrated XRD signals that accounts for the pre-pulse formations with respect to the total XRD yield for the entire z-pinch lifecycle.

Shot #	Configuration	N	Material (alloy)	Dia. (μm)	Spacing/Gap (mm)	Total Mass ($\mu\text{g}/\text{cm}$)	Bolo max (kJ)
1765	SPWA	2/1/2	W/Al/W	10/35	2	117	30.1
1038	DPWA	8/8	W	6	0.7/3	87	22.4
1253	DPWA	8/8	W	6.00	0.7/3	87	16.1
1402	DPWA	7+1x2	W+Al	10+22.5	0.7/3	234	16.5
1404	DPWA	7+1x2	W+Al	10+22.5	0.7/3	234	-
1601	DPWA	7+1x2	W+Al	6+15	0.7/3	86	23.9
1605	DPWA	8/8	Al	17.8	0.7/3	108	13.9
1606	DPWA	8/8	Al	17.8	0.7/3	108	14.7
1613	DPWA	8/8	W	6	0.7/3	87	22.9
1614	DPWA	8/8	W	6	0.7/3	87	24.8
1634	DPWA	13+1x2	W + Al	5+12.7	0.7/6	105	16.2
1767	DPWA	8/8	Al	17.8	0.7/3	108	21.5
1972	DPWA	8/8	W	7	0.7/3	119	27.5
1598	DPWA	7+1x2	W+Al	6+15	0.7/3	86	13.4
1599	DPWA	7+1x2	W+Al	6+15	0.7/3	86	14.9
1600	DPWA	7+1x2	W+Al	6+15	0.7/3	86	0.0
1942	Skewed DPWA (28deg)	10/10	Al	10	1/6	42	12.7
1951	Skewed DPWA (28deg)	10/10	Al	10	1/6	42	12.9
1632	Skewed DPWA (16deg)	10/10	Al	10	0.7/3	42	12.0
1779	Skewed DPWA (28deg)	10/10	Al	10	0.7/3	42	18.5
1781	Skewed DPWA (28deg)	10/10	Al	10	0.7/3	42	17.0
1787	Skewed DPWA (28deg)	10/10	W	5	0.7/3	76	34.6
1259	TPWA	10/10/10	Al	10.00	0.7/3	64	9.7
1615	TPWA	8/8/8	W	5	0.7/3	91	19.7
1616	TPWA	8/8/8	W	5	0.7/3	91	21.2
1925	TPWA	7/4/7	Al	17.8/10/17.8	0.7/3	103	13.2
1949	TPWA	6/6/6	W+Al	7	0.7/1.5	134	27.4

Table 9.2: List of all shots in the pulse shaping survey where pre-pulse formations were not observed.

did, the total array mass was proportional to the percentage of pre-pulse signal to total radiation output as detected by the XRD. Sk-DPWAs only formed pre-pulses in cases with low aspect ratio. Of the TPWAs surveyed, none of the loads with uniform wire material and diameter resulted in observed pre-pulse formation. Of all the shots tested, the ones where bubbling effects were present generated the most distinct pre-pulse shapes with the highest yield percentages. Since the implosion and ablation dynamics of these loads is still not yet fully understood, it should be a point of interest to advance studies regarding the bubbling phenomenon in cases where their pulse shapes are deemed useful for practical applications.

Part V

Conclusions

This dissertation has attempted to further the development of tungsten plasma diagnostics while investigating phenomena and inertial confinement fusion (ICF) applications related to high energy density z-pinch plasmas and highlights areas in which I actively participated throughout my graduate studies. Focus was given to planar wire arrays due to their high radiation output and diagnostic accessibility, as well as recent interest in their usefulness for ICF. These studies combined both experimental and theoretical analysis, including spectral modeling and simulations, to form as comprehensive an analysis as possible. This included my personal participation in 15 experimental campaigns on the University of Nevada, Reno generator Zebra, 2 on Cornell University's COBRA machine, 1 on UNR's Leopard laser, 2 at the UNR Sparky facility, and the development of a kinetic code to generate synthetic spectra from HULLAC University Lawrence Livermore Atomic Code (HULLAC) data. I took part in the development and installation of the load current multiplier (LCM) on Zebra and attended to the operation and reconfiguration of optical and shadowgraphy systems for all campaigns, many of the images from which are included in previous sections. As my time on Zebra progressed, I gradually took on more responsibilities for the day to day operation of our experimental group, including the fielding of the time-gated extreme ultraviolet (TGEUV) spectrometer and data processing (this included the development of new signal processing techniques), to name only a few of the more challenging tasks. Eventually I became responsible for overseeing and training new graduate students and ensuring quality in the daily operation of diagnostics. This expertise was also applied to campaigns that I participated in at other facilities, as well.

The first challenge I faced in studying the tungsten and aluminum-based plasmas dis-

cussed was the development of proper tungsten plasma diagnostics, particularly spectroscopy. To aid in this endeavor, data from the Lawrence Livermore National Laboratory's (LLNL) electron beam ion trap (EBIT) was employed and has proved an invaluable resource for both benchmarking theoretical modeling and providing a basis for charge state balancing. This method of charge balancing, which is done using independently modeled synthetic spectra for each ion species, is both a useful diagnostic for z-pinch-generated W plasma research currently being conducted at (UNR) and Sandia National Laboratories (SNL) and for identifying lines in EBIT spectra itself. In particular, the relatively optically thin $3d \rightarrow 5l$ transitions continue to be the most promising candidates for charge balancing in the M-shell band of high energy density (HED) plasmas on Zebra. Many of the lines within the 5-8 Å range in z-pinch spectra were also identified with the aid of EBIT data. I developed the kinetic code front-end for generating the synthetic spectra throughout this dissertation, as detailed in previous sections, and employed charge balancing techniques and all line identifications found here.

During our work with Al tracer wires, we were then able to develop a method for generating absorption spectra using a z-pinch wire array load without the need to utilize an external source. Al absorption features were shown to occur in areas of the source where Al is cold and W SPWA plasma is radiating intensely and is hot enough to produce prominent $3d \rightarrow 5l$ features. These conditions under which absorption would be expected to occur are all shown to be met through spectroscopic analysis. Estimates of electron temperature in the outer Al plasma using charge-state balancing and comparisons with previous NTF publications suggest values between 10-40 eV (Ivanov 2011). All load variations shown beyond the first, original experiment, were designed either completely or in part by myself, personally.

I also designed all bubbling effect loads used presented here, based on reasonable theories that I either concluded myself or discussed with other members of our team or the community at large. The combined W/Al planar array loads that generated bubble-shaped instabilities in loads where a high-Z element, specifically W or Au, is surrounded by Al wires were a result an investigation that I carried out, myself. A full analysis of these shots, including shadowgraphy, x-ray signals, and spectroscopy has been presented and discussed.

The possibility that these effects are caused by drastic differences in the parameters and radiation features of low-Z and high-Z plasmas has been shown via modeling, while numerous other hypotheses have also been presented and proven false. The modeling provided by one of my close collaborators has shown to be consistent with experimental results in all cases, including the lack of bubble-like instabilities witnessed in inverted (Al in the center, W on the outside) configurations. More importantly, a method has been developed for identifying parameter windows where bubbling can and cannot occur, allowing future load designs to either take advantage of these instabilities or avoid them, depending on their intended application.

Following this, I then proposed a bubbling shot in a triple planar wire array (TPWA) configuration in order to study of the signal shapes of these loads with the expectation that they may be used in pulse shaping experiments in the future. I have concluded that the single planar wire arrays (SPWA) appear to implode at nearly the same times whether bubbling instabilities are formed or not, however all bubbling shots appear to have lower high energy radiation yield than other similar loads. I have also shown that the timing and shape of these pre-pulses can be altered by varying the load geometry. However, with the exception of the double planar wire array (DPWA) and Au shots, all loads consistently had a pre-pulse to total radiation output ratio of approximately 25-30%.

Finally, I have presented a survey of the radiation output from planar wire experiments with various mixtures of W and Al were shown to be effective in generating a wide variety of different pulse shapes located at different times with respect to the signal peak, with the intention of creating a compilation that will be useful for applications in inertial confinement fusion and future radiation research. I participated in the execution and data collection of every shot in this survey. Bubbling loads of various configurations were shown to be effective in consistently generating useful pre-pulse shapes. In fact, bubbling loads in triple planar configurations showed some of the earliest and most prominent precursor formations. DPWAs in both skewed and straight configurations were also shown to be effective in generating prominent pre-pulses, although only with loads of low aspect ratio or multiple wire materials. TPWAs were primarily effective in generating pre-pulses in configurations where

the geometry, materials, or masses of the arrays were varied in specific ways.

The development of tungsten plasma diagnostics is still very much in its infancy, particularly regarding spectroscopy. It is this my hope that these studies, which resulted in the publication of 27 (3 first authored and 24 co-authored) refereed articles, 11 (1 first authored) conference proceedings, and 60 (8 first authored) posters, will aid the generation of more sophisticated diagnostics for tungsten plasmas going into the future.

References

- Anderson, O.A.; Baker, W.R.; Colgate, S.A.; Ise, J.; Pyle, R. V.; Neutron Production in Linear Deuterium Pinches. *Phys. Rev.* **1958**, *110*, 1375.
- Bauer, B. S.; Kantsyrev, V. L.; Winterberg, F.; Shlyaptseva, A. S.; Mancini, R. C.; Li, H.; Oxner, A. Proceedings of the Fourth International Conference on Dense Z-pinches. *AIP Conf. Proc.* **1997**, *153*, 409.
- Beiersdorfer, P.; Osterheld, A.L.; Scofield, J.; Wargelin, B.; Marrs, R.E.; Observation of Magnetic Octupole Decay in Atomic Spectra. *Phys. Rev. Lett.* **1991**, *67*, 2272-5.
- Beiersdorfer, P.; Laboratory X-ray Astrophysics. *Annu. Rev. Astron. Astr.* **2003**, *41*, 343-390.
- Bott, S. C.; Lebedev, S. V.; Ampleford, D. J.; Bland, S. N.; Chittenden, J. P.; Ciardi, A.; Haines, M. G.; Jennings, C.; Sherlock, M.; Hall, G.; Rapley, J.; Beg, F. N.; Palmer, J. Dynamics of cylindrically converging precursor plasma flow in wire-array z-pinch experiments. *Phys. Rev. E.* **2006**, *74*, 046403.
- Burkhalter, P. G.; Dozier, C. M.; Nagel D. J.; X-ray spectra from exploded wire plasmas. *Phys. Rev. A* **1977**, *15*, 700.
- Chittenden, J.P.; Jennings, C.A.; Development of Instabilities in Wire-Array Z Pinches. *Phys. Rev. Lett.* **2008**, *101*, 055005.
- Chuvatin, A.S.; Kokshenev, V.A.; Aranchuk, L.E.; Huet, D.; Kurmaev, N.E.; Fursov, F.I.; An inductive scheme of power conditioning at mega-Ampere currents. *Laser and Particle Beams* **2006**, *24*, 395-401.

- Chuvatin, A.S.; Rudakov, L.I.; Velikovich, A.L.; Modeling of Radiative Properties of the Wire Array Z-Pinches. *AIP Conf. Proc.* **2006**, *808*, 343.
- Chuvatin, A.S.; Kantsyrev, V.L.; Rudakov, L.I.; Cuneo, M.E.; Astanovitskiy, A.L.; Presura, R.; Safronova, A.S.; Esaulov, A.A.; Cline, W.; Williamson, K.M.; Shrestha, I.; Yilmaz, M.F.; Osborne, G.C.; Weller, M.E.; Jarrett, T.; LeGalloudec, B.; Nalajala, V.; Pointon, T.D.; Mikkelson, K.A.; Design and Testing of a Load Current Multiplier on Zebra Facility. *Dense Z-Pinches: 7th International Conference*, **2009**, 1088, 253.
- Clementson, J.; Beiersdorfer, P.; Brown, G.V.; Gu, M.F.; Spectroscopy of M-shell x-ray transitions in Zn-like through Co-like W. *Phys. Scr.* **2010**, *81*, 015301.
- Clementson, J.; Beiersdorfer, P.; Gu, M.F.; X-ray Spectroscopy of E2 and M3 Transitions in Ni-like W. *Phys. Rev. A* **2010**, *81*, 012505.
- Cuneo, M.E.; Vesey, R.A.; Porter, J.L. Jr.; Bennett, G.R.; Hanson, D.L.; Ruggles, L.E.; Simpson, W.W.; Idzorek, G.C.; Stygar, W.A.; Hammer, J.H.; Seamen, J.J.; Torres, J.A.; McGurn, J.S.; Green, R.M.; *Phys. Rev. Lett.* **2002**, *88*, 215004.
- Cuneo, M. E.; Vesey, R. A.; Sinars, D. B.; Chittenden, J. P.; Waisman, E. M.; Lemke, R.W.; Lebedev, S. V.; Bliss, D. E.; Stygar, W. A.; Porter, J. L.; Schroen, D. G.; Mazarakis, M. G.; Chandler, G. A.; Mehlhorn, T. A. Demonstration of Radiation Pulse Shaping with Nested-Tungsten-Wire-Array Z Pinches for High-Yield Inertial Confinement Fusion. *Phys. Rev. Lett.* **2005**, *95*, 185001.
- Cuneo, M.E.; Waisman, E.M.; Lebedev, S.V.; Chittenden, J.P.; Stygar, W.A.; Chandler, G.A.; Vesey, R.A.; Yu, E.P.; Nash, T.J.; Bliss, D.E.; Sarkisov, G.S.; Wagoner, T.C.; Bennett, G.R.; Sinars, D.B.; Porter, J.L.; Simpson, W.W.; Ruggles, L.E.; Wenger, D.F.; Garasi, C.J.; Oliver, B.V.; Aragon, R.A.; Fowler, W.E.; Hettrick, M.C.; Idzorek, G.C.; Johnson, D.; Keller, K.; Lazier, S.E.; McGurn, J.S.; Mehlhorn, T.A.; Moore, T.; Nielsen, D.S.; Pyle, J.; Speas, S.; Struve, K.W.; Torres, J.A.; Characteristics and scaling of tungsten-wire-array z -pinch implosion dynamics at 20 MA. *Phys. Rev. E* **2005**, *71*, 046406.

- Cuneo, M. E.; Sinars, D. B.; Waisman, E. M.; Bliss, D. E.; Stygar, W. A.; Vesey, R. A.; Lemke, R. W.; Smith, I. C.; Rambo, P. K.; Porter, J. L.; Chandler, G. A.; Nash, T. J.; Mazarakis, M. G.; Adams, R. G.; Yu, E. P.; Struve, K. W.; Mehlhorn, T. A.; Lebedev, S. V.; Chittenden, J. P.; Jennings, C. A. Compact single and nested tungsten-wire-array dynamics at 14–19 MA and applications to inertial confinement fusion. *Phys. of Plasmas* **2006**, *13*, 056318.
- Deeney, C.; Douglas, M. R.; Spielman, R. B.; Nash, T. J.; Peterson, D. L.; L'Eplattenier, P.; Chandler, G. A.; Seamen, J. F.; Struve, K. W. Enhancement of X-Ray Power from a Z Pinch Using Nested-Wire Arrays. *Phys. Rev. Lett.* **1998**, *81*, 22.
- Elliott, S.R.; Beiersdorfer, P.; MacGowan, B.J.; Nilsen, J.; Measurements of line overlap for resonant spoiling of x-ray lasing transitions in nickel-like tungsten. *Phys. Rev. A* **1995**, *52*, 2689.
- Esaulov, A.A.; Models of radiation yield from wire array implosion at 1 MA Zebra generator. *Phys. Plasmas* **2006**, *13*, 042506.
- Esaulov, A.A.; Bauer, B.S.; Makhin, V.; Siemon, R.E.; Lindemuth, I.R.; Awe, T.J.; Reinovsky, R.E.; Struve, K.W.; Desjarlais, M.P.; Mehlhorn, T.A.; Radiation magneto-hydrodynamic simulation of plasma formed on a surface by a megagauss field. *Phys. Rev. E* **2008**, *77*, 036404.
- Esaulov, A.A.; Kantsyrev, V.L.; Safronova, A.S.; Velikovich, A. L.; Cuneo, M. E.; Jones, B.; Struve, K. W.; Mehlhorn, T. A.; Magnetostatic and magnetohydrodynamic modeling of planar wire arrays. *Phys. Plasmas* **2008**, *15*, 052703.
- Esaulov, A.A.; Kantsyrev, V.L.; Safronova, A.S.; Williamson, K.M.; Shrestha, I.; Osborne, G.C.; Yilmaz, M.F.; Ouart, N.D.; Weller, M.E.; WADM and radiation MHD simulations of compact multi-planar and cylindrical wire arrays at 1 MA currents. *High Energy Density Physics* **2009**, *5*, 166.
- Fournier, K.B.; Atomic Data and Spectral Line Intensities for Highly Ionized Tungsten

(Co-like W^{47+} to Rb-like W^{37+}) in a High-Temperature, Low-Density Plasma. *Atomic Data and Nuclear Data Tables* **1998**, *68*, 1-48.

- Greenly, J. B.; Douglas, J. D.; Hammer, D. A.; Kusse, B. R.; Glidden, S. C.; Sanders, H. D. A, 1 MA, variable risetime pulse generator for high energy density plasma research. *Rev. Sci. Instrum.* **2008**, *79*, 073501.
- Hansen, S.B., *Ph.D. Dissertation*, University of Nevada, Reno, **2003**.
- Ivanov, V.V.; Hakel, P.; Mancini, R.C.; Chittenden, J.P.; Anderson, A.; Shevelko, A.P.; Wiewior, P.; Durmaz, T.; Altemara, S.D.; Papp, D.; Astanovitskiy, A.L.; Nalajala, V.; Chalyy, O.; Dmitriev, O.; X-ray absorption spectroscopy for wire-array Z-pinches at the non-radiative stage. *High Energy Density Physics* **2011**, *7*, 383-390.
- Jones, B.; Ampleford, D. J.; Vesey, R. A.; Cuneo, M. E.; Coverdale, C. A.; Waisman, E. M.; Jones, M. C.; Fowler, W. E.; Stygar, W. A.; Serrano, J. D.; Vigil, M. P.; Esaulov, A. A.; Kantsyrev, V. L.; Safronova, A. S.; Williamson, K. M.; Chuvatin, A. S.; Rudakov, L. I. Planar Wire-Array Z-Pinch Implosion Dynamics and X-Ray Scaling at Multiple-MA Drive Currents for a Compact Multisource Hohlraum Configuration, *Phys. Rev. Lett.* **2010**, *104*, 125001.
- Kantsyrev, V.; Fedin, D.; Cline, W.; Nalajala, V.; Pokala, S.; Shrestha, I.; Savage, M.; Proc. SPIE 5918 **2005**, 59180W.
- Kantsyrev, V.L.; Rudakov, L.I.; Safronova, A.S.; Fedin, D.A.; Ivanov, V.V.; Velikovich, A.L.; Esaulov, A.A.; Chuvatin, A.S.; Williamson, K.M.; Ouart, N.D.; Nalajala, V.; Osborne, G.C.; Shrestha, I.; Yilmaz, M.F.; Pokala, S.; Laca, P.J.; Cowan, T.E.; Planar Wire Array as Powerful Radiation Source. *IEEE Transactions on Plasma Science* **2006**, *34*, 2295-2302.
- Kantsyrev, V. L.; Rudakov, L. I.; Safronova, A. S.; Velikovich, A. L.; Ivanov, V. V.; Coverdale, C. A.; Jones, B.; LePell, P. D.; Ampleford, D. J.; Deeney, C.; Chuvatin, A. S.; Williamson, K. M.; Shrestha, I.; Ouart, N.; Yilmaz, M. F.; Osborne, G. C.;

- Haboub, A.; Batie, S.; Astanovitsky, A.; LeGalloudec, B.; Nalajala, V.; McDaniel, W.; Shlyaptseva, V.; Adkins, T.; Meyer, C. Properties of a planar wire arrays Z-pinch source and comparisons with cylindrical arrays. *High Energy Density Physics* **2007**, *3*, 136-142.
- Kantsyrev, V. L.; Rudakov, L. I.; Safronova, A. S.; Esaulov, A. A.; Chuvatin, A. S.; Coverdale, C. A.; Deeney, C.; Williamson, K. M.; Yilmaz, M. F.; Shrestha, I.; Ouart, N. D.; Osborne, G. C. Double planar wire array as a compact plasma radiation source. *Phys. of Plasmas* **2008**, *15*, 030704.
 - Kantsyrev, V. L.; Safronova, A. S.; Esaulov, A. A.; Williamson, K. M.; Shrestha, I.; Yilmaz, M. F.; Osborne, G. C.; Weller, M. E.; Ouart, N. D.; Shlyaptseva, V. V.; Rudakov, L. I.; Chuvatin, A. S.; Velikovich, A. L. A review of new wire arrays with open and closed magnetic configurations at the 1.6 MA Zebra generator for radiative properties and opacity effects. *High Energy Density Physics* **2009**, *5*, 115–123.
 - Kantsyrev, V.L.; Safronova, A.S.; Esaulov, A.A.; Williamson, K.M.; Shrestha, I.; Osborne, G.C.; Weller, M.E.; Yilmaz, M.F.; Ouart, N.D.; Shlyaptseva, V.V.; Velikovich A.L.; Rudakov, L.I.; X-ray pulse shaping in experiments with planar wire arrays at the 1.6 MA Zebra generator. *J. of Phys.: Conference Series* **2010**, *244*, 032030.
 - Kantsyrev, V.L.; Esaulov, A.A.; Safronova, A.S.; Velikovich, A.L.; Rudakov, L.I.; Osborne, G.C.; Shrestha, I.; Weller, M.E.; Williamson, K.M.; Stafford, A.; Shlyaptseva, V.V.; Influence of induced axial magnetic field on plasma dynamics and radiative characteristics of Z pinches. *Phys. Rev. E* **2011**, *84*, 046408.
 - Kramida, A.E.; Shirai, T.; Energy levels and spectral lines of tungsten, W III through W LXXIV. *Atomic Data and Nuclear Data Tables* **2009**, *95*, 305-474.
 - Levine, M.A.; Marrs, R.E.; Henderson, J.R.; Knapp, D.A.; Schneider, M.B.; The Electron Beam Ion Trap: A New Instrument for Atomic Physics Measurements. *Phys. Scr.* **1988**, *T22*, 157.

- Mandelbaum, P.; Klapisch, M.; Bar-Shalom, A.; Schwob, J.L.; Zigler, A.; Classification of Cu-I Like 3p-4s and 3p-4d Transitions in X-ray Spectra from Laser-Produced Plasmas of Atoms from Tm to Re in the Range 4-8 Å. *Phys. Lett. A* **1983**, *99*, 84.
- Mandelbaum, P.; Klapisch, M.; Bar-Shalom, A.; Schwob, J.L.; Zigler, A.; Classification of X-ray Spectra from Laser Produced Plasmas of Atoms from Tm to Pt in the Range 6-9 Å. *Phys. Scripta* **1983**, *27*, 39.
- McBride, R. D.; Shelkovenko, T. A.; Pikuz, S. A.; Hammer, D. A.; Greenly, J. B.; Kusse, B. R.; Douglass, J. D.; Knapp, P. F.; Bell, K. S.; Blesener, I. C.; Chalenski, D. A. Implosion dynamics and radiation characteristics of wire-array Z pinches on the Cornell Beam Research Accelerator. *Phys. of Plasmas* **2009**, *16*, 012706.
- Neill, P.; Harris, C.; Safronova, A.S.; Hamasha, S.; Hansen, S.; Safronova, U.I.; Beiersdorfer, P.; The study of X-ray M-shell spectra of W ions from the Lawrence Livermore National Laboratory Electron Beam Ion Trap. *Can. J. Phys.* **2004**, *82*, 931.
- Neu, R.; Fournier, K.B.; Schlögl, D.; Rice, J.E.; Observations Of X-Ray Spectra From Highly Charged Tungsten Ion In Tokamak Plasmas. *J. Phys. B* **1997**, *30*, 5056.
- Osborne, G.C.; Safronova, A.S.; Kantsyrev, V.L.; Safronova, U.I.; Beiersdorfer, P.; Williamson, K.M.; Weller, M.E.; Shrestha, I.; Spectroscopic analysis and modeling of tungsten EBIT and Z-pinch plasma experiments. *Rev. of Sci. Inst.* **2008**, *79*, 10E308.
- Osborne, G.C.; Safronova, A.S.; Kantsyrev, V.L.; Safronova, U.I.; Beiersdorfer, P.; Williamson, K.M.; Weller, M.E.; Shrestha, I.; Spectroscopic analysis and modeling of tungsten EBIT and Z-pinch plasma experiments. *Can. J. Phys.* **2011**, *89*, 1-10.
- Osborne, G.C.; Kantsyrev, V.L.; Safronova, A.S.; Esaulov, A.A.; Weller, M.E.; Shrestha, I.; Shlyaptseva, V.V.; Quart, N.D.; X-ray absorption spectroscopy of aluminum z-pinch plasma with tungsten backlighter planar wire array source. *Rev. of Sci. Inst.* **2012**, *83*, 10E103.

- Porter, F. S.; Audley, M. D.; Beiersdorfer, P.; Kevin, K.R.; Boyce, R.; Brekosky, R. P.; Brown, G. V.; Gendreau, K. C.; Gygax, J. D.; Kahn, S. M.; Kelley, R. L.; Stahle, C. K.; Szymkowiak, A. E.; Laboratory Astrophysics using a Spare XRS Microcalorimeter. *Proc. SPIE* **2000**, *4140*, 407-418.
- Ralchenko, Y.; Tan, J.N.; Gillaspay, J.D.; Pomeroy, J.M.; Silver, E.; Accurate Modeling of Benchmark X-ray Spectra from Highly Charged Ions of Tungsten. *Phys. Rev. A* **2006**, *74*, 042514.
- Renaudin, P.; Audebert, P.; Bastiani-Ceccotti, S.; Chenais-Popovics, C.; Geindre, J.P.; Tzortzakis, S.; Nagels, V.; Matsushima, I.; Shepherd, R.; Gauthier, J.C.; Gary, S.; Girard, F.; Blancard, C.; Faussurier, G.; Time and space-resolved X-ray absorption spectroscopy of aluminum irradiated by a subpicosecond high-power laser. *31st EPS Conf. on Plasma Phys. London* **2004**, *28G*, O-3.34.
- Safronova, A.S.; Kantsyrev, V.L.; Fedin, D.A.; Osborne, G.C.; Yilmaz, M.F.; Hoppe, T.; Nalajala, V.; Douglass, J.D.; McBride, R.D.; Mitchell, M.D.; Maxson, L.M.; Hammer, D.A.; Spectroscopic and Imaging Study of Combined W and Mo X-pinch at 1 MA Z-pinch Generators. *IEEE Trans. Plasma Sci.* **2006**, *34*, 5.
- Safronova, A. S.; Kantsyrev, V. L.; Esaulov, A. A.; Ouart, N. D.; Yilmaz, M. F.; Williamson, K. M.; Shrestha, I.; Osborne, G.; Greenly, J. B.; Chandler, K. M.; McBride, R. D.; Chalenski, D. A.; Hammer, D. A.; Kusse, B. R. Spectroscopy and implosion dynamics of low wire number nested arrays on the 1 MA COBRA generator. *Phys. of Plasmas* **2008**, *15*, 033302.
- Safronova, A.S.; Kantsyrev, V.L.; Faenov, A.Y.; Safronova, U.I.; Wiewior, P.; Renard-Le Galloudec, N.; Esaulov, A.A.; Weller, M.E.; Stafford, A.; Wilcox, P.; Shrestha, I.; Ouart, N.D.; Shlyaptseva, V.; Osborne, G.C.; Chalyy, O.; Paudel, Y.; Atomic physics of relativistic high contrast laser-produced plasmas in experiments on Leopard laser facility at UNR. *High Energy Density Physics* **2012** *8*, 190-195.
- Ouart, N.D.; Safronova, A.S.; Kantsyrev, V.L.; Esaulov, A.A.; Williamson, K.M.;

- Shrestha, I.; Osborne, G.C. ; Weller, M.E.; Studies of Radiative and Implosion Characteristics From Brass Planar Wire Arrays, *IEEE Trans. on Plas. Sci.* **2010** *38*, 631-637.
- Safronova, U.I.; Excitation energies and transition rates in Be-, Mg-, and Zn-like ions. *Mol. Phys.* **2000**, *98*, 1213-1225.
 - Sherlock, M.; Chittenden, J. P.; Lebedev, S. V.; Haines, M. G. Ion collisions and the Zpinch precursor column. *Phys. of Plasmas* **2004**, *11*, 1609.
 - Spielman, R. B. Diamond photoconducting detectors as high power z-pinch diagnostics. *Rev. Sci. Instrum.* **1995**, *66*, 867.
 - Spielman, R. B.; Ruggles, L. E.; Pepping, R. E.; Breeze, S. P.; McGurn, J. S.; Struve K. W. Fielding and calibration issues for diamond photoconducting detectors. *Rev. Sci. Instrum.* **1997**, *1*, 68.
 - Spielman, R. B.; Deeney, C.; Chandler, G. A.; Douglas, M. R.; Fehl, D. L.; Matzen, M. K.; McDaniel, D. H.; Nash, T. J.; Porter, J. L.; Sanford, T. W. L.; Seamen, J. F.; Stygar, W. A.; Struve, K. W.; Breeze, S. P.; McGurn, J. S.; Torres, J. A.; Zagar, D. M.; Gilliland, T. L.; Jobe, D. O.; McKenney, J. L.; Mock, R. C.; Vargas, M.; Wagoner, T. Tungsten wire-array Z-pinch experiments at 200 TW and 2 MJ. *Phys. of Plasmas* **1998**, *5*, 2105.
 - Stygar, W. A.; Spielman, R. B.; Ives, H.; Moore, W. B. S.; Seamen, J. F.; Sharpe, A. W.; Wagoner, T. C.; Gilliland, T. L.; Broyles, R. S.; Mills, J. A.; Dinwoodie, T. A.; Slopek, J. S.; Struve, K. W.; Reynolds, P. G. Proc. of the Eleventh IEEE Pulsed Power Con. **1997**, *Baltimore, MD*, 1258.
 - Vesey, R. A.; Herrmann, M. C.; Lemke, R. W.; Desjarlais, M. P.; Cuneo, M. E.; Stygar, W. A.; Bennett, G. R.; Campbell, R. B.; Christenson, P. J.; Mehlhorn, T. A.; Porter, J. L.; Slutz, S. A. Target design for high fusion yield with the double Z-pinch-driven hohlraum. *Phys. of Plasmas* **2007**, *14*, 056302.

- Wagoner, T. C; Stygar, W. A; Ives, H. C; Gilliland, T. L; Spielman, R. B; Johnson, M. F; Reynolds, P. G; Moore, J. K; Mourning, R. L; Fehl, D. L; Androlewicz, K. E; Bailey, J. E; Broyles, R. S; Dinwoodie, T. A; Donovan, G. L; Dudley, M. E; Hahn, K. D; Kim, A. A; Lee, J. R; Leeper, R. J; Leifeste, G. T; Melville, J. A; Mills, J. A; Mix, L. P; Moore, W. B; Peyton, B. P; Porter, J. L; Rochau, G. A; Rochau, G. E; Savage, M. E; Seamen, J. F; Serrano, J. D; Sharpe, A. W; Shoup, R. W; Slopek, J. S; Speas, C. S; Struve, K. W; Van De Valde, D. M; Woodring, R. M.; Differential-output B-dot and D-dot monitors for current and voltage measurements on a 20-MA, 3-MV pulsed-power accelerator. *Phys. Rev. ST Accel. Beams*, **2008**, *11*, 100401.
- Wiewior, P.P.; Astanovitskiy, A.; Aubry, G.; Batie, S.; Caron, J.; Chalyy, O.; Cowan, T.; Haefner, C.; Le Galloudec, B.; Le Galloudec, N.; Macaulay, V.; Nalajala, V.; Pettee, G.; Samek, S.; Stepanenko, Y.; Vesco, J.; Status of the Leopard Laser Project in Nevada Terawatt Facility. *J. of Fusion Energy* **2012**, *28*, 218-220.
- Williamson, K. M.; Kantsyrev, V. L.; Esaulov, A. A.; Safronova, A. S.; Rudakov, L.I.; Cox, P.; Shrestha, I.; Osborne, G.C.; Weller, M.E.; Ouart, N.D.; Shlyaptseva, V.V. Implosion dynamics in double planar wire array Z pinches. *Phys. of Plasmas* **2010**, *17*, 112705.
- Williamson, K.M.; *Ph.D. Dissertation*, University of Nevada, Reno, **2011**.
- Yilmaz, M.F.; Safronova, A.S.; Kantsyrev, V.L.; Esaulov, A.A.; Williamson, K.M.; Shrestha, I.K.; Weller, M.E.; Osborne, G.C.; Shlyaptseva, V.V.; Modeling of K-shell Al and Mg radiation from compact single, double planar and cylindrical alloyed Al wire array plasmas produced on the 1 MA Zebra generator at UNR. *High Energy Density Physics* **2012**, *8*, 30-37.
- Zigler, A.; Zmora, H.; Spector, N.; Klapisch, M.; Schwob, J.L.; Bar-Shalom, A.; Identification of the spectra of Hf XLV, Ta XLVI, W XLVII, and Re XLVIII isoelectronic to Ni I in laser- produced plasmas. *J. Opt. Soc. Am.* **1980**, *70*, 129.

Part VI

Appendix

A List of Acronyms and Abbreviations

HED	High Energy Density
SPWA	Single Planar Wire Array
DPWA	Double Planar Wire Array
TPWA	Triple Planar Wire Array
ICF	Inertial Confinement Fusion
ICCD	Intense Charge-Coupled Device
XRS	X-Ray Spectrometer
TIXRS	Time-Integrated X-Ray Spectrometer
TGXRS	Time-Gated X-Ray Spectrometer
TGEUV	Time-Gated Extreme Ultraviolet Spectrometer
TIPH	Time-Integrated Pinhole
TGPH	Time-Gated Pinhole
XRD	X-Ray Diode
PCD	Photo-Conducting Diode
EUV	Extreme Ultraviolet
UNR	University of Nevada, Reno
NTF	Nevada Terawatt Facility
SNL	Sandia National Laboratory
LLNL	Lawrence Livermore National Laboratory
RMBPT	Relativistic Many-Body Perturbation Theory
EBIT	Electron Beam Ion Trap
HULLAC	Hebrew University Lawrence Livermore Atomic Code

B Constants

Rydberg Constant	$R_y = 13.605\ 692\ eV$
Electron Mass	$m_e = 0.510\ 999\ MeV/c^2$
Proton Mass	$m_p = 938.272\ MeV/c^2$
Electron Charge	$e = 1.602\ 177 \times 10^{-19}\ C$
Planck's Constant	$\hbar = 6.582\ 119 \times 10^{-16}\ eV\cdot s$
Bohr Radius	$a_0 = 0.529\ 177\ \text{\AA}$
Speed of Light in Vacuum	$c = 2.997\ 925 \times 10^{10}\ cm/s$

C X-Ray Film Calibration

All digitally scanned x-ray films from experiments on Zebra must undergo a series of corrections to determine relative line intensities as well as wavelength or energy scale before it can be useful for analysis. Because certain spectral features may be more easily discerned at one portion of the image than in an area of particular interest, it can often be useful to do a wavelength calibration for one tracing and then apply it to another, a process that is made possible by ensuring that the tracings are taken at the same horizontal positions on the film. Intensity calculations must be applied to each tracing independently, however, due to the removal of background noise that is often both horizontally and vertically inconsistent.

Many of the corrections that must be made to intensity are wavelength dependent, so the first step in film calibration is to convert the horizontal film position in centimeters to a scale that's appropriate to the data, which in the case of the spectrometers used on Zebra and COBRA, is generally angstroms or nanometers. Due to the curved nature of crystal spectrometers, generally a second-order polynomial is used to provide the most accurate scale. Calibrations are done using prominent and well-known lines, and for cases in which the load materials do not produce highly resolved and easily discernible peaks, tracer wires can be introduced (see section 4.1).

Once a satisfactory wavelength calibration has been applied, the pixel values must be

converted to optical density, which is done using the following equation:

$$OD(p) = A_1 + pA_2 + p^2A_3 + p^3A_4 + p^4A_5, \quad (\text{C.1})$$

where A_i refers to a set of coefficients that are determined by the type of film used and p is the initial pixel value between 0 and 255. The first correction that must be calculated once optical density has been determined for each spectrum is the subtraction of background noise. In most cases, a simple method in which areas that are known not to contain continua of unresolved lines provide the minimum point values from which to generate a curve that can be subtracted out.

The raw optical density value must then be corrected for film transmission and filters, both of which are dependant on the type of film and filters used, respectively. The film that was used for this research was primarily Kodak BioMAX and had transmission values calculated as

$$I(\lambda) = I_{def} \left[y_0 + A_1 e^{\lambda/t_1} \right], \quad (\text{C.2})$$

where λ is wavelength, I_{def} is

$$I_{def} = y_0 + A e^{\left(\frac{OD(\lambda)}{a\lambda^b}\right)}, \quad (\text{C.3})$$

and y_0 , A_1 , t_1 , A , a , and b are constants provided by the film manufacturer. Once all of these corrections have been made, the spectra are then normalized to emphasize relative line intensity.

D Zebra Scope Signal Processing

A large number of oscilloscopes are used on Zebra to record measurements from a wide variety of diagnostics, including B-dots, V-dots, diodes, bolometers, laser probe pulses, and others. Each signal must be treated individually with corrections for RF-attenuators, cable lengths, device delays, and device calibration factors. In addition to the various signal adjustments that must be made, each set of data from every oscilloscope must also be synchronized for cross-scope comparisons. As a point of reference to make synchronization

possible, the signal from a B-dot located on the Zebra load chamber is split and sent to one channel of each oscilloscope.

After basic data processing is complete, the first set of calculations that must be performed is an integration and combination of each pair of B-dot signals. For the majority of the B-dots used in these experiments, only a single scaling coefficient is required for each of the B-dot coils, so the integration is simply

$$I(t) = M \int_0^{t_f} V(t) dt, \quad (\text{D.1})$$

where I is the resulting current, M is the experimentally determined calibration constant, t_f is the current end time, and V is the voltage output from the B-dot read on the oscilloscope. Specialized loads occasionally require the use of small B-dots, however, where the walls of the copper aperture that hold the B-dot coils are too thin to neglect penetration terms from surrounding magnetic flux. Wagoner et al. (Wagoner 2008) theorized that this would generate an effect similar to passing the induced B-dot output voltage through a high-pass RC filter with a negative time constant, thereby amplifying low frequency signals. Their proposed first-order correction has proven accurate for our purposes, and results in the integral

$$I(t) = M e^{(-t_f/\tau)} \int_0^{t_f} V(t) e^{t/\tau} dt, \quad (\text{D.2})$$

where the new factor τ is a flux-penetration time characteristic that must also be experimentally determined, effectively turning the calibration into a two-variable fitting. While direct calibration on Zebra for most B-dots is possible, these calibration factors are generally determined on a smaller 50 KV pulser device, a process that is detailed further in appendix E.

Bolometer measurements must also be interpreted into meaningful data from their raw signal outputs. Each of the two bolometers outputs a current monitor and a data signal, which contains a time-integrated representation of the radiation incident on the Ni detector.

The total calculated energy in joules, then, is simply

$$E = \frac{C_{bolo} \cdot \Delta V}{I_{mon}} (J), \quad (D.3)$$

where ΔV is the change in voltage on the detector, I_{mon} is taken from the current monitor, and C_{bolo} is a constant that is specific to the bolometer, its cross section, and its positioning. C_{bolo} can be calculated as

$$C_{bolo} = \frac{\pi^2 R^2 t^2 \rho w}{l \phi}, \quad (D.4)$$

where R is the distance to the plasma source in cm, ρ is the density of the bolometer element in g/cm³, t is its thickness in cm, w is its width in cm, l is its length in cm, and ϕ is its sensitivity in cm.g/J.

D.1 Power Calculations

Two types of power and total energy output estimates are possible using data from various radiation detectors on Zebra. The first requires knowledge of the detector's sensitivity, which is generally given in terms of amps per watt (A/W) for the current induced within the detector when it interacts with an incident photon. The total instantaneous power yield P (W) at any given time t (s) for a point source located a distance r (m) from a detector with cross sectional surface area σ (m²) can then be calculated simply as

$$P(t) = V(t) \left[\frac{F(\epsilon) A(\epsilon) \sigma}{4\pi r^2} \right]^{-1} (W), \quad (D.5)$$

where $F(\epsilon)$ and $A(\epsilon)$ are filter transmission and device sensitivity, respectively, for an incident photon energy ϵ . The largest source of error, then, comes from the fact that the energy of an impacting photon is generally unknown, so estimations must be made regarding the filter transmission and device sensitivity curves. A total energy yield can be calculated by simply integrating this power output over the entire lifetime of the pinch:

$$E_{total} = \int_{t_1}^{t_2} P(t) dt (J). \quad (D.6)$$

There are cases, however, when the device sensitivity may be unknown or the photons incident on the detector span such a wide energy range that the estimations for $F(\epsilon)$ and $A(\epsilon)$ are too inaccurate for proper analysis (as is often the case with the XRDs on Zebra and their corresponding filters). This second method, then, provides a simple means for estimating total power output by using the bolometer - which is insensitive to specific photon energy - in conjunction with a more time-resolved detector, such as an XRD, by taking advantage of the fact that they are placed side by side in the same viewport on the Zebra target chamber. While the XRDs and their filters *are* sensitive to incident photon energy, they have a cutoff range (implemented via filters) that is similar enough to the bolometers' ($A_{XRD}(\epsilon)F_{XRD}(\epsilon) \approx A_{Bolo}(\epsilon)F_{Bolo}(\epsilon)$) to make direct comparisons of x-ray radiation output. The power for a particular point in time t_0 can be calculated, then, as a function of the bolometer energy over the normalized, integrated XRD signal between times t_1 and t_2 , or

$$P(t) = EV_{t_0} \left(\int_{t_1}^{t_2} V(t) dt \right)^{-1} \quad (J/s), \quad (D.7)$$

where E is the bolometer energy from equation D.3, $V(t)$ is the XRD signal as a function of time, and V_{t_0} is the voltage of the signal at t_0 .

E B-Dot Calibrations on a 50 KV Pulser

To minimize disruption of experiments and for testing of B-dots that might be destroyed in Zebra's extreme high-current environment, a 50 KV pulser was recently installed at the NTF. The current generated by the pulser passes first down through a rod containing a current-viewing resistor (CVR) and then to a plate, illustrated in Fig. E.2. A set of eight return current rods connect that plate to another solid plate below, which is connected to ground. A control B-dot is placed an equal distance on the opposite side of the rod for calibration purposes. The magnetic fields from the return current rods must be accounted for in the calibration calculations in addition to the position of the B-dot on the plate. B-dots are oriented in such a way that the coils are always parallel to the direction of current flow, thus making them perpendicular to the magnetic flux, and the return current rods are

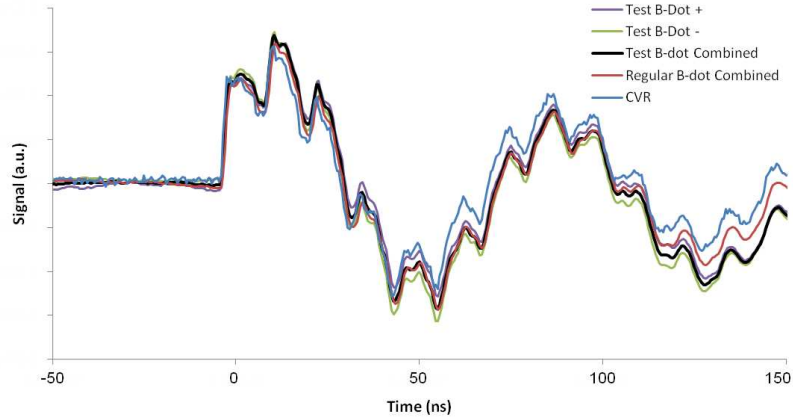


Figure E.1: Sample of calibration shot on the 50 KV pulser at NTF. Lines that indicate they are combined refer to B-dot signals that have had the absolute values of their positive and negative portions averaged together.

estimated to be at an angle of $7\pi/8$. This results in a total correction factor of

$$I_{total} = I \left(\frac{1}{d} - 2\frac{r}{8} \sin \theta \right), \quad (\text{E.1})$$

where d is the distance between the B-dot and the current source rod, r and ϑ are the distance and angle, respectively, between the B-dot and the two nearest return current rods. A sample of the resulting signals can be found in Fig. E.1. It should be noted that the B-dot being calibrated in this example is a standard size, and the small size B-dots must be treated as described in Appendix D.

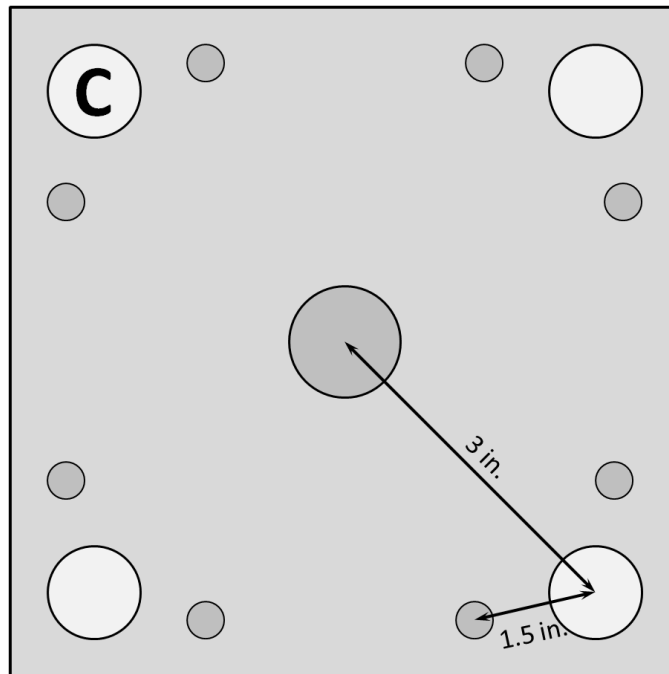


Figure E.2: Cartoon of the plate used on the 50 KV pulser at NTF for calibration of B-dots. Gray circles indicate rods that connect to a bottom plate (which is connected to ground), white circles indicate open holes where B-dots can be installed (the control B-dot position is marked with a C), and the central circle represents the location of the CVR where the current is passed to the plate from the pulser itself.

F List of Publications

Part I

- A.S. Chuvatin, V.L. Kantsyrev, L.I. Rudakov, M.E. Cuneo, A.L. Astanovitskiy, R. Presura, A.S. Safronova, W. Cline, K.M. Williamson, I. Shrestha, G.C. Osborne, B. LeGalloudec, V. Nalajala, T.D. Pointon, K.A. Mikkelson, “Operation of a load current multiplier on a nanosecond mega-ampere pulse forming line generator,” *Physical Review, Special Topics: Accelerators and Beams*, v. 13, pp. 010401 (2010).
- A.S. Chuvatin, V.L. Kantsyrev, L.I. Rudakov, M.E. Cuneo, A.L. Astanovitskiy, R. Presura, A.S. Safronova, A.A. Esaulov, W. Cline, K.M. Williamson, I. Shrestha, M.F. Yilmaz, G.C. Osborne, M. Weller, T. Jarrett, B. LeGalloudec, V. Nalajala, T.D. Pointon, A. Mikkelson, “Design and Testing of a Load Current Multiplier on Zebra Facility,” *AIP Conference Proceedings (Dense Z-pinches)*, v. 1088, pp. 253-258 (2009).
- V.L. Kantsyrev, L.I. Rudakov, A.S. Safronova, D.A. Fedin, V.V. Ivanov, A.L. Velikovich, A.A. Esaulov, A.S. Chuvatin, K. Williamson, N.D. Ouart, V. Nalajala, G. Osborne, I. Shrestha, M.F. Yilmaz, S. Pokala, P.J. Laca, T.E. Cowan, “Planar Wire Array as Powerful Radiation Source,” *IEEE Transactions on Plasma Science*, v.34, No 5, pp. 2295-2302 (2006).
- G.C. Osborne, V.L. Kantsyrev, A.S. Safronova, A.A. Esaulov, M.E. Weller, I. Shrestha, V.V. Shlyaptseva, and N.D. Ouart, “X-ray absorption spectroscopy of aluminum z-pinch plasma with tungsten backlighter planar wire array source,” *Rev. Sci. Inst.* 83, 10E103 (2012).
- A.S. Safronova, A.A. Esaulov, V.L. Kantsyrev, N.D. Ouart, V. Shlyaptseva, M.E. Weller, S.F. Keim, K.M. Williamson, I. Shrestha, G.C. Osborne, “Searching for efficient X-ray radiators for wire array Z-pinch plasmas using mid-atomic-number single planar wire arrays on Zebra at UNR,” *High Energy Density Physics* 7, pp. 252-258 (2011).
- A.S. Safronova, V.L. Kantsyrev, A.A. Esaulov, I. Shrestha, V.V. Shlyaptseva, M.E.

Weller, , N.D. Ouart, G.C. Osborne, K.M. Williamson, S. Keim, A.L. Velikovich, J.L. Giuliani, A.S. Chuvatin, “Producing keV plasmas on Zebra at UNR: achievements, challenges and applications”, AIP Proceedings of 8th International Conference on Dense Z-pinch, August 2011.

Part II

- G.C. Osborne, A.S. Safronova, V.L. Kantsyrev, U.I. Safronova, P. Beiersdorfer, K.M. Williamson, M.E. Weller, and I. Shrestha, P. “Spectroscopic analysis and modeling of tungsten EBIT and Z-pinch plasma experiments,” *Can. J. Physics* 89, 599-608 (2011).
- G.C. Osborne, A.S. Safronova, V.L. Kantsyrev, U.I. Safronova, M.F. Yilmaz, K.M. Williamson, I. Shrestha, P. Beiersdorfer, “Diagnostic of charge balance in high-temperature tungsten plasmas using LLNL EBIT,” *Review of Scientific Instruments*, 79, pp. 10E308 (2008).
- A.S. Safronova, V.L. Kantsyrev, A.Y. Faenov, U.I. Safronova, P. Wiewior, N. Renard-Le Galloudec, A.A. Esaulov, M.E. Weller, A. Stafford, P. Wilcox, I. Shrestha, N.D. Ouart, V. Shlyaptseva, G.C. Osborne, O. Chalyy, Y. Paudel, “Atomic Physics of Relativistic High-Contrast Laser-produced Plasmas in Experiments on Leopard Laser Facility at UNR, ”, submitted to *High Energy Density Physics*, October 2011.
- A.S. Safronova, V.L. Kantsyrev, U.I. Safronova, A.A. Esaulov, M.F. Yilmaz, N.D. Ouart, I. Shrestha, K.M. Williamson, G.C. Osborne, P.G. Wilcox, M.E. Weller, V. Shlyaptseva, C.A. Coverdale, B. Jones, D.J. Ampleford, P.D. LePell, C. Deeney, “Studying radiation from Z-pinch wire array and X-pinch plasmas: K-shell Mg to M-shell Mo,” *AIP Conference Proceedings (Atomic Processes in Plasmas)*, v. 1161, pp. 217-228 (2009).
- A.S. Safronova, V.L. Kantsyrev, A.A. Esaulov, N.D. Ouart, M.F. Yilmaz, K.M. Williamson, I. Shrestha, G.C. Osborne, J.B. Greenly, K.M. Chandler, R.D. McBride, D.A. Chalenski, D.A. Hammer, B.R. Kusse, and P.D. LePell, “Spectroscopy and implosion dynam-

ics of low wire number nested arrays on the 1 MA COBRA generator,” *Physics of Plasmas* 15, 033302 (2008).

- A.S. Safronova, V.L. Kantsyrev, A.A. Esaulov, N.D. Ouart, M.F. Yilmaz, K. M. Williamson, V. Shlyaptseva, I. Shrestha, G.C. Osborne, C.A. Coverdale, B. Jones, C. Deeney, “X-ray diagnostics of imploding plasmas from planar wire arrays composed of Cu and few tracer Al wires on 1 MA pulsed power generator at UNR,” *Review of Scientific Instruments* 79, pp.10E315 (2008).
- A.S. Safronova, V.L. Kantsyrev, P. Neill, U.I. Safronova, D.A. Fedin, N.D. Ouart, M.F. Yilmaz, G. Osborne, I. Shrestha, K. M. Williamson, T. Hoppe, C. Harris, P. Beiersdorfer, S. Hansen, “The importance of EBIT data for Z-pinch plasma diagnostics,” *Can. J. Physics*, v. 86, pp. 267-276 (2008).
- A.S. Safronova, V.L. Kantsyrev, D.A. Fedin, G. Osborne, M.F. Yilmaz, T. Hoppe, V. Nalajala, J.D. Douglass, R.D. McBride, M.D. Mitchell, L.M. Maxson, D.A. Hammer, “Spectroscopic and Imaging Study of Combined W and Mo X-Pinches at 1 MA Z-Pinch Generators,” *IEEE Trans. on Plas. Sci.* 34, 2256 (2006).
- M.F. Yilmaz, A.S. Safronova, V.L. Kantsyrev, A.A. Esaulov, K.M. Williamson, I.K. Shrestha, M.E. Weller, G.C. Osborne, V.V. Shlyaptseva, “Modeling of K-shell Al and Mg radiation from compact single, double planar and cylindrical alloyed Al wire array plasmas produced on the 1 MA Zebra generator at UNR,” *High Energy Density Physics* 8, 30-37 (2012).

Part III

- A.A. Esaulov, V.L. Kantsyrev, A.S. Safronova, K.M. Williamson, I. Shrestha, G.C. Osborne, M.F. Yilmaz, N.D. Ouart, M.E. Weller, “WADM and radiation MHD simulations of compact multi-planar and cylindrical wire arrays at 1 MA currents,” *High Energy Density Physics*, v. 5, pp. 166-172 (2009).
- A.A. Esaulov, V.L. Kantsyrev, A.S. Safronova, K.M. Williamson, I. Shrestha, G.C.

Osborne, “Application of the Wire Ablation Dynamics Model to the Design and Optimization of Wire Array Loads of Complex Geometry,” AIP Conference Proceedings (Dense Z-pinches), v. 1088, pp. 45-48 (2009).

- G.C. Osborne, V.L. Kantsyrev, A.A. Esaulov, A.S. Safronova, M.E. Weller, K.M. Williamson, I. Shrestha, V.V. Shlyaptseva, “Implosion Characteristics of Tungsten and Gold Single Planar Wire Arrays on UNR Zebra Generator”, AIP Proceedings of 8th International Conference on Dense Z-pinches, August 2011.

Part IV

- C.A. Coverdale, A.S. Safronova, V.L. Kantsyrev, N.D. Ouart, A.A. Esaulov, C. Deeney, K.M. Williamson, G.C. Osborne, I. Shrestha, D.J. Ampleford, B. Jones, “Observation of > 400 -eV precursor plasmas from low-wire-number copper arrays at the 1-MA Zebra facility,” Physical Review Letters, v.102, pp. 105006 (2009).
- V.L. Kantsyrev, A.A. Esaulov, A.S. Safronova, A.L. Velikovich, L.I. Rudakov, G.C. Osborne, I. Shrestha, M.E. Weller, K.M. Williamson, A. Stafford, V.V. Shlyaptseva, “Influence of induced axial magnetic field on plasma dynamics and radiative characteristics of Z pinches,” Phys. Rev. E 84, 046408 (2011).
- V.L. Kantsyrev, A.S. Safronova, A.A. Esaulov, K.M. Williamson, I. Shrestha, F. Yilmaz, G.C. Osborne, M.E. Weller, N.D. Ouart, V.V. Shlyaptseva, L.I. Rudakov, A.S. Chuvatin. A.L. Velikovich, “A review of new wire arrays with open and closed magnetic configurations at the 1.6 MA Zebra generator for radiative properties and opacity effects,” High Energy Density Physics, v. 5, pp. 115-123 (2009).
- V.L. Kantsyrev, L.I. Rudakov, A.S. Safronova, A.A. Esaulov, A.S. Chuvatin, C.A. Coverdale, C. Deeney K. M. Williamson, F. Yilmaz, I. Shrestha, N. Ouart, G. Osborne, “Double planar wire array as a compact plasma radiation source,” Physics of Plasmas, v.15, 030704 (2008).
- V.L. Kantsyrev, L.I. Rudakov, A.S. Safronova, A.L. Velikovich, V.V. Ivanov, C.A.

Coverdale, B. Jones, V. Nalajala, P.D. LePell, D.J. Ampleford, C. Deeney, A.S. Chuvatin, K. M. Williamson, I. Shrestha, N. Ouart, F. Yilmaz, G. Osborne, A. Haboub, S. Batie, A. Astanovitsky, B. LeGalloudec, V. Nalajala, W. McDaniel, V. Shlyaptseva, T. Adkins, C. Meyer, "Properties of planar wire arrays Z-pinch source and comparisons with cylindrical arrays," *High Energy Density Physics* 3, 136-142 (2007).

- V.L. Kantsyrev, A.S. Safronova, A.A. Esaulov, A.S. Chuvatin, L.I. Rudakov, A.L. Velikovich, K.M. Williamson, I. Shrestha, G.C. Osborne, M.E. Weller, V.V. Shlyaptseva, N.D. Ouart, A. Stafford, S. Keim, "Yield Enhancement and x-ray pulse shaping of radiation from anisotropic wire array plasma sources," *AIP Proceedings of 8th International Conference on Dense Z-pinchs*, August 2011.
- V.L. Kantsyrev, A.S. Safronova, A.A. Esaulov, K.M. Williamson, I. Shrestha, G.C. Osborne, M.E. Weller, M.F. Yilmaz, N.D. Ouart, V.V. Shlyaptseva, A.L. Velikovich, L.I. Rudakov, "X-ray pulse shaping in experiments with planar wire arrays at the 1.6 MA Zebra generator," *J. of Phys.: Conference Series* 244, 032030 (2010).
- V.L. Kantsyrev, A.S. Safronova, A.A. Esaulov, K.M. Williamson, I. Shrestha, N.D. Ouart, M.F. Yilmaz, P.G. Wilcox, G.C. Osborne, M.E. Weller, V.V. Shlyaptseva, A.S. Chuvatin, L.I. Rudakov, J.B. Greenly, R.D. McBride, P.F. Knapp, I.C. Blessener, K.S. Bell, D.A. Chalenski, D.A. Hammer, B.R. Kusse, "Physics of Multi-Planar and Compact Cylindrical Wire Arrays Implosions on University-Scale Z-Pinch Generators," *AIP Conference Proceedings (Dense Z-pinchs)*, v. 1088, pp. 113-116 (2009).
- M.E. Weller, A.S. Safronova, V.L. Kantsyrev, A.A. Esaulov, N.D. Ouart, K.M. Williamson, I. Shrestha, G. C. Osborne, V.V. Shlyaptseva, "Analysis of Implosion Dynamics and Radiation of Mixed Mo and Al Triple Planar Wire Arrays With Different Inter-row Gap," *AIP Proceedings of 8th International Conference on Dense Z-pinchs*, August 2011.
- K.M. Williamson, V.L. Kantsyrev, A.A. Esaulov, A.S. Safronova, L.I. Rudakov, P. Cox, I. Shrestha, G.C. Osborne, M.E. Weller, N.D. Ouart, V.V. Shlyaptseva, "Pre-

cursor Formation in Double Planar Wire Array Z-Pinches,” *Physics of Plasmas* 17, 112705 (2010).

- K.M. Williamson, V.L. Kantsyrev, A.S. Safronova, A.A. Esaulov, I. Shrestha, N. D. Ouart, M.F. Yilmaz, G.C. Osborne, M.E. Weller, V. Shlyaptseva, A.S. Chuvatin, “Scaling of Radiation Parameters of Planar and Compact Cylindrical Wire Arrays at the 1MA Zebra Generator,” *AIP Conference Proceedings (Dense Z-pinches)*, v. 1088, pp. 141-144 (2009).

Additional Publications

- D.J. Ampleford, S.V. Lebedev, S.N. Bland, S.C. Bott, J.P. Chittenden, C.A Jennings, V.L. Kantsyrev, A.S. Safronova, V.V. Ivanov, D.A. Fedin, P.J. Laca, M.F. Yilmaz, V. Nalajala, I. Shrestha, K. M. Williamson, G. Osborne, A. Haboub, A. Ciardi, “Dynamics of conical wire array Z-pinch implosions,” *Physics of Plasmas* 14, 102704 (2007).
- B. Jones, F. Yilmaz, V. Nalajala, D. Fedin, V.V. Ivanov, V.I. Sotnikov, G. Osborne, V.L. Kantsyrev, A.S. Safronova, K.P. Shelton, P.D. LePell, C.A. Coverdale, D.J. Ampleford, J.L. McKenney, C. Deeney, I. Shrestha, “Measurement of Temperature, Density, and Particle Transport with Localized Dopants in Wire-Array Z Pinches,” *Phys. Rev. Lett.* 100, 105003 (2008).
- V.L. Kantsyrev, D.A. Fedin, A.A. Esaulov, A.S. Safronova, V. Nalajala, K. M. Williamson, G. Osborne, M.F. Yilmaz, N.D. Ouart, J. B. Greenly, J.D. Douglass, R.D. McBride, L.M. Maxson, D.A. Hammer, A.L. Velikovich, “Al and W Wire Array Implosions and energy deposition on the 1-MA COBRA Generator,” *IEEE Transactions on Plasma Science*, v. 34, No 5, pp. 2288-2294 (2006).
- N.D. Ouart, A.S. Safronova, V.L. Kantsyrev, A.A. Esaulov, K.M. Williamson, I. Shrestha, G.C. Osborne, M.E. Weller, “Studies of radiative and implosion characteristics from brass planar wire arrays,” *IEEE Transactions on Plasma Science*, v. 34, No 4, pp. 631-638 (2010).

- N.D. Ouart, M.F. Yilmaz, A.S. Safronova, V.L. Kantsyrev, A.A. Esaulov, K.M. Williamson, G.C. Osborne, I. Shrestha, M.E. Weller, R.D. McBride, P.F. Knapp, K.S. Bell, S.A. Pikuz, T.A. Shelkovenko, J.B. Greenly, D.A. Hammer, B.R. Kusse, "Analysis of Compact Cylindrical Wire Array Implosions with Brass and also by Alternating Brass and Al wires on the 1-MA COBRA Generator," AIP Conference Proceedings (Dense Z-pinch), v. 1088, pp. 65-68 (2009).
- N. Renard - Le Galloudec, J. Cobble, S.L. Nelson, A. Merwin, Y. Paudel, I. Shrestha, G.C. Osborne, K.M. Williamson, V.L. Kantsyrev. "Advantages of a soft protective layer for good signal-to-noise ratio proton radiographs in high debris environment," High Energy Density Physics 7, pp. 247-251 (2011).
- I. Shrestha, V.L. Kantsyrev, A.S. Safronova, A.A. Esaulov, K.M. Williamson, N.D. Ouart, G.C. Osborne, M.E. Weller, M.F. Yilmaz, "Study of electrons beams in wire arrays at 1 MA Z-pinch generator," IEEE Transactions on Plasma Science 34, No 4, pp. 658-666 (2010).
- I. Shrestha, V.L. Kantsyrev, A.S. Safronova, A.A. Esaulov, K.M. Williamson, N.D. Ouart, G.C. Osborne, M.E. Weller, M.F. Yilmaz, "Investigation of characteristics of hard x-rays produced during implosions of wire array loads on 1.6 MA Zebra generator," High Energy Density Physics, v. 6, pp. 113-120 (2010).
- A.S. Safronova, V.L. Kantsyrev, A.A. Esaulov, N.D. Ouart, V. Shlyaptseva, K.M. Williamson, I. Shrestha, G.C. Osborne, M.E. Weller, "Analysis of X-ray Iron and Nickel Radiation and Jets from Planar Wire arrays and X-pinch," J. of Phys.: Conference Series 244, 032031 (2010).
- A.S. Safronova, V.L. Kantsyrev, A.A. Esaulov, N.D. Ouart, M.F. Yilmaz, K.M. Williamson, I. Shrestha, G.C. Osborne, J.B. Greenly, K.M. Chandler, R.D. McBride, D.A. Chalenski, D.A. Hammer, B.R. Kusse, P.D. LePell, "Spectroscopy and implosion dynamics of low wire number nested arrays on the 1 MA COBRA generator," Physics of Plasmas v. 15, 033302 (2008).

- A.S. Safronova, V.L. Kantsyrev, M.F. Yilmaz, G. Osborne, N.D. Ouart, K. Williamson, I. Shrestha, V. Shlyaptseva, S. Batie, B. LeGalloudec, A. Astanovitsky, V. Nalajala, W. McDaniel, “Radiative properties of implosions of combined X-pinch and planar wire arrays composed from different wire materials on the UNR 1 MA Z-pinch generator,” *High Energy Density Physics* 3, 237-241 (2007).
- V.V. Shlyaptseva, V.L. Kantsyrev, A.S. Safronova, A.A. Esaulov, I. Shrestha, K.M. Williamson, G.C. Osborne, M.E. Weller, A. Stafford, S. Keim, “Studying wire array and X-pinch plasmas from Alumel wire loads,” *AIP Proceedings of 8th International Conference on Dense Z-pinchs*, August 2011.
- M.F. Yilmaz, A.S. Safronova, V.L. Kantsyrev, A.A. Esaulov, K.M. Williamson, G.C. Osborne, I. Shrestha, N.D. Ouart, “Spectroscopic features of implosions of Mo single- and double-planar wire arrays produced on the 1 MA Z-pinch generator,” *Journal of Quantitative Spectroscopy and Radiative Transfer*, v.109, pp. 2877- 2890 (2008).